Neural substrates of cold nociception in *Drosophila* larva

Atit A. Patel[1*], Albert Cardona[2,3,4], and Daniel N. Cox[1*]

[1]Neuroscience Institute, Georgia State University, Atlanta, GA, USA

[2]HHMI Janelia Research Campus, Ashburn, VA, USA

[3]MRC Laboratory of Molecular Biology, Cambridge, UK

[4]Department of Physiology, Development, and Neuroscience, University of Cambridge, UK

*** Correspondence:**
Corresponding Authors
apatel221@gsu.edu; dcox18@gsu.edu

Keywords: cold nociception, thermosensation, somatosensory circuits, *Drosophila*.

Abstract

Metazoans detect and differentiate between innocuous (non-painful) and/or noxious (harmful) environmental cues using primary sensory neurons, which serve as the first node in a neural network that computes stimulus specific behaviors to either navigate away from injury-causing conditions or to perform protective behaviors that mitigate extensive injury. The ability of an animal to detect and respond to various sensory stimuli depends upon molecular diversity in the primary sensors and the underlying neural circuitry responsible for the relevant behavioral action selection. Recent studies in *Drosophila* larvae have revealed that somatosensory class III multidendritic (CIII md) neurons function as multimodal sensors regulating distinct behavioral responses to innocuous mechanical and nociceptive thermal stimuli. Recent advances in circuit bases of behavior have identified and functionally validated *Drosophila* larval somatosensory circuitry involved in innocuous (mechanical) and noxious (heat and mechanical) cues. However, central processing of cold nociceptive cues remained unexplored. We implicate multisensory integrators (Basins), premotor (Down-and-Back) and projection (A09e and TePns) neurons as neural substrates required for cold-evoked behavioral and calcium responses. Neural silencing of cell types downstream of CIII md neurons led to significant reductions in cold-evoked behaviors and neural co-activation of CIII md neurons plus additional cell types facilitated larval contraction (CT) responses. Further, we demonstrate that optogenetic activation of CIII md neurons evokes calcium increases in these neurons. Finally, we characterize the premotor to motor neuron network underlying cold-evoked CT and delineate the muscular basis of CT response. Collectively, we demonstrate how *Drosophila* larvae process cold stimuli through

functionally diverse somatosensory circuitry responsible for generating stimulus-specific behaviors.

Introduction

Metazoans detect innocuous and/or noxious environmental cues and appropriately generate relevant behavioral responses. There is a large diversity in types of nervous systems from relatively simple nerve nets to highly complex centralized organs dedicated for processing and executing behavioral commands. The ability of an organism to sense and respond to environmental cues is based on the underlying neural architecture and its connectivity to muscle groups for generating behavioral responses. Understanding the neural substrates underlying the execution of how behavioral commands are generated in the nervous system, spanning from the sensory neuron input to motor neuron output, constitutes one of the key areas of research in contemporary neuroscience.

Drosophila melanogaster is among the premier model organisms for studying molecular, cellular and circuit bases of behaviors in modern neuroscience driven by advances in electron microscopy (EM) connectomics, ability to perform high-throughput behavioral screens, characterization of stereotyped behavioral phenotypes, the ability to perform cell-type specific manipulations and genetic accessibility (for review see (Eschbach & Zlatic, 2020). Another critical benefit of using *Drosophila* to study neural connectivity at the synaptic level is its relatively small, but complex CNS, where there are only ~10,000 neurons in the *Drosophila* larval CNS and ~100,000 neurons in adult *Drosophila melanogaster* brain compared to 86 billion neurons in the human brain (Herculano-Houzel, 2009; Scheffer et al., 2020). Highly detailed serial section transmission electron microscopy (ssTEM) whole brain volumes with synaptic level resolution have been obtained for both *Drosophila* larval (Ohyama et al., 2015) and adult (Zheng et al., 2018) brains, where neurons were reconstructed using a collaborative web-based software, CATMAID (Saalfeld et al., 2009; Schneider-Mizell et al., 2016). Concerted efforts from many laboratories have made tremendous advances in reconstructing the *Drosophila* larval connectome at synaptic level resolution and there has been great progress in mapping out select connectomes at the EM level (Clark et al., 2018; Eschbach & Zlatic, 2020; Kohsaka et al., 2017). Connectomes have been further validated using behavioral and functional imaging studies for olfaction in combination with learning and memory (Berck et al., 2016; Eichler et al., 2017; Eschbach et al., 2020; Saumweber et al., 2018), feeding (Miroschnikow et al., 2018; Schlegel et al., 2016), visual processing (Larderet et al., 2017), locomotion (Carreira-Rosario et al., 2018; Fushiki et al., 2016; Heckscher et al., 2015; Hiramoto et al., 2021; Kohsaka et al., 2019; Zarin et al., 2019; Zwart et al., 2016), chemotaxis (Tastekin et al., 2018), thermosensation (Hernandez-Nunez et al., 2021), mechanosensation (Jovanic et al., 2016; Jovanic et al., 2019; Masson et al., 2020), nociceptive modalities (Burgos et al., 2018; Gerhard et al., 2017; Hu et al., 2017; Imambocus et al., 2022; Kaneko et al., 2017; Ohyama et al., 2015; Takagi et al., 2017), among

others (Andrade et al., 2019; Huckesfeld et al., 2021; Imura et al., 2020; Mark et al., 2021; Valdes-Aleman et al., 2021; Winding et al., 2023).

We are particularly interested in how larval somatosensation functions through peripheral sensory neurons located along the body wall just below the larval cuticle. Larval somatosensory neurons are comprised of type I, mono-ciliated dendrites, (external sensory (es) and chordotonal (Ch) neurons) and type II, bipolar dendritic (td and bd) and highly branched multidendritic (md) neurons (classes I-IV, referred to as CI-IV md). Functional and behavioral roles of these sensory neurons include proprioception (CI md & Ch) (Caldwell et al., 2003; He et al., 2018; Vaadia et al., 2018), heat thermoreception (CIV md) (Babcock et al., 2009; Babcock et al., 2011; Im et al., 2018; Im et al., 2015; Ohyama et al., 2015; Tracey et al., 2003), cold thermoreception (Ch, CII md, & CIII md) (Maksymchuk et al., 2022; Maksymchuk et al., 2023; Turner et al., 2016; Turner et al., 2018), chemoreception (CIV md) (Himmel et al., 2019; Lopez-Bellido et al., 2019) and mechanosensation (Ch, CII md, CIII md, & CIV md) (Hu et al., 2017; Hu et al., 2020; Jovanic et al., 2019; Kaneko et al., 2017; Masson et al., 2020; Ohyama et al., 2015; Scholz et al., 2015; Tsubouchi et al., 2012; Yan et al., 2012; Yoshino et al., 2017). Recent studies have unraveled circuit bases underlying thermo- (heat), chemo- and mechanosensation (Burgos et al., 2018; Hernandez-Nunez et al., 2021; Hu et al., 2017; Hu et al., 2020; Imambocus et al., 2022; Jovanic et al., 2016; Jovanic et al., 2019; Kaneko et al., 2017; Lopez-Bellido et al., 2019; Masson et al., 2020; Ohyama et al., 2015; Yoshino et al., 2017), however, circuit bases of noxious cold thermosensory evoked behaviors are yet to be described.

Neural circuitry downstream of select somatosensory neurons has been elucidated both physiologically and behaviorally in the context of nociceptive stimuli that evoke characteristic rolling behavior in *Drosophila* larvae. Specifically, Ch and CIV md neurons signal through multisensory integrator neurons (Basins) via ascending pathways to command neurons for mechanical and nociceptive stimulation that synergistically impact larval rolling escape responses (Ohyama et al., 2015). CIV md neuron mediated nociceptive escape behaviors also function through premotor neurons such as Down-and-Back (DnB) and medial clusters of CIV md interneurons (mCSI) (Burgos et al., 2018; Yoshino et al., 2017). Additionally, A08n projection neurons receive input from CIV md neuron and the peptidergic neuron DP-ilp7 to integrate multisensory inputs from CII, CIII and CIV md neurons (Imambocus et al., 2022). A08n and DP-ilp7 neurons are specifically required for nociceptive mechanical and chemical sensing but not for nociceptive thermosensation (Hu et al., 2017; Imambocus et al., 2022; Kaneko et al., 2017; Tenedini et al., 2019; Vogelstein et al., 2014). Lastly, Ch and CIII md neuronal connectivity, through ascending projection neurons A09e and TePns as well as premotor neuron Chair-1, are required for anemotaxis and innocuous mechanical sensing (Jovanic et al., 2019; Masson et al., 2020). While CIII md neuron connectivity to select second order neurons has been published (Masson et al., 2020), the functional and behavioral roles of these circuit components in the context of cold nociception remain unexplored. We hypothesized that the noxious cold sensitive somatosensory nociceptive circuit functions through shared circuitry amongst other somatosensory modalities.

114 Analyses of cold sensitive circuitry downstream of CIII md neurons elucidated dual
115 pathways for signal transduction: (1) CIII md neurons directly signal through premotor neurons
116 that modulate motor activity and (2) CIII md neurons also function via multisensory integrators
117 and projections neurons to convey somatosensory information to higher order brain regions.
118 Somatosensory neurons (Ch and CIII md) are required for cold-evoked responses but not CIV
119 md neurons (Turner et al., 2016; Turner et al., 2018). Based on EM connectivity, we performed
120 an unbiased behavioral screen of neuronal types that are synaptically connected to CIII md
121 neurons. Multisensory integration neurons, Basins 1-4, are required for cold nociception,
122 facilitate CIII md-evoked larval contraction (CT) responses, and select Basins exhibit cold-
123 evoked increases in calcium. Premotor neurons, DnB and mCSI, are required and facilitate CIII
124 md neuron mediated responses, whereas Chair-1 premotor neurons are required for cold
125 nociception but do not facilitate CIII md neuron mediated responses. Additionally, nociceptive
126 projection neurons A09e and TePns also integrate cold stimuli but only A09e neurons enhance
127 CIII md neuron mediated behavioral responses. Lastly, cold-evoked muscle activation is
128 strongest in abdominal segments (2-4). Individual muscle groups show distinct stimulus-evoked
129 responses, where dorsal longitudinal/oblique (DL & DO) muscles have sustained activation,
130 lateral transverse (LT) muscles exhibit increasing response during stimulus exposures, and
131 ventral longitudinal/oblique (VL & VO) muscles exhibit declining response. Collectively, we
132 functionally validate cold sensitive circuitry in *Drosophila* larvae from thermosensation, central
133 processing, to identifying muscles responsible for stimulus-evoked behavioral response.
134
135 **Results**
136
137 **Peripheral sensory neurons share synaptic partners**
138 Recent work on competitive interactions and behavioral transitions in *Drosophila* larvae
139 has reported CIII md and Ch connectomes in the context of larval mechanosensation (Masson et
140 al., 2020). We performed a comparative circuit analysis of somatosensory (Ch, CIII md and CIV
141 md) neurons using an online repository hosted by LMB Cambridge, which contains a ssTEM
142 volume of *Drosophila melanogaster* first instar larval central nervous system and a repository of
143 neural reconstructions (https://neurophyla.mrc-lmb.cam.ac.uk/). Here, we report and
144 contextualize relevant CIII md neuron downstream neurons, whose functional roles in cold
145 nociception were evaluated. The meta-analyses of previously published literature on *Drosophila*
146 larval somatosensory connectomes revealed several common post-synaptic partners that are
147 shared amongst Ch, CIII md and CIV md neurons (**Figure 1A**). CIII md neurons are upstream of
148 multisensory integration neurons, pre-motor neurons and projection neurons. Class III md
149 neurons are synaptically connected to multisensory integration neurons (Basin-2, -3 & -4). The
150 downstream pathway from Basins includes connectivity to A00c neurons and a polysynaptic
151 pathway to the rolling command neuron (Goro) via A05q neurons. CIII md neurons are also
152 connected to various pre-motor neurons, which are ventral nerve cord localized neurons
153 providing synaptic input to motor neurons, including DnB, A02n, Chair-1, A01d3, A02f, A02h

154 and A27k, and projection neurons including A05q, A09e, TePn05, A08n, A09o, A02o, and
155 dILP7. The CIII md neuron connectome analyses reveal broad second order connectivity and
156 complex interconnectivity amongst second order neurons (**Figure 1A, Figure 1-figure**
157 **supplement 1**). Functional and behavioral roles of CIII md neuron second order interneurons in
158 cold nociception remain unexplored and below we address this knowledge gap.
159
160
161 **Functional analysis of somatosensory neurons in cold nociception**
162 Due to shared post-synaptic neural connectivity of Ch, CIII md and CIV md neurons
163 (**Figure 1A, Figure 1-figure supplement 1**), we first assessed functional roles of these sensory
164 neurons in cold nociception by investigating: (1) stimulus-evoked calcium responses in the
165 *Drosophila* larval ventral nerve cord; (2) cold-evoked calcium responses of these sensory
166 neurons; (3) necessity and sufficiency of these sensory neurons in cold-evoked behaviors; and
167 (4) examining whether co-activating multiple sensory neurons facilitates CIII-mediated
168 behavioral response in *Drosophila* larvae.
169
170 1. <u>CaMPARI analyses reveal distinct neuropil activation patterns by sensory stimuli</u>
171 *Drosophila* larvae have distinct behavioral responses to various sensory stimuli including
172 touch, heat or cold. Exposure to noxious cold temperatures (≤10°C) evokes highly stereotyped
173 head and tail withdrawal towards the center of the animal, termed here as contraction (CT)
174 response (Patel et al., 2022; Turner et al., 2016). The cold-evoked CT response is defined as at
175 least 10% reduction in larval surface area (**Figure 1-figure supplement 2**). Innocuous
176 mechanical stimuli evoke a suite of behaviors including pausing, turning, head withdrawal,
177 and/or reverse locomotion. Noxious heat exposure leads to a corkscrew body roll escape
178 response (Babcock et al., 2009; Babcock et al., 2011; Im et al., 2015; Ohyama et al., 2015;
179 Tracey et al., 2003). Previous work on stimulus-evoked changes in neural ensembles in larval
180 zebrafish (*Danio rerio*) used the genetically encoded calcium integrator CaMPARI to reveal
181 distinct CNS neural activation patterns in response noxious heat or cold exposure (Fosque et al.,
182 2015). CaMPARI affords great spatial resolution as stimulus-evoked neural responses are
183 captured from a freely moving animal.
184 With CaMPARI and pan-neural imaging of ventral nerve cord neurons, we visualized
185 central representations of somatosensory stimuli across sensory modalities including innocuous
186 mechanical, noxious cold or noxious heat, which are primarily detected via Ch, CIII md, & CIV
187 md neurons, respectively. We pan-neuronally expressed CaMPARI using $R57C10^{GAL4}$ (Jenett et
188 al., 2012; Pfeiffer et al., 2008) and *Drosophila* larvae were simultaneously exposed to diverse
189 sensory stimuli and photoconverting light. Post-hoc imaging of intact *Drosophila* larvae ventral
190 nerve cord revealed relatively little neural activity when larvae are not presented with any
191 sensory stimulus (**Figure 1-figure supplement 3**). However, upon innocuous mechanical (gentle
192 touch) stimulation, there is a marked increase in neural activation as reported by $F_{red/green\ LUT}$
193 (**Figure 1-figure supplement 3**). *Drosophila* larvae exposed to noxious heat experience a large,

194 spatially broad increase in neural activity. Incidentally, similar neuropil regions appear to be
195 activated by both innocuous touch and noxious heat, albeit at different levels (**Figure 1-figure**
196 **supplement 3**). Lastly, noxious cold exposure leads to robust neural activation medially, in the
197 neuropil, however, cell bodies seem to have lower activation levels compared to touch or heat
198 stimulations (**Figure 1-figure supplement 3**). These experiments measuring pan-neuronal
199 ventral nerve cord activity in response to sensory stimuli would be ideal for comparative neural
200 activation analyses, were the spatial resolution of the optical microscope sufficient.
201 Acknowledging the limitations of the approach, we heretofore focus instead on single-cell type
202 specific genetic driver lines for identified neurons that can be assigned to known neurons in the
203 connectome,
204
205 2. <u>CIII md somatosensory neurons exhibit robust Ca^{2+} responses to cold</u>
206 Somatosensory neurons function as primary sensors of external stimuli. Ch and CIII md
207 neurons have previously been reported to exhibit cold-evoked Ca^{2+}increases (Turner et al., 2016;
208 Turner et al., 2018) whereas CIV md neurons are weakly sensitive to cold stimuli (Turner et al.,
209 2016). Furthermore, previous studies have addressed the potential confounds of cold-induced
210 muscle contraction on cold-induced electrical activity of CIII md neurons, where
211 electrophysiological recordings performed on de-muscled larval fillets revealed that CIII md
212 neural activity is not dependent upon muscles in response to cold. Exposure to noxious cold
213 stimuli results in temperature-dependent increases in CIII neuron electrical activity consisting of
214 both bursting and tonic firing (Himmel et al., 2021; Himmel et al., 2022; Himmel et al., 2023;
215 Maksymchuk et al., 2022; Maksymchuk et al., 2023; Patel et al., 2022). Cold sensitivity of
216 sensory neurons (Ch, CIII md, & CIV md) was assessed by selectively expressing the
217 *CaMPARI2* Ca^{2+} integrator in sensory neurons using cell-type specific driver lines (**Figure 1-**
218 **figure supplement 4A**). CaMPARI2 signal, as assessed by F_{red}/F_{green} ratios at the cell body,
219 reveal all three neuron subtypes (Ch, CIII md and CIV md) have significantly higher response
220 upon cold exposure compared to no stimulus controls (**Figure 1B, Figure 1-figure supplement**
221 **4B**). Unsurprisingly, as high-threshold nociceptors, CIII md or CIV md neurons present
222 relatively low responses upon photoconverting light exposure *sans* cold (**Figure 1B, Figure 1-**
223 **figure supplement 4B**). However, mechanosensitive Ch neurons exhibit relatively high
224 responses upon exposure to only photoconverting light but no stimulus indicative of high
225 baseline neuronal activity (**Figure 1B, Figure 1-figure supplement 4B**).
226 Similar to the analysis at cell bodies, in the dendrites of Ch neurons we observe marked
227 increases in CaMPARI2 response to photoconverting light (control), however, upon cold
228 exposure (experimental condition) there is a further increase in CaMPARI2 response (**Figure**
229 **1C**). Sholl intensity analysis (see methods) likewise reveals that CIII md neurons present
230 relatively low CaMPARI2 response in control conditions, however, there is a robust cold-evoked
231 increase in CaMPARI2 response throughout the dendrites (**Figure 1C**). Interestingly, CIV md
232 neurons also exhibited significant increases in CaMPARI2 response upon cold exposure in the
233 cell body (**Figure 1B**). However, there is no change in distal dendritic CIV md neuron

234 CaMPARI2 response between cold and no stimulus conditions (**Figure 1C**). CIII md have robust
235 cold-evoked Ca^{2+} responses compared to Ch and CIV md neurons, which have relatively low
236 cold-evoked Ca^{2+} increases (**Figure 1B, C**). Collectively, these data validate previous findings
237 that identified CIII md neurons as the most sensitive to noxious cold temperatures both at the cell
238 body and dendrites, and thus we focused our study on the neural circuitry postsynaptic to CIII
239 md neurons.
240
241 3. <u>CIII md somatosensory neurons are necessary and sufficient for the cold response</u>
242 We assessed the necessity of somatosensory neurons in noxious cold-evoked behavioral
243 responses (**Figure 1-figure supplement 2**) by expressing tetanus toxin light chain, which
244 inhibits neurotransmitter release (Sweeney et al., 1995). Based on Ca^{2+} imaging, we expected
245 both Ch and CIII md neurons may be necessary for cold-evoked CT responses. Neural silencing
246 of Ch or CIII md neurons led to significant reductions in cold-evoked CT responses compared to
247 either *w1118* (parental line) or $Empty^{GAL4}$ controls (a GAL4 construct lacking the promotor
248 sequence; **Figure 1D**). Instantaneous behavioral response curves also indicate lower cold
249 sensitivity when either Ch or CIII md neurons are silenced. However, inhibiting neurotransmitter
250 release in CIV md neurons alone did not result in significant reductions in cold-evoked CT
251 responses (**Figure 1D**). To further assess the requirement of CIII md neuron activity for cold-
252 evoked behaviors, we simultaneously measured the delay from the onset of CIII md cold-evoked
253 Ca^{2+} increases to evoked mouth hook retraction. Upon neural silencing of CIII md neurons, there
254 is a significant delay in mouth hook retraction compared to controls suggesting that cold-evoked
255 head withdrawal requires sensory perception (**Figure 1-figure supplement 4C**). Among the
256 three somatosensory neuron types tested, neural silencing of CIII md neurons resulted in the
257 strongest impairment in cold-evoked behavioral response.
258 Next, we evaluated whether neural activation of sensory neurons via optogenetics would
259 be sufficient to elicit the CT behavioral response (**Figure 1-figure supplement 5A**). First, we
260 tested the efficacy of various optogenetic actuators in eliciting CIII-evoked CT responses using
261 either blue light actuators (ChR2, ChR2-H134R, and ChETA) or red-shifted actuator
262 (CsChrimson) and two independent CIII md *GAL4* drivers were used ($19\text{-}12^{GAL4}$ and
263 $GMR83B04^{GAL4}$) (**Figure 1-figure supplement 6 A-F**) (Berndt et al., 2011; Boyden et al., 2005;
264 Gunaydin et al., 2010; Klapoetke et al., 2014). Collectively, using either blue or red-shifted
265 optogenetic actuators third instar *Drosophila* larvae exhibited light-evoked CT responses (**Figure**
266 **1-figure supplement 6**). We selected ChETA for the majority of the experiments due to its high
267 spike fidelity and lack of plateau potential (Gunaydin et al., 2010). We expressed ChETA in
268 individual sensory neuron subtypes and assessed evoked behavioral responses (Gunaydin et al.,
269 2010). When assessing evoked responses, we first analyzed CT responses as measured by
270 changes in surface area (**Figure 1-figure supplement 5B**). Only neural activation of CIII md
271 neurons led to CT responses in *Drosophila* larvae (**Figure 1E**) consistent with our previously
272 published work (Turner et al., 2016). Additionally, we analyzed larval mobility, which refers to
273 changes in larval postures as measured by changes in occupied space (**Figure 1-figure**

supplement 5C). Upon neural activation of CIII md neurons, there is a large increase in *Drosophila* larval immobility compared to controls (**Figure 1-figure supplement 7A-C**). However, there was no difference in immobility when either Ch or CIV md neurons were optogenetically activated compared to control (**Figure 1-figure supplement 7A-C**). Of the somatosensory neurons tested, only CIII md neurons are sufficient to elicit the CT response.

4. Effect of co-activating CIII md somatosensory neurons plus additional somatosensory neuron classes

Both Ch and CIV md neurons share common first order post-synaptic partners with CIII md neurons and all three somatosensory present cold-evoked increases in calcium levels. However, neither Ch nor CIV md are sufficient to elicit a CT response. To further clarify the roles of Ch and CIV md in cold-evoked behaviors, we simultaneously activated CIII md neurons plus either Ch or CIV md neurons. We expected that co-activation of multiple sensory neuron subtypes would facilitate optogenetically-evoked CT responses. Optogenetic activation of CIII md neurons using two CIII driver lines (*19-12*^{GAL4} and *83B04*^{GAL4}) led to sustained increases in instantaneous CT responses compared to control, where only one driver line (*19-12*^{GAL4}) was used to activate CIII md neurons (**Figure 1F**). The activation of CIII md neurons concurrently using two driver lines (expressed in the same cell type, CIII md) led to a significant increase in immobility compared to single *GAL4* driver-mediated activation of these neurons (**Figure 1-figure supplement 7D-F**), suggesting a single GAL4 line does not exhaust the dynamic range of the CT response. Co-activation of CIII md and Ch neurons, which are cold sensitive and required for cold-evoked CT responses, led to a subtle initial increase in instantaneous CT response compared to CIII activation alone, however, the initial increase in evoked CT response was quickly reduced to well below control (**Figure 1F**). Therefore, the co-activation of two somatosensory neuron types, Ch and CIII md, elicited a CT response that varied along the temporal axis relative to the activation of CIII md alone. *Drosophila* larval immobility was reduced during co-activation of Ch and CIII md neurons compared to CIII md neuron activation alone suggesting that Ch neurons do not facilitate CIII md neuron mediated CT responses (**Figure 1-figure supplement 7D-F**). CIV md and CIII md neurons share a large proportion of common second order interneuron connectivity including multisensory integration neurons, premotor and ascending neurons. We predicted that CIV md and CIII md neuron co-activation might potentiate CT responses. Interestingly, simultaneous activation of CIII and CIV md neurons led to small but insignificant reductions in instantaneous and peak CT responses compared to CIII md neuron activation alone (**Figure 1F**). Similarly, co-activation of CIII md and CIV md neurons did not alter larval immobility compared to only CIII md neuron activation (**Figure 1-figure supplement 7D-F**). Ch neurons are cold sensitive and required for cold nociceptive behaviors but do not facilitate CIII md neuron-evoked behavioral responses (Figure 1B-F) (Turner et al., 2018). Meanwhile, CIV md neurons are modestly cold sensitive but are not required for cold nociception and do not facilitate CIII md neuron-evoked CT responses.

Collectively, CIII md neurons have the strongest cold-evoked calcium response, are required for cold-evoked behavioral response and are sufficient for the CT response.

5. CT response in *Drosophila* larvae throughout development

Synaptic connectivity was mapped using first instar larvae, however, thus far we assessed cold- or CIII md-evoked larval behavioral responses in third instar larvae. Previous work assessing how synaptic connectivity scales between first and third instar larvae revealed that there is a five-fold increase in the number of synaptic connections and the size of neurons thus conserving overall connectivity as measured by percent of input synapses during larval development (Gerhard et al., 2017). Similarly, larval muscle cell size and sarcomere number scale linearly with the larval body size, while maintaining average sarcomere length (Balakrishnan et al., 2020; Demontis & Perrimon, 2009). Muscle contractile force analyses showed that total larval contractile force generation is not dependent on the size or the orientation of third instar larvae (Ormerod et al., 2022). We investigated how CT behavior changes throughout larval development by assessing both cold- and CIII md-evoked responses. First, cold-evoked larval CT magnitude and duration scale linearly across development (**Figure 1G, H**). *Drosophila* larvae with silenced CIII md neurons exhibited significantly reduced CT duration and magnitude compared to age matched controls (**Figure 1G, H**). Next, we evaluated how CIII md neuron-evoked CT behavior develops in *Drosophila* larvae. Similar to cold-evoked CT responses, CIII md neuron-evoked CT behavior also shows a linear trend in CT duration and magnitude (**Figure 1G, H**). Lastly, we assessed the similarity between cold- and CIII md-evoked CT responses throughout larval development. For second instar larvae, there was a 20% change increase in CT duration from first instar larvae for both cold and CIII md activation (**Figure 1H**). For third instar larvae, there was a greater increase in CT duration from first instar larvae for cold-evoked compared to CIII-activation (**Figure 1H**). Meanwhile, developmental increases in CT magnitude between cold- and CIII md neuron activation are nearly identical (**Figure 1H**). Collectively, cold-evoked CT response scales linearly throughout development, where CIII md neurons are necessary and sufficient for cold nociceptive responses.

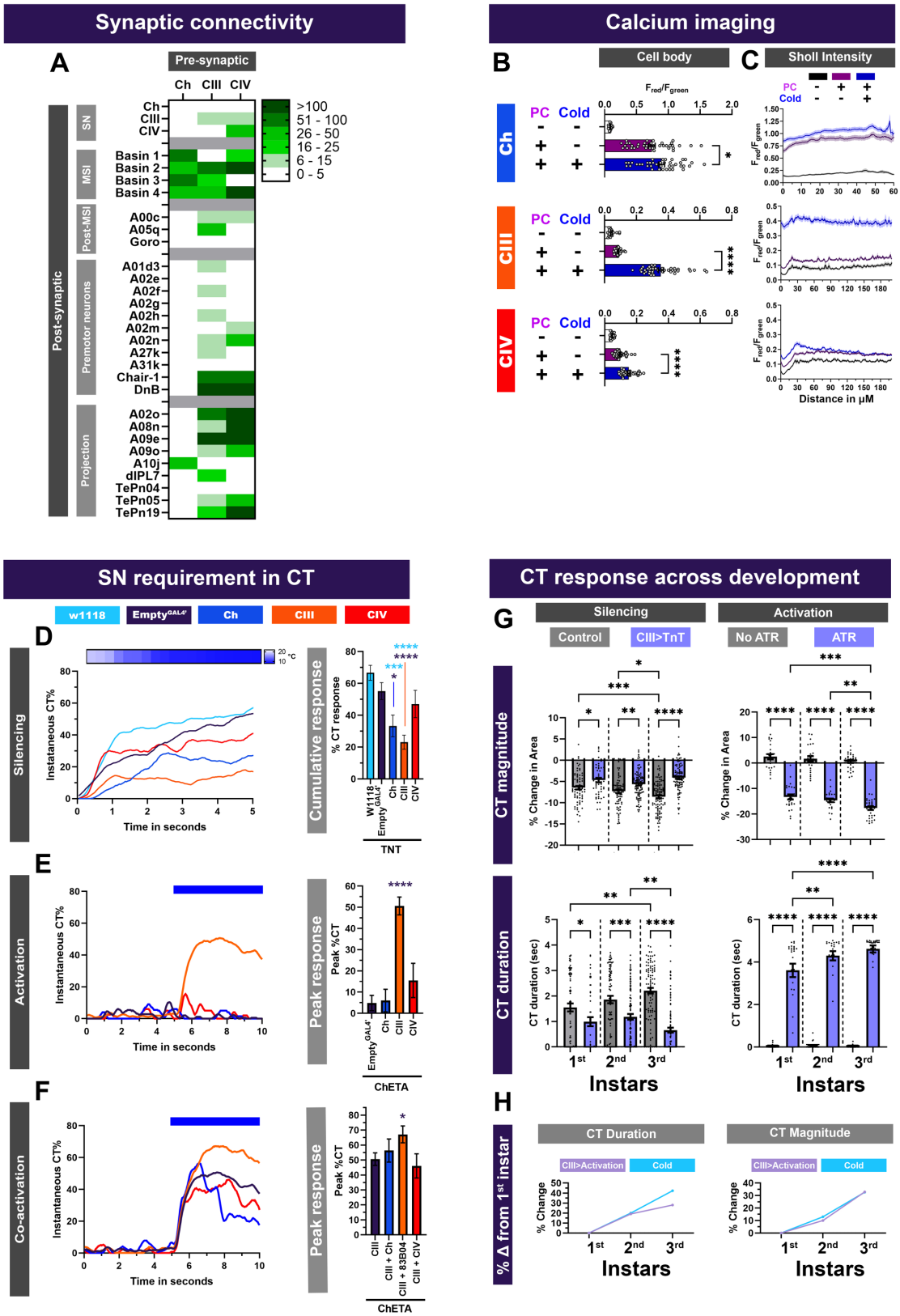
Synaptic connectivity
A
Pre-synaptic
Ch CIII CIV
Post-synaptic
SN
MSI
Post-MSI
Premotor neurons
Projection
Ch
CIII
CIV
Basin 1
Basin 2
Basin 3
Basin 4
A00c
A05q
Goro
A01d3
A02e
A02f
A02g
A02h
A02m
A02n
A27k
A31k
Chair-1
DnB
A02o
A08n
A09e
A09o
A10j
dIPL7
TePn04
TePn05
TePn19
>100
51 - 100
26 - 50
16 - 25
6 - 15
0 - 5
Calcium imaging
B
Cell body
C
Sholl Intensity
PC
Cold
Ch
CIII
CIV
Distance in µM
SN requirement in CT
w1118
Empty
Ch
CIII
CIV
D
Silencing
Instantaneous CT%
Time in seconds
Cumulative response
% CT response
TNT
E
Activation
Peak response
Peak %CT
ChETA
F
Co-activation
CIII + Ch
CIII + 83B04
CIII + CIV
CT response across development
G
Silencing
Activation
Control
CIII>TnT
No ATR
ATR
CT magnitude
% Change in Area
CT duration
CT duration (sec)
1st
2nd
3rd
Instars
H
% Δ from 1st instar
CT Duration
CT Magnitude
CIII>Activation
Cold
% Change

346 **Figure 1: CIII md neurons are primary cold sensors and share common post-synaptic**
347 **partners with mechanosensory and nociceptive Ch and CIV md neurons.**
348 **(A)** Sensory neuron second order connectome analyses. Heatmap plot of synaptic connections
349 between sensory neuron subtypes including chordotonal (Ch), class III (CIII) md, class IV (CIV)
350 md neurons and previously published centrally located neurons. Sensory neurons (SN) Ch, CIII
351 md, and CIV md were analyzed. Multisensory integrator (MSI) neurons include Basin-1, -2, -3,
352 and -4. Neurons downstream of MSI (Post-MSI) include A00c, A05q and Goro. Premotor
353 neurons (PMNs) include Chair-1 (A10a), Down and Back (DnB), A02m and A02n. Lastly,
354 sensory neurons are also connected to several command/projection neurons including A02o,
355 A09e, A10j, A09o, TePn04 and TePn05. Synaptic connectivity data was extracted from
356 Neurophyla LMB Cambridge. (https://neurophyla.mrc-lmb.cam.ac.uk/). (**B-C**) Calcium imaging
357 of sensory neurons including chordotonal (IAV^{GAL4}), class III md ($19\text{-}12^{GAL4}$) and class IV md
358 (ppk^{GAL4}) neurons using CaMPARI2. There were three conditions for sensory neurons: No
359 photoconversion (PC) control (no stimulus and no photoconversion), photoconversion control
360 (photoconversion and no stimulus) and stimulus (Stim) condition (photoconversion and 6°C
361 stimulus). CaMPARI2 data are reported area normalized intensity ratios for F_{red}/F_{green} (mean ±
362 SEM). Average N for each cell type and each condition is n=32. (**B**) CaMPARI2 response
363 measured at the cell body for each neuron type. (**C**) Sholl intensity analysis performed using
364 custom FIJI scripts. CaMPARI2 response is measured radially away from the center of the soma.
365 (**D**) Cold-evoked responses of third instar *Drosophila* larva. Sensory neurons Ch, CIII md or CIV
366 md neurons were silenced by inhibiting neurotransmitter release via cell type specific expression
367 of tetanus toxin (TNT). (**D, left**) Instantaneous %CT over time. The heatmap on top represents
368 change in temperature over time. (**D, right**) Cumulative %CT response for a duration of 5
369 seconds. Controls include *w1118* and $Empty^{GAL4}>TNT$. Significant stars: turquoise stars represent
370 comparison to *w1118* and purple stars represent comparison to $Empty^{GAL4}>TNT$. Average n=72.
371 (**E**) Neural activation of sensory neurons via cell type specific expression of ChETA relative to
372 $Empty^{GAL4}>ChETA$ control. $Empty^{GAL4}$ n=35. Ch n=20, CIV n=20. & CIII n=143. (**E, left**)
373 Instantaneous %CT over time. Blue bar represents optogenetic neural activation. (**E, right**) Peak
374 %CT. (**F**) Neural co-activation of sensory neurons and CIII md neurons. Here each condition
375 represents expression of *ChETA* in CIII md neurons and plus Ch (via *IAV-GAL4*), CIII (via
376 $R83B04^{GAL4}$) or CIV md neurons (via ppk^{GAL4}). (**F, left**) Instantaneous %CT over time. Blue bar
377 represents optogenetic neural activation. (**F, right**) Peak %CT response during optogenetic
378 stimulation. CIII n=143 and average experimental n=50 Significant differences indicated via
379 asterisks, where *p<0.05, ***p<0.001, and ****p<0.0001. (**G, left**) Cold-evoked CT behavioral
380 responses throughout larval development. In controls (w^{1118}), cold-evoked CT responses are
381 stronger as the larvae develop. CT magnitude is significantly greater between 1st v. 3rd instars
382 and 2nd v. 3rd instars. CT duration is significantly higher between 1st v. 3rd instars. Silencing CIII
383 md ($19\text{-}12^{GAL4}$) using TNT leads to significantly reduced cold-evoked responses as measured via
384 CT duration and magnitude across development when compared to age matched w^{1118} controls.
385 For each condition average n = 82 larvae. (**G, right**) CIII md neuron activation via optogenetics

reveals that CT responses increase as the animal develops. No ATR controls do not exhibit any CT responses as measured by CT duration and magnitude. Activating CIII md (*19-12^{GAL4}*) using ChR2-H134R leads to significantly increased optogenetic-evoked responses as measured via CT duration and magnitude across development when compared to age matched no ATR controls. *Drosophila* larvae with ATR show significant increase in CT magnitude between 1st v. 3rd instars and 2nd v. 3rd instars. Additionally, CT duration is significantly higher between 1st v. 2nd instars and 1st v. 3rd instars. For each condition average n = 27 larvae (**H**) Comparison between cold- and CIII-evoked CT responses throughout development, where the CT duration and magnitude are normalized to 1st instar larvae. (**H, left**) For 2nd instar larvae both cold- and CIII-evoked CT duration increases by ~20% compared to 1st instar larvae. For 3rd instar larvae both cold- and CIII-evoked CT duration increases by ~40% and ~30%, respectively, compared to 1st instar larvae. (**H, right**) For 2nd instar larvae both cold- and CIII-evoked CT magnitude increases by ~13% and ~10%, respectively, compared to 1st instar larvae. For 3rd instar larvae both cold- and CIII-evoked CT magnitude increases by ~32% compared to 1st instar larvae.

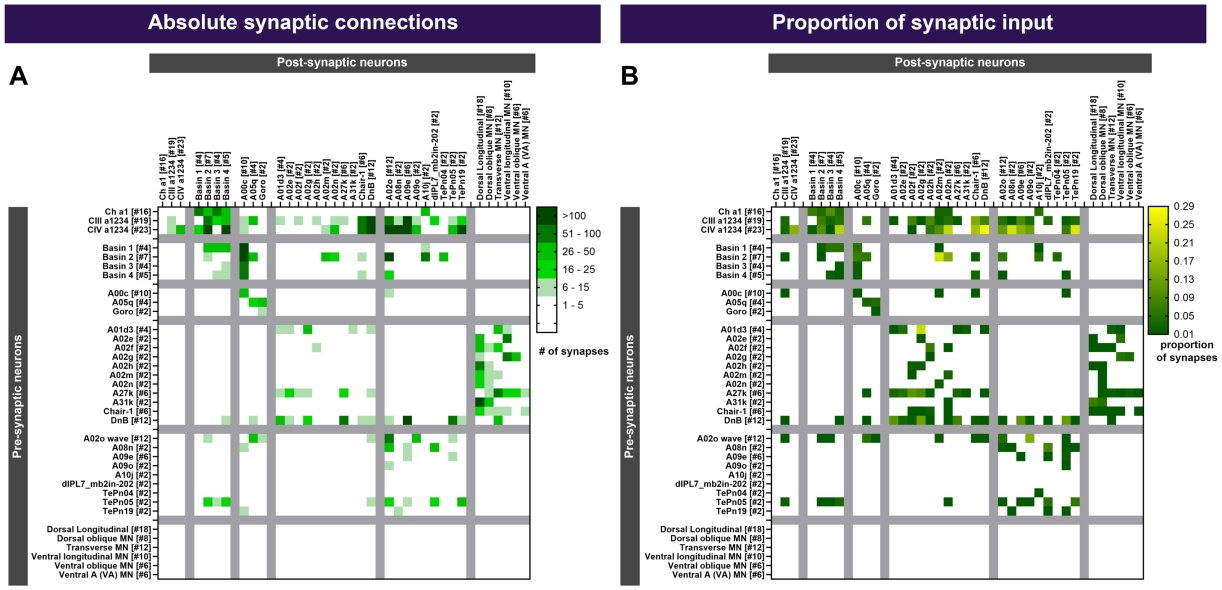

Figure 1-figure supplement 1: Sensory neuron connectivity matrix.
Synaptic connectivity matrix for neurons whose role in cold nociception was assessed. The number in brackets indicates the total number of neurons analyzed for each cell-type. (**A**) Absolute number of synaptic connections between pre- and post-synaptic neurons. (**B**) Connectivity represented as proportion of synaptic input to the post-synaptic neurons.

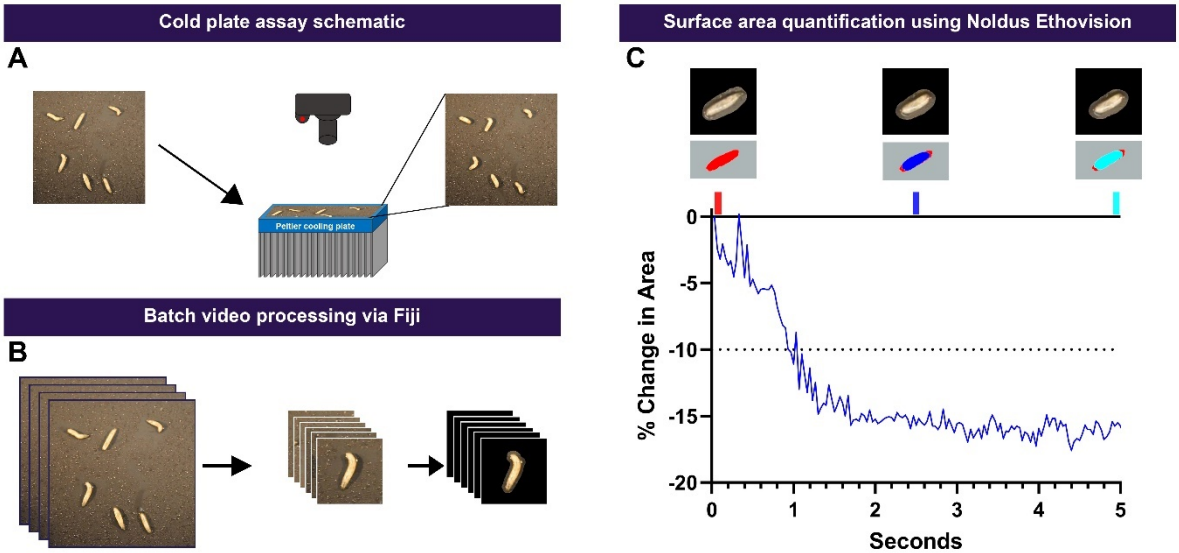

Figure 1-figure supplement 2: *Drosophila* larval cold plate assay and quantitative analysis. (**A**) A schematic of cold plate assay. Briefly, 3rd instar *Drosophila* larvae are plated on a thin metal plate, then we expose the larvae to noxious temperature by transferring the plate onto pre-chilled Peltier cold plate. (**B**) Behavior videos are automatically processed using custom macros in Fiji, where behavioral videos are cropped, and background is removed to improve quantitative analysis. (**C**) Larval surface is area is measured using Noldus Ethovision. The following larval cold-evoked contraction (CT) behavioral metrics are calculated using r: Instantaneous CT%, cumulative CT%, CT duration and CT magnitude. We define CT behavioral response as a reduction in surface area less than -10%.

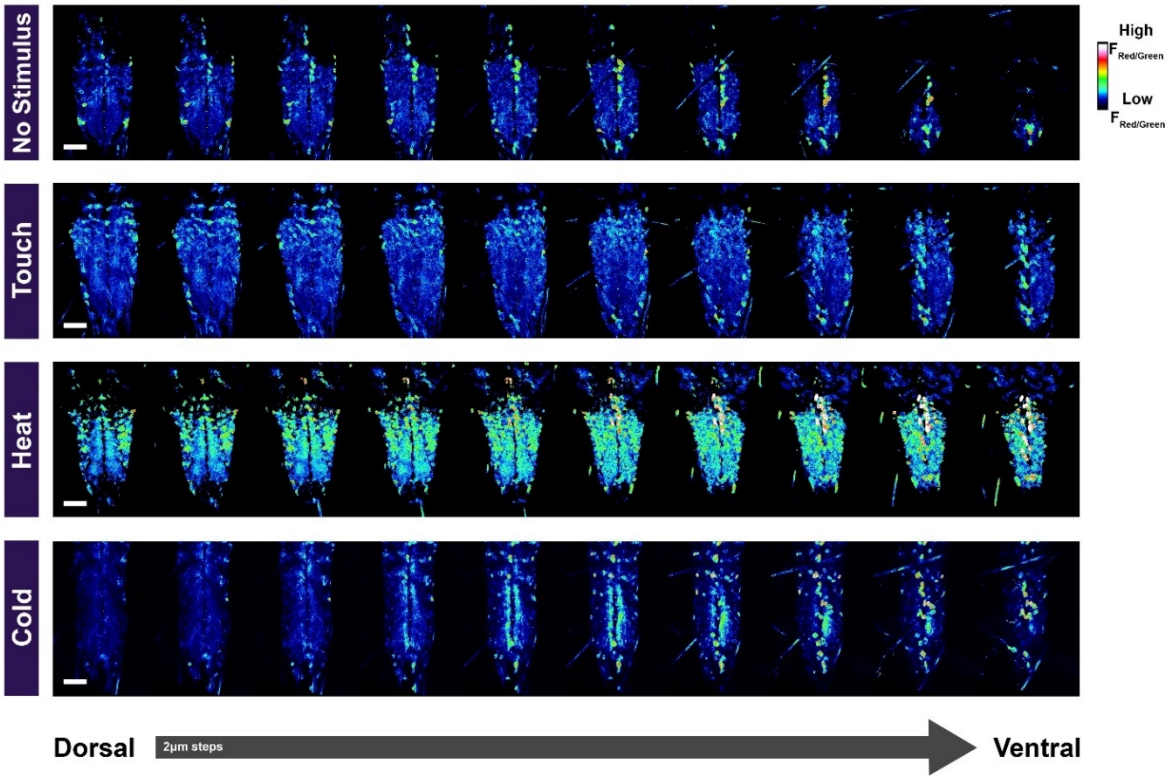

421
422 **Figure 1-figure supplement 3: Stimulus-evoked calcium responses of *Drosophila* larval**
423 **ventral nerve cord.**
424 Representative images of *Drosophila* larval *in vivo* intact animal ventral nerve cord calcium
425 responses assessed via pan-neural CaMPARI expression. Freely moving larvae were exposed to
426 innocuous touch, noxious heat (45°C) or noxious cold (6°C) stimulus for 20 seconds and
427 simultaneously exposed to 20 seconds of photo-converting light. Z-stacks of ventral nerve cord
428 are shown with 2µm steps. Briefly, all animals were from the same batch, imaging was
429 conducted using the same settings, and larvae were exposed to the same levels of photo-
430 converting light. For better visualization, F_{red}/F_{green} CaMPARI fluorescence is reported, and
431 images were pseudo-colored for enhancing signal-to-noise ratio, where highest intensity
432 represented as white and lowest intensity with dark blue. Scale bar represents 50µm.
433

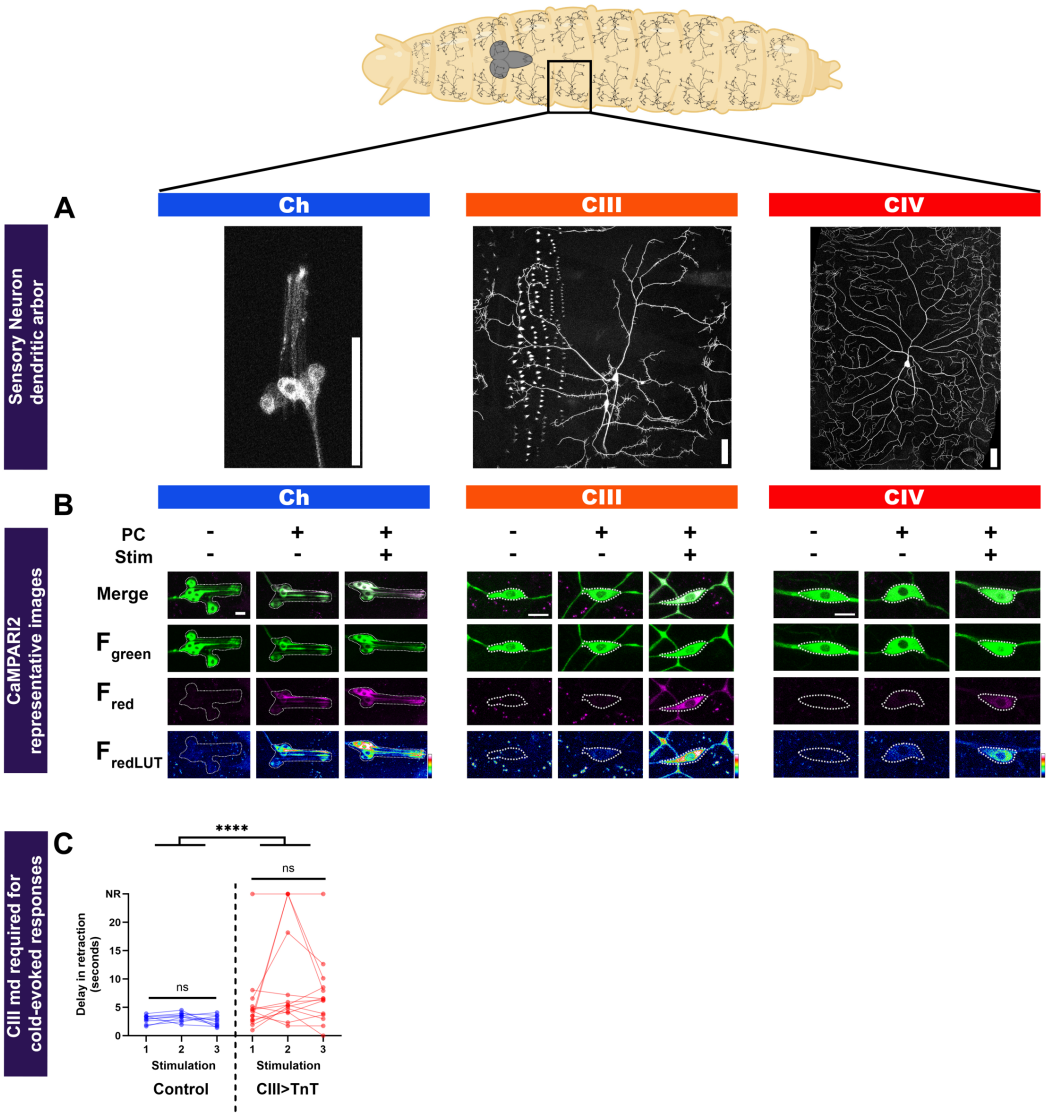

Figure 1-figure supplement 4: Somatosensory neural dendritic morphology and representative images of sensory neurons expressing CaMPARI2.
(**A**) Representative images of somatosensory neurons (Ch, CIII md and CIV md). Note, all images have separate magnification. Each image's scale bar represents 50µm. Drosophila larva and larval brain graphic was created with BioRender.com. (**B**) Confocal images of chordotonal (Ch: *IAV*^{GAL4}), class III md (CIII: *19-12*^{GAL4}) and class IV md (CIV: *ppk*^{GAL4}) neurons expressing CaMPARI2. There were three conditions for sensory neurons: No photoconversion control (no stimulus (Stim) and no photoconversion (PC)), photoconversion control (photoconversion and no stimulus) and stimulus condition (photoconversion and 6°C stimulus). Top row shows merge of F_{red} and F_{green}, second row is F_{green}, third row is F_{red} and last row contains F_{redLUT}, which is pseudo-colored with highest intensity being white and lowest intensity being dark blue (color

447 scale bar on bottom right). Cell body and dendrites are outlined in white for Ch and cell body are
448 outlined in white for CIII and CIV neurons. Scale bar represents 10µm. (**C**) CIII md
449 neurotransmitter release is required for cold-evoked mouth hook retraction in *Drosophila* larvae.
450 Using epifluorescence microscopy, CIII md neuron cold-evoked increases in Ca^{2+} levels (*19-*
451 *12>GCaMP6m ± TNT*) were assessed and the delay in mouth hook retraction was measured.
452 Compared to controls, there is a significant delay in mouth retraction, when CIII md neurons are
453 silenced with tetanus toxin expression. Average n=12 with three stimulations per animal.

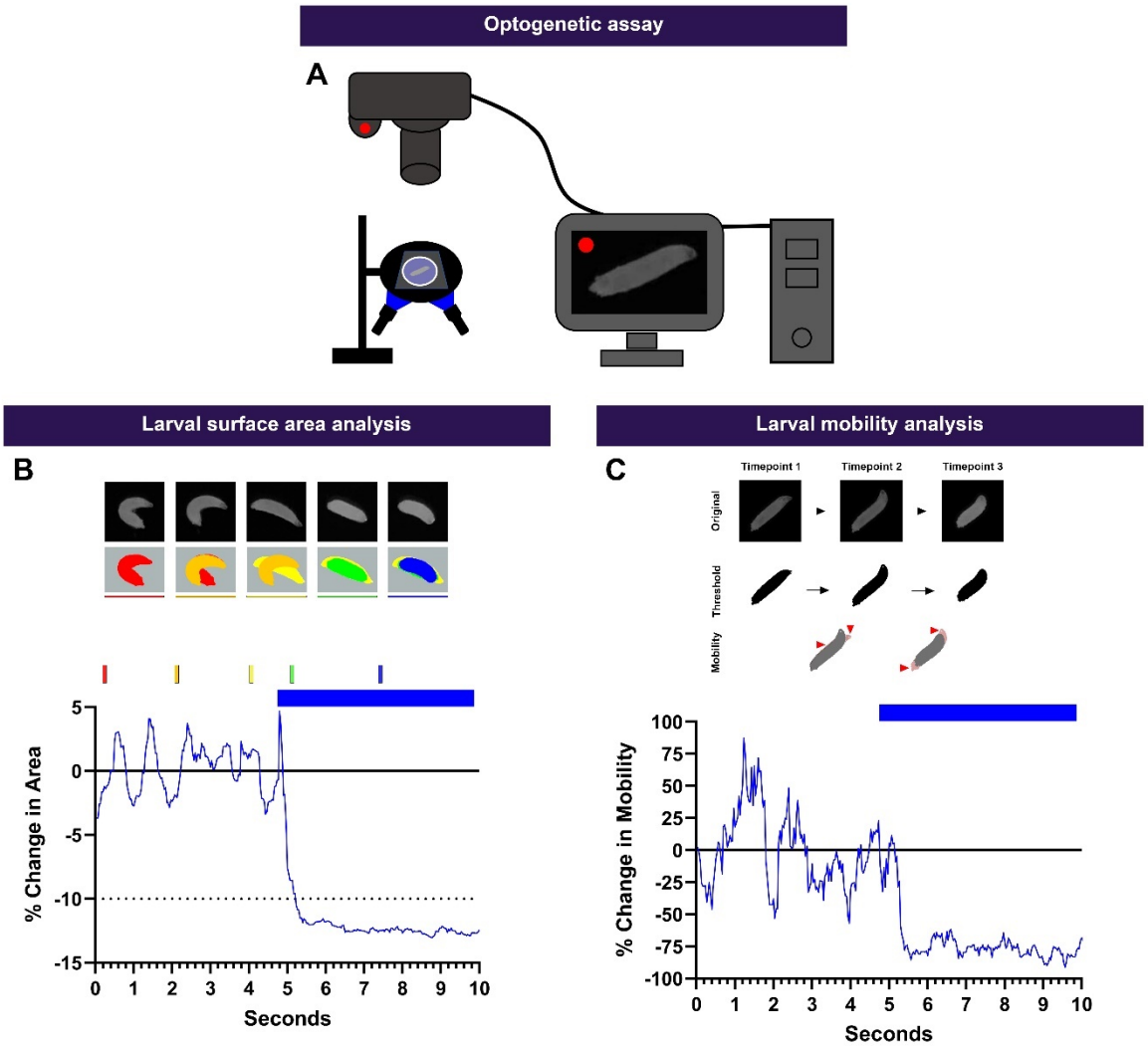

454 **Figure 1-figure supplement 5: *Drosophila* larval neural activation assays using**
455 **optogenetics.** To perform neural activation experiments, we created a custom built optogenetic
456 experimental setup, which has a very high spatial resolution and signal to noise ratio by using
457 principles of dark field illumination. (**A**) Schematic of custom optogenetic rig, where stimulus
458 and video recording are controlled via computer using Noldus Ehtovision. Individual *Drosophila*
459 larva are plated on clear glass plate and illuminated from below with white light. Neuron

activating blue light is also delivered from the below. Individual behavioral videos are automatically cropped and stabilized using custom Fiji macros. (**B-C**) We measured to two variables *Drosophila* larval surface area and mobility. (**B**) Top, image stills from various timepoints before and during optogenetic stimulation of cold sensitive CIII md neurons resulting in contraction (CT) behavioral response. Bottom, percent change in area over time of an individual animal. During baseline, larval locomotion and turns results brief changes in surface area (±2-4%). Whereas upon neural stimulation, there is a distinct lasting reduction in surface area of less than -10%. (**C**) Larval mobility refers to changes in larval postures as measured by changes in occupied space. Since the amount of larval mobility is a function of various intrinsic and extrinsic factors, we normalized larval mobility to baseline period, where there was no neural activation. Top, conceptual framework of how larval mobility is measured. Original videos are motion stabilized in the XY axis and thresholded. Next, we perform image calculations (Mobility=$\text{Frame}_{\text{timepoint 2}} - \text{Frame}_{\text{timepoint 1}}$) to get just the red shaded portions denoting changes in postural locations (red arrowheads). *Drosophila* larval time series mobility data are reported as percent change in mobility, time spent being immobile and percent of immobile animals, or for a genotype percent of animals that are immobile over time, immobility is defined as -25% or more reduction in mobility.

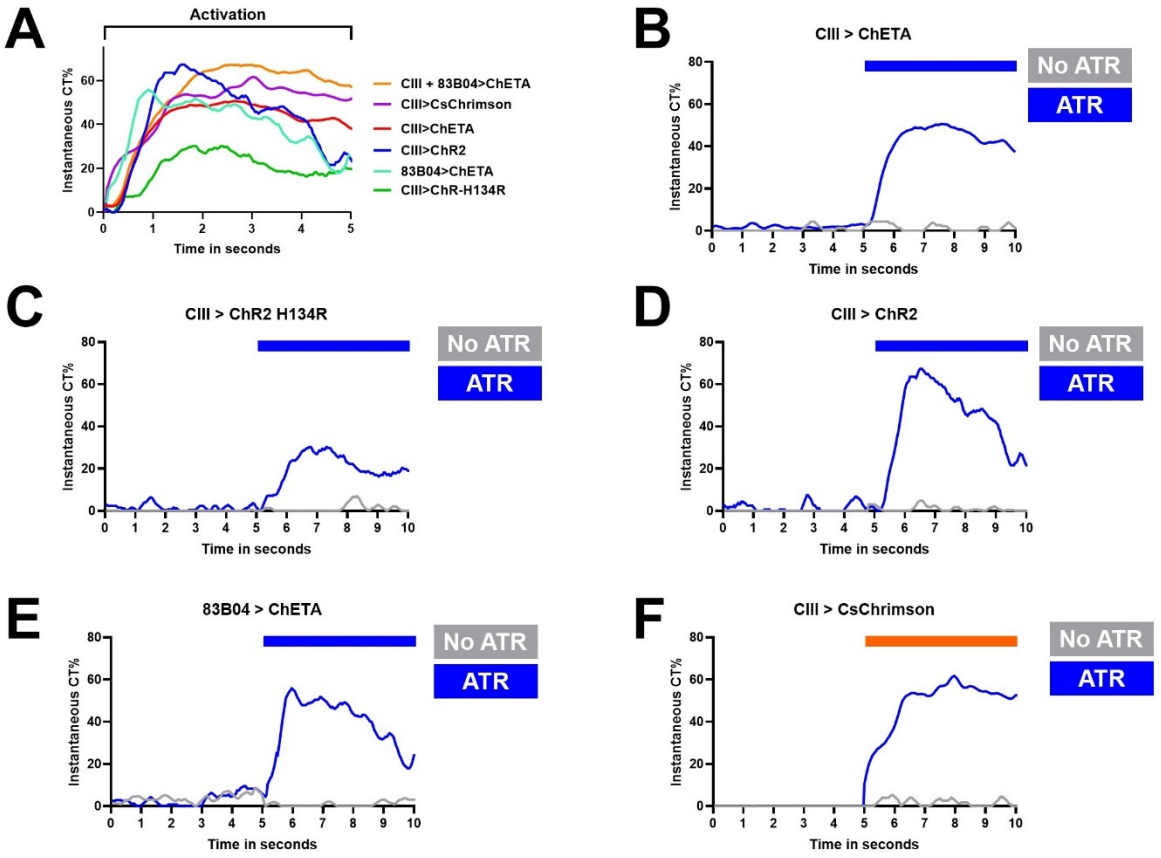

Figure 1-figure supplement 6: Optogenetic activation of CIII md neurons.
(**A**) Activation of CIII md neurons using different optogenetic actuators including *CsChrimson, ChETA, ChR2* and *ChR2-H134R*. Activation of CIII md neurons using either *19-12*^{GAL4} or *83B04*^{GAL4} leads to a contraction response in third instar *Drosophila* larvae. Optogenetic activation of CIII md neurons (*19-12*^{GAL4}) using *CsChrimson, ChETA, ChR2* or *ChR2-H134R* leads to CT responses. Each optogenetic actuator has unique impacts neuronal action potential firing rates leading to slightly different CT responses, however, CIII md neuron activation leads to CT behavioral response. (**B-F**) Represents instantaneous CT percentage responses of no ATR control and with ATR conditions for each of the actuators. (**B-E**) 470nm light was used to activate CIII md neurons. (**F**) CsChrimson is very sensitive to minimal ambient white light exposure. Here, the experiments were conducted in near darkness conditions and thus no pre-stimulus data are recorded. The larval behavior was only recorded upon optogenetic light (617nm) exposure. (**B**) *19-12*^{GAL4}*>ChETA* average n=27. (**C**) *19-12*^{GAL4}*> ChR2-H134R* average n=37. (**D**) *19-12*^{GAL4}*>ChR2* average n=29. (**E**) *83B04*^{GAL4}*>ChETA* average n=30. (**F**) *19-12*^{GAL4}*>CsChrimson* average n=33.

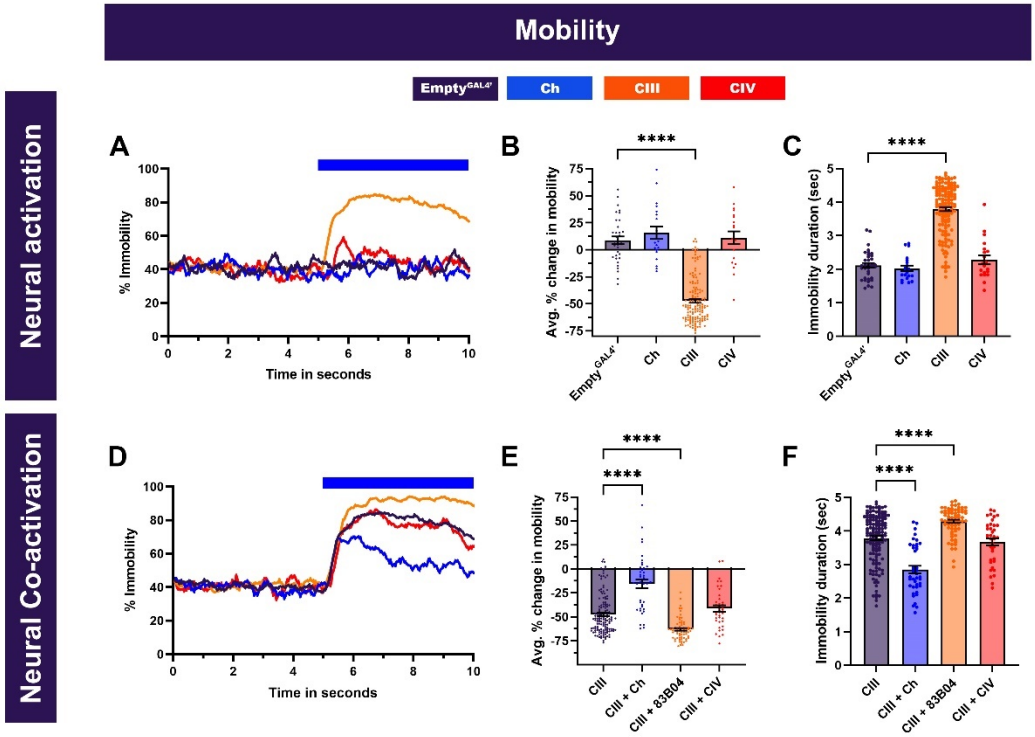

Figure 1-figure supplement 7: *Drosophila* larval mobility pipeline and effects of neural activation and co-activation of sensory neurons on larval mobility (**A-F**) *Drosophila* larval mobility following somatosensory neuron optogenetic activation (**A-C**) and CIII md neuron plus co-activation of Ch, additional CIII *GAL4* driver (*83B04*^{GAL4}) or CIV md neurons (**D-F**). (**A, D**) Instantaneous percent immobility. Blue bar represents optogenetic neural activation. (**B, E**) Average percent change in mobility for each genotype, where greater percent immobility results in larger changes in average mobility. (**C, F**) Immobility duration in seconds during stimulation. Neural activation: *Empty*$^{GAL4'}$ n=35. Ch n=20, CIV n=20. & CIII n=143. Neural co-activation: CIII n=143 and average experimental n=50.Significant differences indicated via asterisks, where ****p<0.0001.

538 **Multisensory integrators are required and facilitate larval contraction response**
539
540 Basin interneurons function as multisensory integrators receiving convergent inputs from
541 mechano-, chemo- and thermo-sensitive peripheral sensory neurons (**Figure 2A, Figure 2-figure**
542 **supplement 1A**). Previous behavioral and functional studies have revealed that Basin
543 interneurons are required for nociceptive escape responses mediated by Ch and CIV md neurons
544 (Ohyama et al., 2015). Both Ch and CIV md neurons play roles in CIII md mediated behavioral
545 responses either in cold nociception and/or can detect cold stimuli. We hypothesized that Basin
546 interneuron function is required downstream of cold nociceptive somatosensory neurons. We
547 evaluated whether Basin interneurons are necessary and sufficient for cold nociception, exhibit
548 cold-evoked increases in calcium response and function downstream of CIII md neurons.
549
550 Silencing Basin interneurons reduces cold-evoked CT
551 Basin interneurons receive somatosensory cues from CIII md neurons, thus we predicted
552 that inhibiting neurotransmitter release from Basin neurons will result in impaired cold-evoked
553 behaviors (**Figure 2A**). We assessed the requirement of all Basin neurons using "pan-" Basin
554 driver lines and also assessed roles of individual Basin neurons using subtype specific driver
555 lines. Neural silencing of all Basin (1-4) neurons, using $R72F11^{GAL4}$, led to significant reductions
556 in cold-evoked CT responses compared to genetic background (w^{1118}) and $Empty^{GAL4'}$ controls
557 (**Figure 2B**). *Drosophila* larvae with impaired Basin (1-4) neuronal function had significant
558 reductions in CT duration, magnitude and cumulative %CT response compared to controls
559 (**Figure 2C-E**). CIII neurons have differential connectivity to individual Basin subtypes (**Figure**
560 **2A**). Therefore, we assessed requirement of Basin-1, -2 or -4 neurons, for which there are
561 previously validated independent driver lines (Jovanic et al., 2016; Ohyama et al., 2015). Tetanus
562 toxin mediated neural silencing of Basin-2 or -4 led to significant reductions in cold-evoked CT
563 response, as measured by cumulative %CT response, CT duration and CT magnitude, compared
564 to controls (**Figure 2B-E**). CIII md neurons do not synapse onto Basin-1 neurons according to
565 the EM-mapped connectome (**Figure 2A**) (Masson et al., 2020), however, Basin-1 & -2 neurons
566 share synaptic connectivity to both feedback and feedforward GABAergic interneurons, both of
567 which are downstream of sensory neurons (Jovanic et al., 2016). Furthermore, Basin-1 neural
568 activation leads to depolarizations in Basin-2 through GABAergic disinhibitory pathway
569 (Jovanic et al., 2016). Therefore, we expected that inhibiting neurotransmitter release in Basin-1
570 neurons would result in reduced cold-evoked responses. Neural silencing of Basin-1 neurons
571 resulted in modest, but significant reductions in cold-evoked responses (**Figure 2B-E**). Impaired
572 Basin neuron signaling results in at least 25% reduction in cold-evoked responses with the
573 strongest reductions for all-Basin, Basin-2 or Basin-4 driver lines (**Figure 2J**).
574
575 Co-activation of Basin interneurons and CIII md somatosensory neurons enhances CT
576 Next, we evaluated whether neural activation of Basin neurons would impair or elicit a
577 CT response. Optogenetic activation of Basin neurons, either using all Basin or individual Basin

578 driver lines, did not elicit a CT response (**Figure 2-figure supplement 2**). But the simultaneous
579 co-activation of CIII md and Basin neurons led to sustained increases in CT responses compared
580 to controls, where only CIII md neurons were activated, across multiple behavioral metrics
581 (**Figure 2F-I**). Coactivation did not result in a change in larval immobility (**Figure 2-figure**
582 **supplement 1B-D**), whereas activation of all Basins led to significantly greater immobility
583 (**Figure 2-figure supplement 1B-D**). These results indicate that Basin neurons are not sufficient
584 for the CT response, but that the combined activation of CIII md and Basins not only suffices but
585 also elicits an even stronger CT response than activating CIII md neurons alone.
586 To parse the contribution of individual Basin neuronal subtypes, we next assessed the
587 role of Basin-1, -2 or -4, and all four Basin together, in either facilitating or suppressing CT
588 responses using our co-activation paradigm (**Figure 2F-I**). Co-activation of Basin-1 or Basin -2
589 with CIII md neurons led to an enhanced CT response compared to controls across all measures
590 of behavioral response including instantaneous %CT response, peak %CT response, CT duration
591 and CT magnitude (**Figure 2F-I**), with a subsequent significant increase in larval immobility
592 (**Figure 2-figure supplement 1B-D**). Basin-2 plus CIII md neuron co-activation led to strong
593 facilitation of CT responses, but surprisingly resulted in significantly reduced immobility
594 (**Figure 2-figure supplement 1B-D**). Unlike for all other Basin neurons tested, Basin-4 and CIII
595 md neuron co-activation led to a suppression of CT response, where peak instantaneous %CT
596 response was similar to controls, however, there was a rapid reduction in instantaneous %CT
597 response compared to controls (**Figure 2F-I**). Both CT duration and CT magnitude were
598 significantly impaired for Basin-4 plus CIII md neuron co-activation compared to controls
599 (**Figure 2H, I**), which also showed significantly lower immobility (**Figure 2-figure supplement**
600 **1B-D**). Interestingly, dual activation of CIII md and all Basin neurons led to weaker CT
601 enhancement compared to co-activation of either Basin-1 or -2 coupled with CIII md neurons
602 (**Figure 2J**), consistent with the finding that co-activation with Basin-4 reduced the CT response.
603 Collectively, second-order Basin neurons are required for cold-evoked responses and specifically
604 Basin-1 and Basin-2 are able to enhance CIII md neuron-evoked behavioral responses.
605
606 <u>CaMPARI reveals Basin-2- and Basin-4 are activated in CT responses</u>
607 To further explore how Basin interneurons function in cold nociception, we sought to
608 investigate cold-evoked Ca^{2+} responses of Basin neurons. Since somatosensory neurons are
609 cholinergic (Salvaterra & Kitamoto, 2001), we expected that Basin neurons postsynaptic to CIII
610 md neurons will exhibit cold-evoked increases in Ca^{2+}. Post-hoc imaging of evoked CaMPARI2
611 fluorescence revealed that Basin neurons have significantly higher F_{red}/F_{green} ratios compared to
612 control, as assessed by all-Basin driver line (**Figure 3A)**. We further investigated Ca^{2+} responses
613 in greater detail using individual driver lines for Basin-1, -2 or -4. Basin-1 neurons are weakly
614 required for cold-evoked CT responses (**Figure 2J**) and coherently do not exhibit cold-evoked
615 increases in Ca^{2+} response (**Figure 3B)**. In contrast, Basin-2 and -4 neurons both exhibit
616 significant increases in Ca^{2+} responses compared to their respective controls (**Figure 3C-D)**.

617 Collectively, Basin-2 and -4 neuron subtypes that are required for cold-evoked CT responses
618 (**Figure 2J**), also exhibit cold-evoked increases in Ca^{2+}.
619
620 <u>CIII md neurons and Basin-2 and -4 neurons are functionally connected</u>
621 Basin-2 and -4 are postsynaptic to CIII md neurons, are required for cold nociception and
622 have cold-evoked increases in Ca^{2+}. Next, we assessed whether CIII md neurons and Basin-2 or -
623 4 neurons are functionally connected. From the EM-reconstructed connectome we predicted that
624 the activation of CIII md neuron will result in increased Ca^{2+} levels of Basin-2 or -4. As
625 expected, optogenetic activation of CIII md neurons led to significant increases in Ca^{2+} levels in
626 Basin-2 neurons, and repeated stimulation of CIII md neurons did not lead to sensitization of
627 Basin-2 Ca^{2+} responses (**Figure 3E, F)**. Previously, it was shown that Ch and CIII md neurons
628 could elicit Ca^{2+} response in Basin-4 neurons (Kaneko et al., 2017), however, in this previous
629 study the authors were unable to determine which of the two sensory neuron cell types led to
630 increases in the Basin-4 Ca^{2+} response (Kaneko et al., 2017). Here, we show that upon
631 specifically activating CIII md neurons, Basin-4 neurons have large, rapid increases in cytosolic
632 Ca^{2+} followed by quick return to baseline levels. In contrast to Basin-2, Basin-4 neurons showed
633 reduced Ca^{2+} responses upon repetitive activations of CIII md neurons (**Figure 3G, H)**.
634 Therefore, CIII md neuron activation is differentially encoded by Basin-2 and -4 neurons, where
635 upon initial stimulation Basin-4 neurons have a much larger CIII md neuron-evoked increase in
636 Ca^{2+} levels but exhibit habituation compared to Basin-2 neurons, which show consistent Ca^{2+}
637 upon repetitive stimulations. Collectively, our data demonstrate that Basin neurons are required
638 for cold-evoked behaviors and Basin-2 and -4 neurons functionally operate downstream of CIII
639 md neurons (**Figure 3-figure supplement 1**).
640
641
642
643
644
645
646
647

648

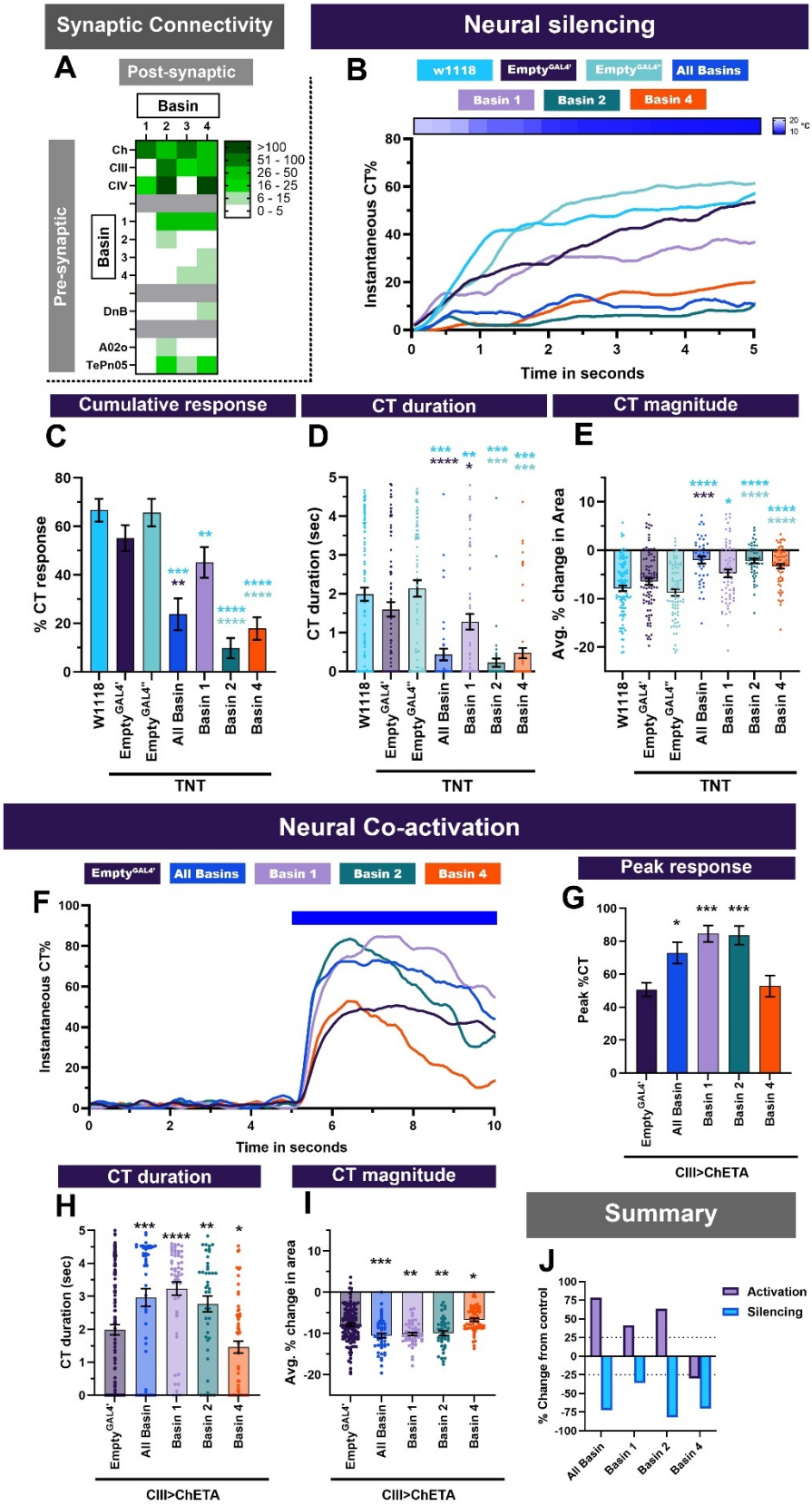
Synaptic Connectivity
Neural silencing
A
Post-synaptic
Basin
Pre-synaptic
Ch
CIII
CIV
DnB
A02o
TePn05
>100
51 - 100
26 - 50
16 - 25
6 - 15
0 - 5
B
w1118
Empty GAL4'
Empty GAL4''
All Basins
Basin 1
Basin 2
Basin 4
Instantaneous CT%
Time in seconds
Cumulative response
CT duration
CT magnitude
C
% CT response
D
CT duration (sec)
E
Avg. % change in Area
W1118
All Basin
TNT
Neural Co-activation
F
Instantaneous CT%
Time in seconds
Peak response
G
Peak %CT
CIII>ChETA
H
CT duration (sec)
I
Avg. % change in area
Summary
J
Activation
Silencing
% Change from control

649 **Figure 2: Multisensory integrator second order neurons are required for cold-evoked**
650 **behaviors and facilitate CIII-evoked behaviors.**
651 (**A**) Basins (1-4) receive inputs from sensory neurons (Ch, CIII md and CIV md), Basins,
652 premotor neuron Down and Back (DnB) and command-like/projection neuron A02o and
653 TePn05. Heatmap plot of pre-synaptic connections to Basins. Synaptic connectivity data was
654 extracted from Neurophyla LMB Cambridge. (https://neurophyla.mrc-lmb.cam.ac.uk/). (**B-E**)
655 Cold-evoked responses of third instar *Drosophila*. Basin (1-4) neurons were silenced by
656 inhibiting neurotransmitter release via cell type specific expression of tetanus toxin (TNT),
657 where All Basin ($R72F11^{GAL4}$), Basin-1 ($R20B01^{GAL4}$), Basin-2 ($SS00739^{splitGAL4}$) and Basin-4
658 ($SS00740^{splitGAL4}$). (**B**) Instantaneous %CT over time. The heatmap on top represents change in
659 temperature over time. (**C**) Cumulative %CT response for a duration of 5 seconds. (**D**) CT
660 duration in seconds. (**E**) CT magnitude as average percent change in area for the duration of
661 stimulus. Controls include w^{1118}, $Empty^{GAL4'}$ (*w;;attP2)* or $Empty^{GAL4''}>TNT$ (*w;attP40;attP2)*.
662 Significant differences were compared to each *GAL4's* respective controls dependent on
663 insertion sites. Significant stars: turquoise stars represent comparison to *w1118*, purple stars
664 represent comparison to $Empty^{GAL4'}>TNT$ and sea green stars represent comparison to
665 $Empty^{GAL4''}>TNT$. Average n = 68. (**F-I**) Neural co-activation of Basin neurons and CIII md
666 neurons. Here each condition represents expression of ChETA in CIII md neurons and plus
667 Basin (1-4) neurons. (**F**) Instantaneous %CT over time. Blue bar represents optogenetic neural
668 activation. (**G**) Peak %CT response during optogenetic stimulation. (**H**) CT duration in seconds
669 during optogenetic stimulation. (**I**) CT magnitude as average percent change in area for the
670 duration of stimulus. Significant stars: purple stars represent comparison to CIII md +
671 $Empty^{GAL4'}>ChETA$. $Empty^{GAL4'}$ n=143 and experimental condition average n =49. (**J**) Overall
672 percent change from control for either neural silencing or neural co-activation. The metrics for
673 neural silencing include cumulative %CT, CT magnitude, and CT duration. The following
674 metrics were used to calculate percent for neural co-activation: cumulative %CT, peak %CT, CT
675 duration and magnitude. Significant differences indicated via asterisks, where *p<0.05,
676 **p<0.01, ***p<0.001, and ****p<0.0001.
677
678
679
680
681
682
683
684
685
686
687

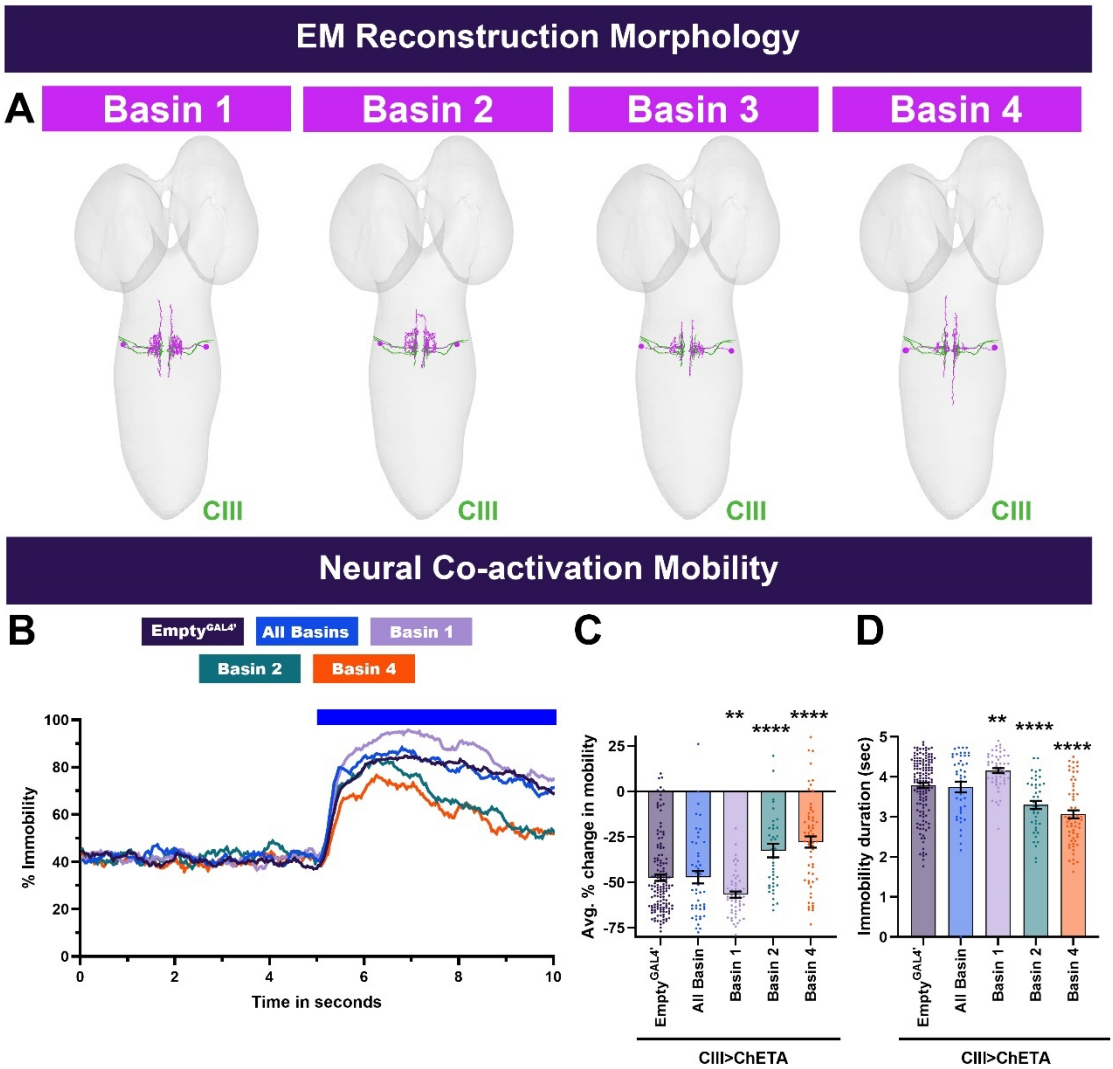

Figure 2-figure supplement 1: Neural reconstructions and larval mobility for multisensory integrator neurons.

(**A**) Individual Basin neuron subtypes (magenta) and CIII md neuron axons (blue). Neural reconstruction data was extracted from Neurophyla LMB Cambridge. (https://neurophyla.mrc-lmb.cam.ac.uk/). (**B-D**) *Drosophila* larval mobility for Basin plus CIII md neuron optogenetic co-activation. (**B**) Instantaneous percent immobility. Blue bar represents optogenetic neural activation. (**C**) Average percent change in mobility for each genotype, where greater percent immobility results in larger changes in average mobility. (**D**) Immobility duration in seconds during stimulation. *Empty$^{GAL4'}$* n=143 and experimental condition n =49. Comparisons to *CIII md + Empty$^{GAL4'}$>ChETA*. Significant differences indicated via asterisks, where **p<0.01, and ****p<0.0001.

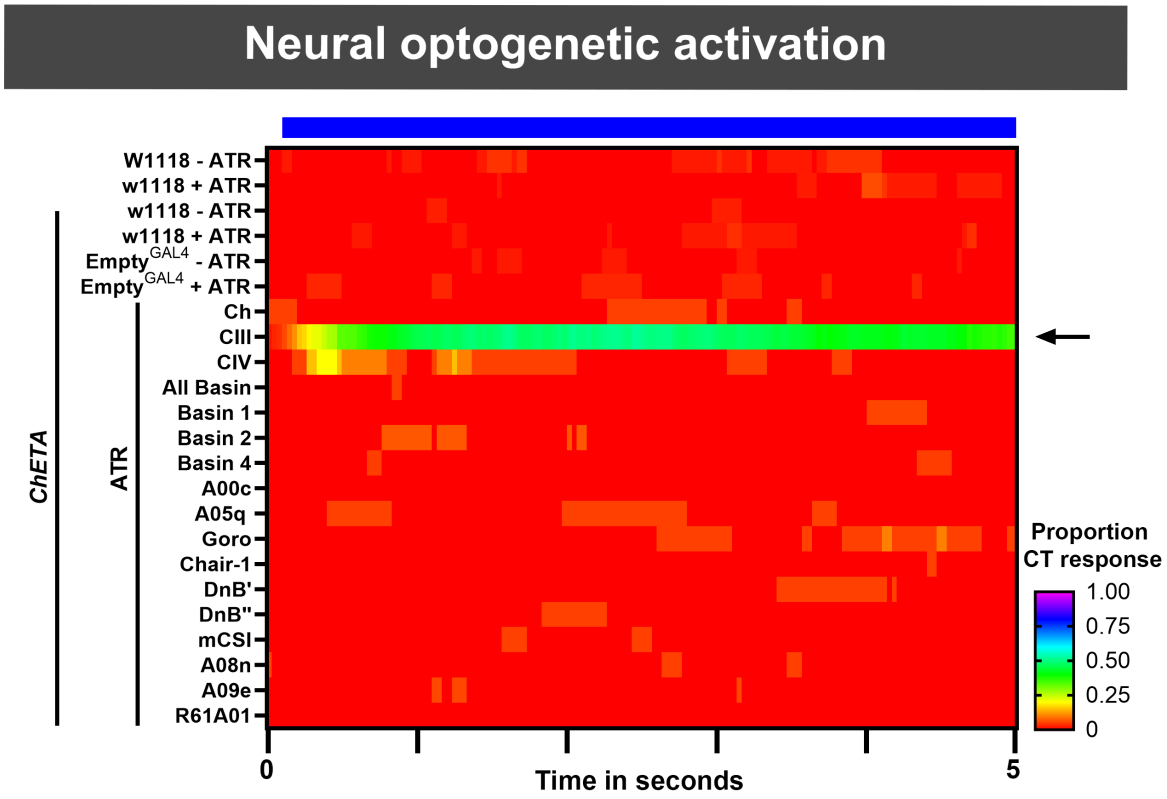

Figure 2-figure supplement 2: Optogenetic activation of individual neuronal cell-types. Heatmap represents optogenetically-evoked instantaneous contraction (CT) proportions of *Drosophila* larvae. Individual neuronal cell-types were optogenetically activated using cell-type specific expression of *ChETA*. Black arrow indicates optogenetic activation of primary cold somatosensory CIII md neurons, which are the only the genotype with high proportions CT. Average n= 31.

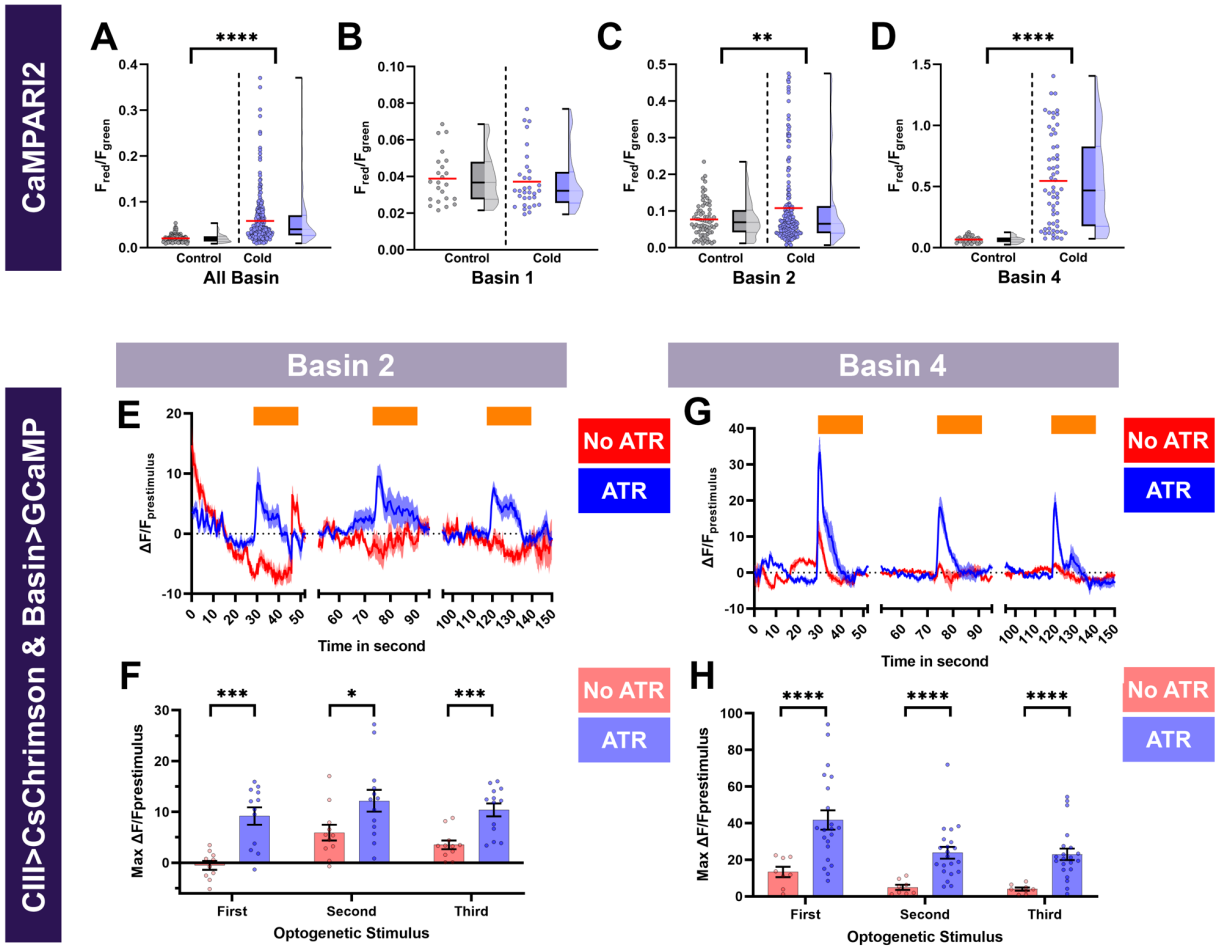

Figure 3: Cold- and CIII- evoked calcium responses of Basin neurons.
(**A-D**) Ca^{2+} responses of Basin neurons upon cold exposure vs. controls (room temperature). Neural responses (CaMPARI2) of Basin neuron cell bodies were analyzed using the following cell type driver lines (**A**) All Basin (*R72F11*^{GAL4}) average n=197, (**B**) Basin-1 (*R20B01*^{GAL4}) average n=27, (**C**) Basin-2 (*SS00739*^{splitGAL4}) average n=119 and (**D**) Basin-4 (*SS00740*^{splitGAL4}) average n=46. CaMPARI2 fluorescence ratio is reported as F_{red}/F_{green}. We report the data as individual datapoints, where the red line represents mean, and hybrid plots (boxplot & violin) for visualizing the distribution and quartiles of data. Significant stars represent $p<0.05$, where comparisons were made to their respective no stimulus controls. (**E-H**) To functionally assess CIII md neuron to Basin-2 or Basin-4 connectivity, we optogenetically activated CIII md neurons (*83B04*^{lexA}*>CsChrimson*) and visualized changes in evoked Ca^{2+} using *Basin-2*^{splitGAL4} or *Basin-4*^{splitGAL4}*>GCaMP6m*. Control: No all *trans*-retinal (ATR) supplemented diet, which is required for optogenetic stimulation in *Drosophila*. Orange bars indicate optogenetic stimulation. (**E,G**) Basin-2 and Basin-4 changes in GCaMP reported as $\Delta F/F_{prestimulus}$, where prestimulus refers to 15 seconds prior to optogenetic stimulation. (**F,H**) Maximum Basin-2 and Basin-4

735 neuronal responses ($\Delta F/F_{prestimulus}$) upon optogenetic stimulation. Average n for each genotype
736 was 13. Comparisons made to relevant controls and significant differences indicated via
737 asterisks, where *p<0.05, **p<0.01, ***p<0.001, and ****p<0.0001.

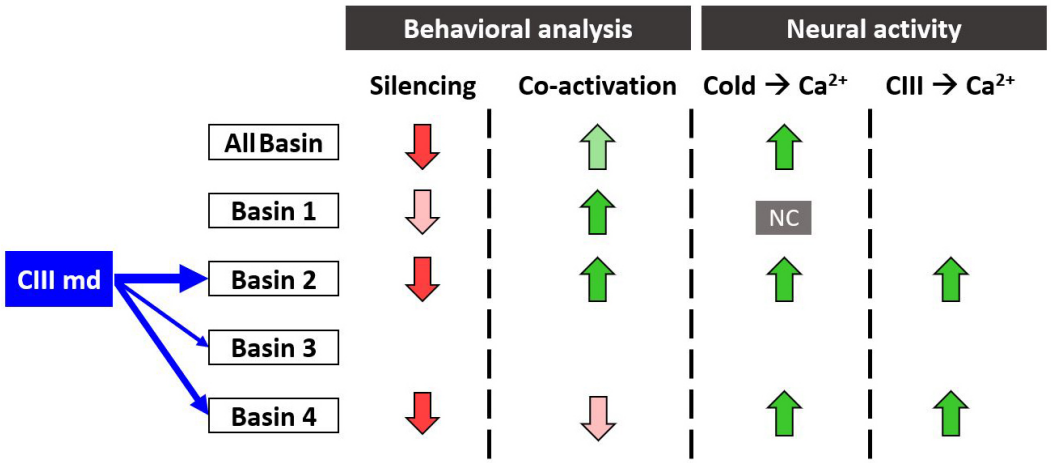

738
739 **Figure 3-figure supplement 1: Summary of behavioral and functional roles of multisensory**
740 **integrators in cold nociception.**
741 Blue arrows indicate strength of synaptic connectivity between the CIII md neurons and second
742 order neurons. In the behavioral analysis column, the arrow direction indicates reduction or
743 enhancement of CT response and shading indicates magnitude of change from control. In neural
744 activity column: NC denotes no significant change in Ca^{2+} response, the arrow direction
745 indicates reduction or enhancement in evoked Ca^{2+} response and shading indicates magnitude of
746 change from control. Empty spaces indicate experimental analyses were not performed.
747
748 **Multisensory integrators function independently of Goro pathway for cold nociception**
749
750 Basin neurons innervate a set of projection neurons (A05q and A00c), which are
751 upstream of a command neuron (Goro) that is responsible for initiating CIV md neuron-mediated
752 nociceptive escape behaviors (**Figure 4A, Figure 4-figure supplement 1A**) (Ohyama et al.,
753 2015). We set out to test whether cold-evoked behavioral responses mediated by CIII md and
754 Basin neurons function through A00c, A05q, and/or Goro neurons. We first assessed whether
755 these neurons are required for cold-evoked behavioral responses (**Figure 4B-E**). Neural silencing
756 of A05q neurons via tetanus toxin led to mild, yet significant reductions in cold-evoked
757 responses, when compared to w^{1118} genetic control (**Figure 4B-E**). Neural silencing of A00c
758 neurons resulted in significantly lower cold-evoked cumulative CT response compared to w^{1118}
759 (**Figure 4C**). There were also significant reductions in CT duration and CT magnitude when
760 A00c neurons were silenced compared to both controls (**Figure 4D, E**). In contrast, the Goro
761 command neuron for nociceptive rolling behavior is not required for cold-evoked CT responses
762 (**Figure 4B-E**). Next, we assessed whether neural activation of these neurons led to evoked CT

763 responses. Like Basin neurons, single cell-type activation of A00c, A05q, or Goro neurons did
764 not lead to CT behavior (**Figure 2-figure supplement 2**). Similarly, optogenetic co-activation of
765 CIII md neurons and A05q or Goro neurons did not lead to significant facilitation of the CT
766 response (**Figure 4F-I**). However, simultaneously co-activating A00c and CIII md neurons led to
767 significant increases in CT duration and CT magnitude (**Figure 4H, I**). There were no changes in
768 *Drosophila* larval immobility upon co-activation of CIII md plus A00c, A05q or Goro neurons
769 (**Figure 4 - figure supplement 1B-D**). Only co-activation of A00c neurons leads to notable
770 enhancement of CIII md mediated CT response, whereas neural silencing of A00c or A05q
771 neurons led to greater than 25% impairment in cold-evoked behavioral responses (**Figure 4J**). In
772 conclusion, the Basin to Goro polysynaptic pathway does not significantly contribute to the cold-
773 evoked CT response.

774

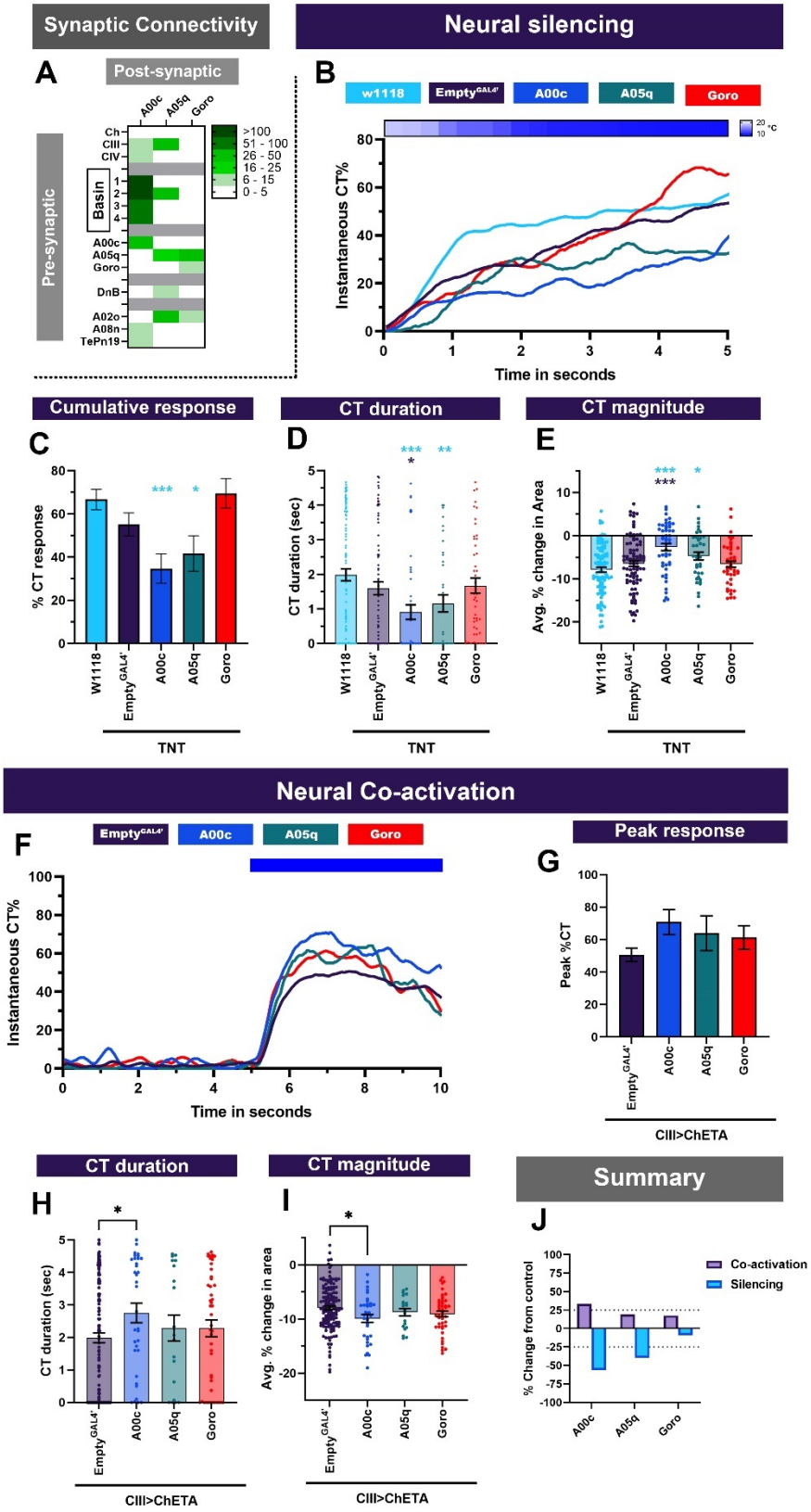
Synaptic Connectivity
Neural silencing
A
Post-synaptic
Pre-synaptic
A00c
A05q
Goro
Ch
CIII
CIV
Basin
1
2
3
4
A00c
A05q
Goro
DnB
A02o
A08n
TePn19
>100
51 - 100
26 - 50
16 - 25
6 - 15
0 - 5
B
w1118
Empty^GAL4'
A00c
A05q
Goro
Instantaneous CT%
Time in seconds
Cumulative response
CT duration
CT magnitude
C
% CT response
D
CT duration (sec)
E
Avg. % change in Area
W1118
Empty^GAL4'
A00c
A05q
Goro
TNT
Neural Co-activation
F
Instantaneous CT%
Time in seconds
Peak response
G
Peak %CT
CIII>ChETA
CT duration
CT magnitude
H
CT duration (sec)
I
Avg. % change in area
Summary
J
Co-activation
Silencing
% Change from control

775 **Figure 4: Projection neurons downstream of Basins and sensory neurons function in cold-**
776 **evoked responses.**
777 (**A**) A00c and A05q primarily receive inputs from Basins and premotor neuron Down and Back
778 (DnB). Goro neurons primarily receive inputs from A05q neurons. Heatmap plot of pre-synaptic
779 connections to downstream neurons. Synaptic connectivity data was extracted from Neurophyla
780 LMB Cambridge. (https://neurophyla.mrc-lmb.cam.ac.uk/). (**B-E**) Cold-evoked responses of
781 third instar *Drosophila*. We used cell-type specific driver lines for downstream neurons to drive
782 expression of tetanus toxin (TNT): A00c ($R71A10^{GAL4}$), A05q ($R47D0^{GAL4}$) and Goro
783 ($R69F06^{GAL4}$). (**B**) Instantaneous %CT over time. The heatmap on top represents change in
784 temperature over time. (**C**) Cumulative %CT response for a duration of 5 seconds. (**D**) CT
785 duration in seconds. (**E**) CT magnitude as average percent change in area for the duration of
786 stimulus. Controls include w^{1118} and $Empty^{GAL4}$ *(w;;attP2)*. For each genotype average n=64.
787 Significant stars: turquoise stars represent comparison to w^{1118} and purple stars represent
788 comparison to $Empty^{GAL4}$*>TNT*. (**F-I**) Neural co-activation of downstream neurons and CIII md
789 neurons. Here each condition represents expression of ChETA in CIII md neurons plus A00c,
790 A05q or Goro neurons. (**F**) Instantaneous %CT over time. Blue bar represents optogenetic neural
791 activation. (**G**) Peak %CT response during optogenetic stimulation. (**H**) CT duration in seconds
792 during optogenetic stimulation. (**I**) CT magnitude as average percent change in area for the
793 duration of stimulus. Significant purple stars represent comparison to *CIII md +*
794 $Empty^{GAL4}$*>ChETA*. $Empty^{GAL4}$ n=143 and experimental condition average n =33. (**J**) Overall
795 percent change from control for either neural silencing or neural co-activation. The metrics for
796 neural silencing include cumulative %CT, CT magnitude, and CT duration. The following
797 metrics were used to calculate percent for neural co-activation: cumulative %CT, peak %CT, CT
798 duration and magnitude. Significant differences indicated via asterisks, where *$p<0.05$,
799 **$p<0.01$, and ***$p<0.001$.
800
801
802
803
804
805
806
807
808
809
810

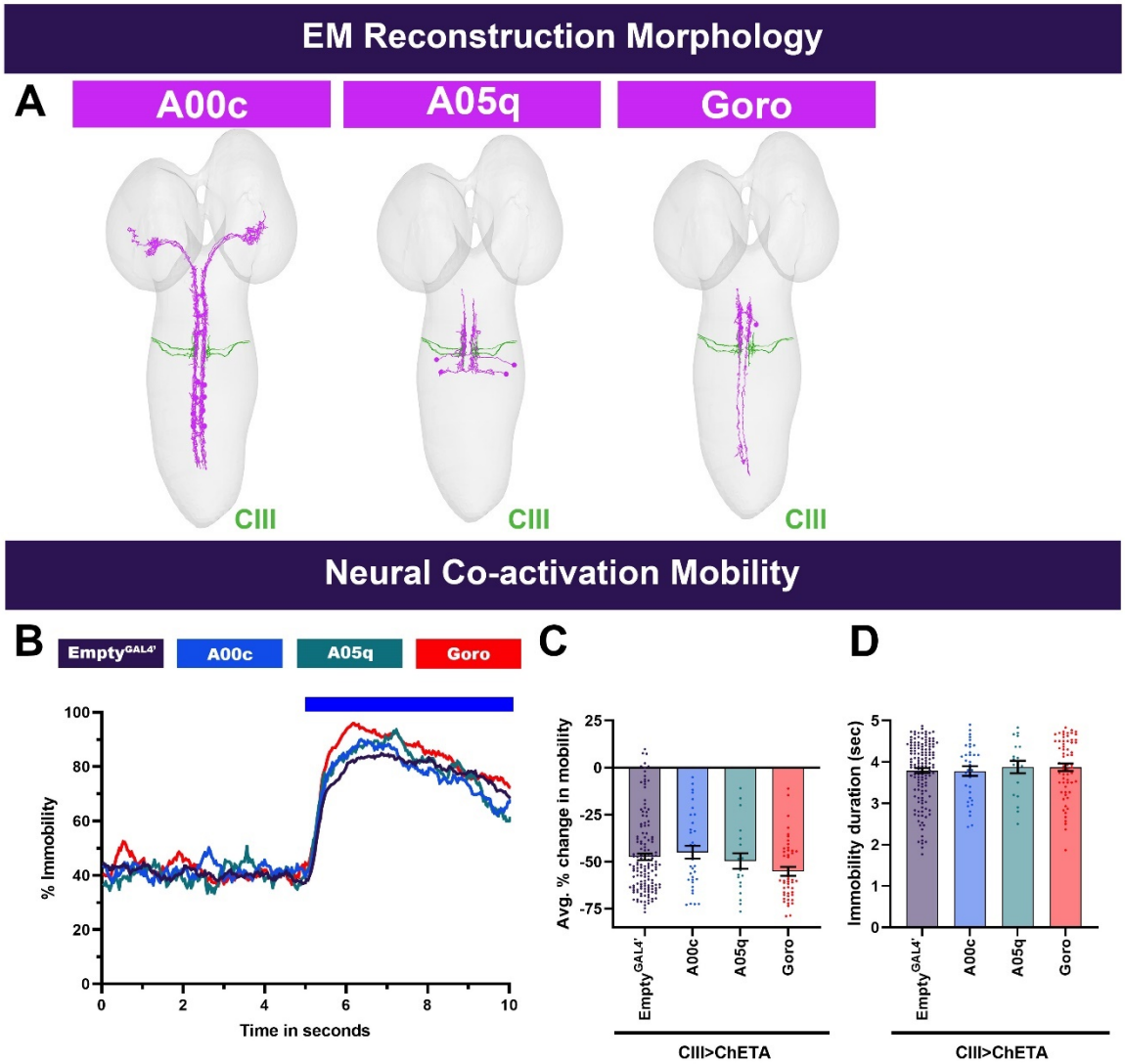

Figure 4-figure supplement 1: Neural reconstructions and larval mobility for A00c, A05q, and Goro neurons.
(**A**) Individual interneuron subtypes (magenta) and CIII md neuron axons (blue). Neural reconstruction data was extracted from Neurophyla LMB Cambridge. (https://neurophyla.mrc-lmb.cam.ac.uk/). (**B-D**) *Drosophila* larval mobility for A00c, A05q or Goro neurons plus CIII md neuron optogenetic coactivation. (**B**) Instantaneous percent immobility. Blue bar represents optogenetic neural activation. (**C**) Average percent change in mobility for each genotype, where greater percent immobility results in larger changes in average mobility. (**D**) Immobility duration in seconds during stimulation. Significant stars represent $p<0.05$, where stars represent comparison to CIII md + *Empty$^{GAL4'}$>ChETA*. Empty^{GAL4} n=143 and experimental condition average n =33.

823
824 **Premotor neurons function downstream of CIII md neurons to mediate cold nociceptive**
825 **responses**
826
827 Select *Drosophila* larval premotor neurons were previously implicated in CIV-mediated
828 nociceptive escape responses. Specifically, DnB premotor neurons are involved in noxious
829 thermal stimulus-evoked c-bending and rolling behavior (Burgos et al., 2018; Lopez-Bellido et
830 al., 2019). *Drosophila* larvae also roll in response to activation of mCSI premotor neurons, which
831 are synaptically connected to CIV md neurons and predicted to be A02m/n neurons from EM
832 connectomes (Lopez-Bellido et al., 2019; Yoshino et al., 2017). Additionally, Chair-1 (A10a)
833 premotor neurons have been implicated in anemotaxis (Jovanic et al., 2019). Collectively, these
834 nocifensive premotor neurons primarily receive inputs from both primary sensory neurons (CIII
835 & CIV md) and multisensory integrators (Basin-2 & -4) (**Figure 5A, Figure 5-figure**
836 **supplement 1A**). CIII md neurons have additional synaptic connectivity with intersegmental
837 feedback circuitry involved in locomotion, where Ifb-fwd (A01d3) is active during forward
838 locomotion and Ifb-bwd (A27k) is active during backwards locomotion (Kohsaka et al., 2019).
839 The intersegmental feedback circuit neurons (A01d3 and A27k) are interconnected via A02e and
840 A02g (Kohsaka et al., 2019). GABAergic A31k premotor neuron is downstream of A01d3 and is
841 responsible for inhibiting motor activity causing relaxation of the larval body. Lastly, A02f has
842 been implicated in delaying nocifensive behavioral responses (Garner, 2020). We predicted that
843 select premotor neurons are required for cold-evoked responses and function downstream of CIII
844 md neurons in a stimulus-specific manner.
845 Inhibition of neural transmission via cell type specific expression of tetanus toxin in
846 individual premotor neurons led to reduced cold-evoked responses in *Drosophila* larvae (**Figure**
847 **5B-E**). Silencing Chair-1 neurons resulted in the strongest reduction of cold-evoked CT
848 responses, where instantaneous %CT was the lowest of all premotor neuron subtypes tested
849 (**Figure 5B**). CT duration, magnitude and cumulative percent response were all significantly
850 reduced compared to controls (**Figure 5B-E**). Impairment in Chair-1 neuronal signaling leads to
851 75% reduction from controls in cold-evoked behaviors (**Figure 5J**). We silenced DnB neurons
852 using two independent cell-type specific driver lines (DnB' ($IT4051^{GAL4}$) & DnB''($IT412^{GAL4}$)),
853 where both resulted in reduced instantaneous %CT response, along with significant reductions in
854 CT duration and magnitude compared to controls (**Figure 5B-E**). Silencing mCSI ($R94B10^{GAL4}$)
855 neurons also resulted in significantly reduced cold-evoked CT responses compared to controls
856 (**Figure 5B-E**). DnB or mCSI inhibition of neurotransmitter release leads to approximately 50%
857 reduction in cold-evoked CT responses (**Figure 5J**). Furthermore, we silenced premotor neurons
858 previously implicated in locomotion (A01d3, A27k, A02e, A02g, A31k) or delaying nocifensive
859 responses (A02f), this did not lead to significant changes in cold-evoked CT responses (**Figure**
860 **5-figure supplement 2**). Collectively, the previously implicated nocifensive premotor neurons
861 are required for cold-evoked behavioral responses.

862 Based on EM connectivity and neural silencing experiments, we predicted that activation
863 of these premotor neurons would be sufficient for *Drosophila* larval CT response. First, we
864 found that activation of premotor neurons alone did not evoke CT response (**Figure 2-figure**
865 **supplement 2**). Next, we performed optogenetic co-activation of CIII md and premotor neuron
866 subtypes. Chair-1 neuron co-activation with CIII md neuron did not have an effect on CT
867 responses (**Figure 5F-I**), however, there was a reduction in larval immobility, where average
868 mobility was increased and duration of immobility was reduced compared to when only CIII md
869 neurons are activated (**Figure 5-figure supplement 1B-D**). Simultaneous activation of CIII md
870 neurons and DnB or mCSI both led to significant increases in CT responses, as measured by
871 peak CT response, CT duration or magnitude, compared to CIII md neuron activation alone
872 (**Figure 5F-I**). DnB and CIII md neuron co-activation led to short lived, subtle but insignificant
873 increases in larval immobility (**Figure 5-figure supplement 1B-D**). Co-activation of mCSI and
874 CIII md neurons resulted in mild reductions in larval immobility (**Figure 5-figure supplement**
875 **1B-D**). These data reveal DnB and mCSI neuronal activity enhances CIII md neuron mediated
876 CT responses.
877 Since these premotor neurons are postsynaptic to CIII md neurons and their activity is
878 required for proper cold-evoked behaviors, we predicted that either activation of CIII md neurons
879 or exposure to cold would cause increases in Ca^{2+}. To test this prediction, we selectively
880 expressed the Ca^{2+} integrator CaMPARI2 in premotor neurons. Unexpectedly, there was no
881 change in cold-evoked Ca^{2+} levels in mCSI or Chair-1 neurons (**Figure 6A-B**). Noxious cold
882 exposure did however lead to significant Ca^{2+} increases in DnB neurons (**Figure 6C-D**). To
883 further assess how CIII md neuronal activity affects DnB function, we optogenetically activated
884 CIII md neurons and assessed evoked Ca^{2+} levels of DnB using GCaMP6. Interestingly,
885 *Drosophila* larvae raised without all *trans*-retinal, a requisite light sensitive cofactor for
886 optogenetic experiments, also had a mild light-evoked increase in Ca^{2+} (**Figure 6E, F**). CIII md
887 neuron optogenetic activation led to significant increases in DnB Ca^{2+} levels that slowly returned
888 to baseline levels (**Figure 6E, F**). Upon repeated CIII md neuron activations, DnB neurons
889 exhibit a blunted Ca^{2+} response relative to initial stimulation (**Figure 6E, F**). Taken together we
890 find that premotor neuronal function is required for cold nociception and premotor neuron
891 activity can facilitate CIII md neuron mediated CT responses (**Figure 6-figure supplement 1**).
892
893
894
895
896
897
898
899
900
901

902

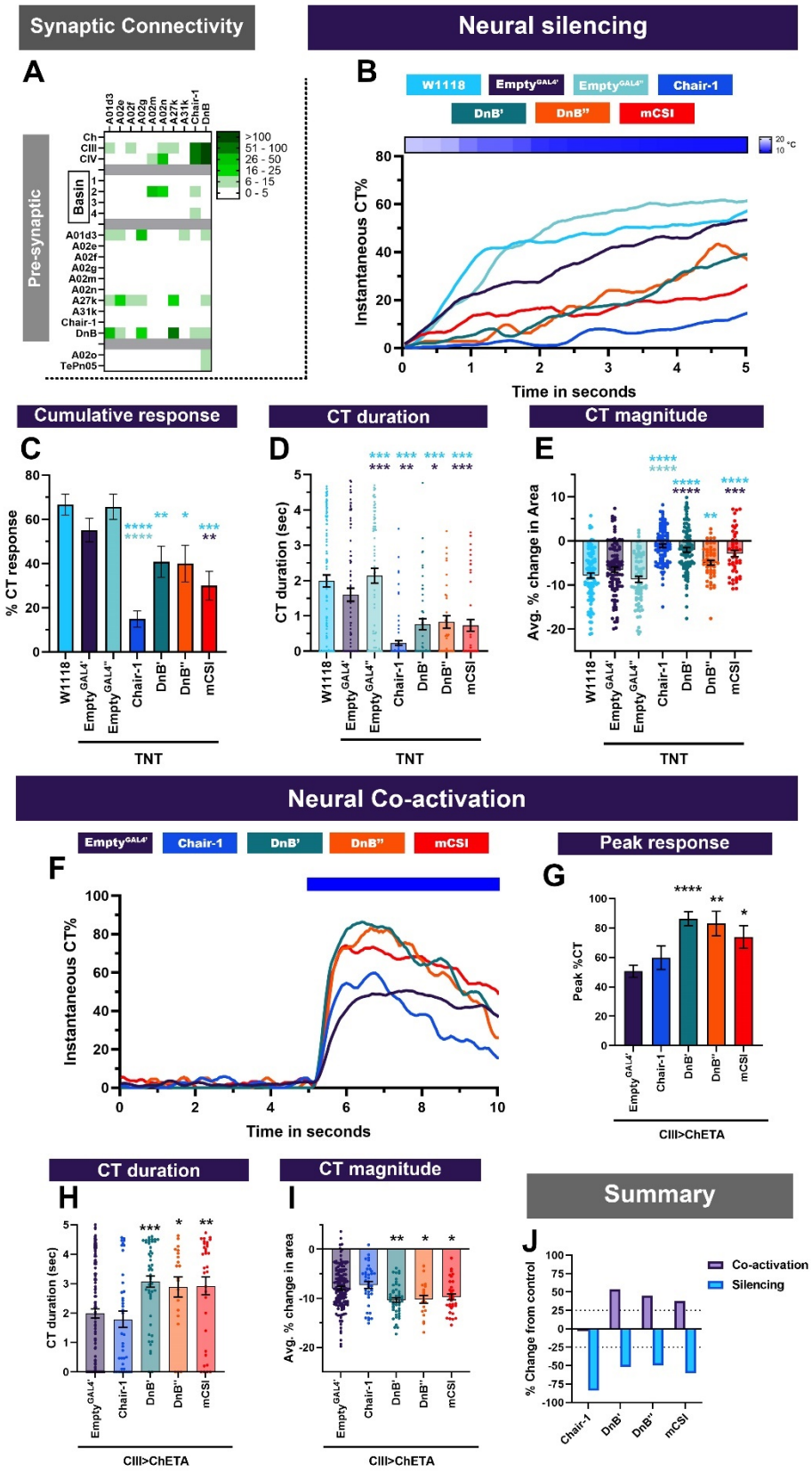
Synaptic Connectivity
Neural silencing
A
B
Pre-synaptic
Basin
Instantaneous CT%
Time in seconds
Cumulative response
CT duration
CT magnitude
C
D
E
% CT response
CT duration (sec)
Avg. % change in Area
TNT
Neural Co-activation
F
G
Peak response
Peak %CT
CIII>ChETA
H
I
CT duration
CT magnitude
Summary
J
Co-activation
Silencing
% Change from control

903
904
905 **Figure 5: Premotor neurons downstream of sensory neurons and Basin neurons are**
906 **required for cold-evoked responses.**
907 (**A**) Chair-1 (A10a), A02m/n (predicted to be mCSI neurons) and Down and Back (DnB,
908 A09l) primarily receive inputs from Basins, CIII md and CIV md neurons. Heatmap plot of pre-
909 synaptic connections to premotor neurons. Synaptic connectivity data was extracted from
910 Neurophyla LMB Cambridge. (https://neurophyla.mrc-lmb.cam.ac.uk/). (**B-E**) Cold-evoked
911 responses of third instar *Drosophila*. Premotor neurons were silenced by inhibiting
912 neurotransmitter release via cell type specific expression of tetanus toxin (TNT), where Chair-1
913 (*SS00911*^{splitGAL4}), DnB' (*IT4015*^{GAL4}), DnB'' (*IT412*^{GAL4}) and mCSI (*R94B10*^{GAL4}). (**B**)
914 Instantaneous %CT over time. The heatmap on top represents change in temperature over time.
915 (**C**) Cumulative %CT response for a duration of 5 seconds. (**D**) CT duration in seconds. (**E**) CT
916 magnitude as average percent change in area for the duration of stimulus Controls include *w*^{1118},
917 *Empty*$^{GAL4'}$ (*w;;attP2)* or *Empty*$^{GAL4''}$*>TNT* (*w;attP40;attP2)*. Significant differences were
918 compared to each *GAL4's* respective controls dependent on insertion sites. Significant stars:
919 turquoise stars represent comparison to *w*^{1118}, purple stars represent comparison to
920 *Empty*$^{GAL4'}$*>TNT* and sea green stars represent comparison to *Empty*$^{GAL4''}$*>TNT*. For each
921 genotype average n=71. (**F-I**) Neural co-activation of premotor neurons and CIII md neurons.
922 Here each condition represents expression of ChETA in CIII md neurons plus premotor neurons.
923 (**F**) Instantaneous %CT over time. Blue bar represents optogenetic neural activation. (**G**) Peak
924 %CT response during optogenetic stimulation. (**H**) CT duration in seconds during optogenetic
925 stimulation. (**I**) CT magnitude as average percent change in area for the duration of stimulus.
926 *Empty*$^{GAL4'}$ n=143 and experimental condition average n =35. Significant stars represent $p<0.05$,
927 where purple stars represent comparison to *CIII md + Empty*$^{GAL4'}$*>ChETA*. (**J**) Overall percent
928 change from control for either neural silencing or neural co-activation. The metrics for neural
929 silencing include cumulative %CT, CT magnitude, and CT duration. The following metrics were
930 used to calculate percent for neural co-activation: cumulative %CT, peak %CT, CT duration and
931 magnitude. Significant differences indicated via asterisks, where *$p<0.05$, **$p<0.01$,
932 ***$p<0.001$, and ****$p<0.0001$.
933
934
935
936
937
938
939
940
941
942
943
944
945
946

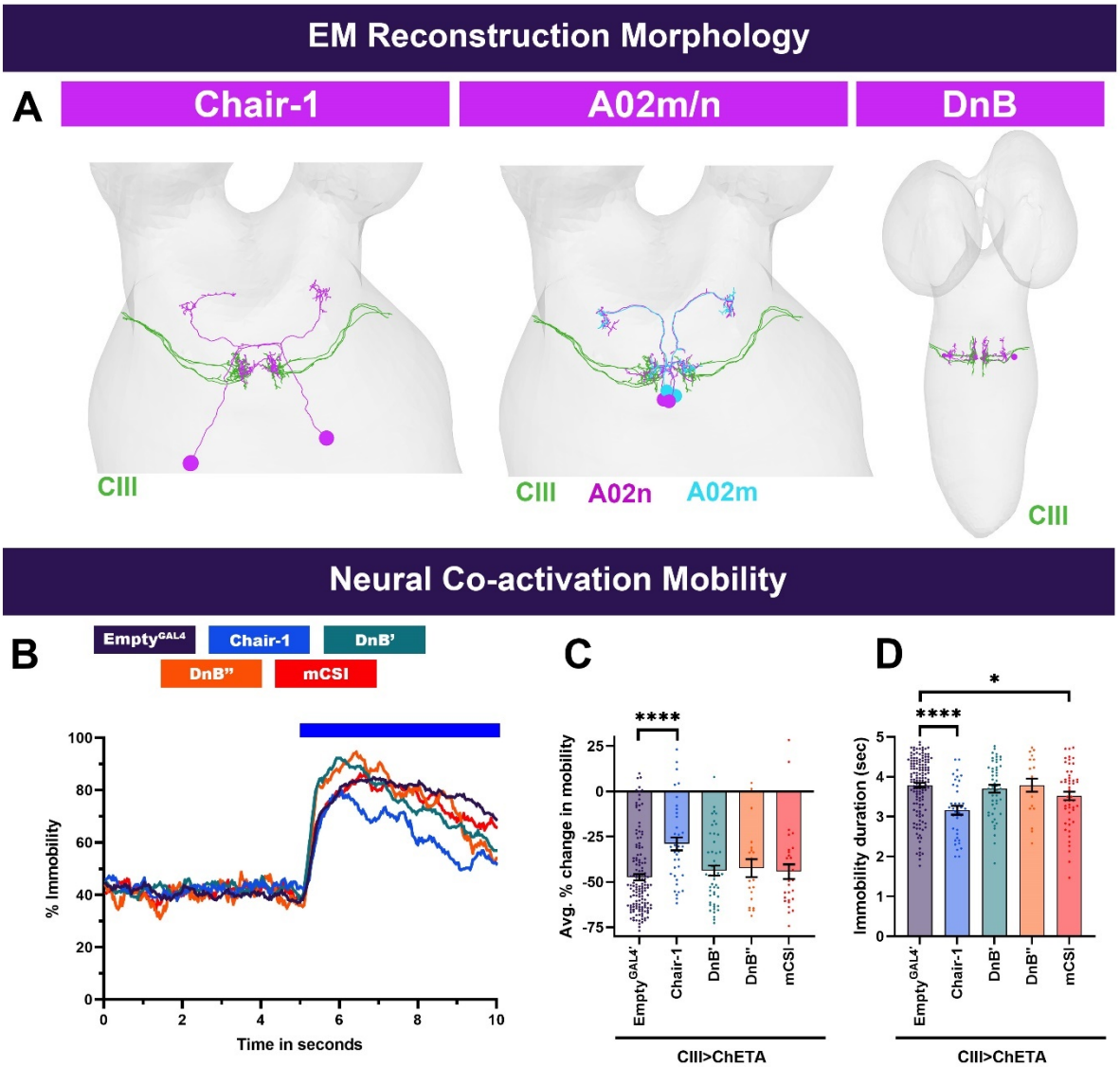

Figure 5-figure supplement 1: Neural reconstructions and larval mobility for premotor neurons.

(**A**) Individual premotor neuron subtypes (magenta/green) and CIII md neuronal axons (blue). Neural reconstruction data was extracted from Neurophyla LMB Cambridge. (https://neurophyla.mrc-lmb.cam.ac.uk/). (**B-D**) *Drosophila* larval mobility observed with premotor neurons plus CIII md neuron optogenetic coactivation. (**B**) Instantaneous percent immobility. Blue bar represents optogenetic neural activation. (**C**) Average percent change in mobility for each genotype, where greater percent immobility results in larger changes in average mobility. (**D**) Immobility duration in seconds during stimulation. *Empty$^{GAL4'}$* n=143 and

experimental condition average n =35. Comparison to *CIII md + Empty$^{GAL4'}$>ChETA*. Significant differences indicated via asterisks, where *p<0.05, and ****p<0.0001.

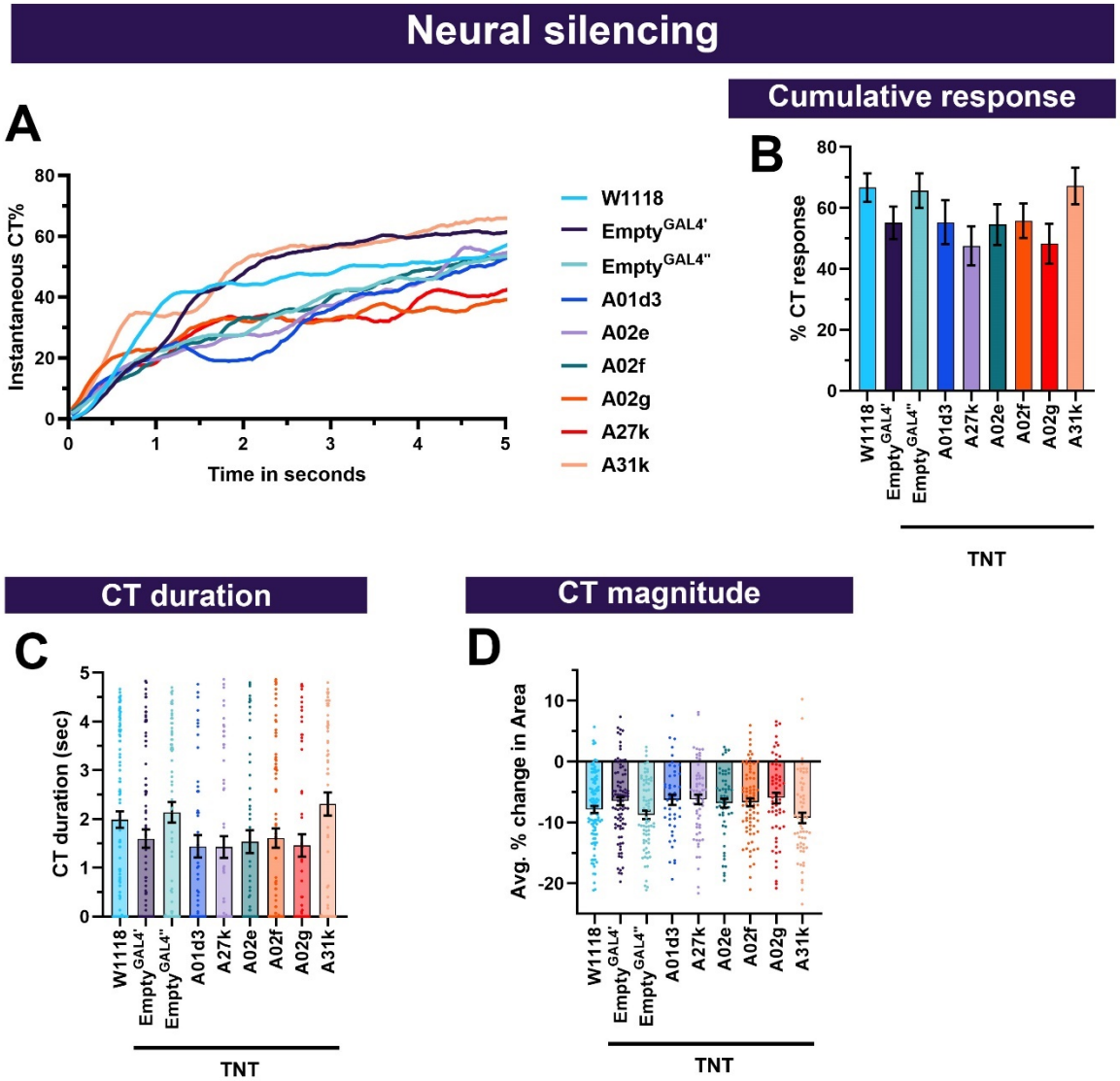

Figure 5-figure supplement 2: Premotor network neurons are not required for cold-evoked responses. (**A-D**) Cold-evoked responses of third instar *Drosophila* larvae. Premotor neurons were silenced by inhibiting neurotransmitter release via cell type specific expression of tetanus toxin (TNT), using these driver lines A01d3 (*SS02065^{splitGAL4}*), A27k (*SS026694^{splitGAL4}*), A02e (*R70C01^{GAL4}*), A02f (*SS01792^{GAL4}*), A02g (*R36G02^{GAL4}*), and A31k (*SS04399^{splitGAL4}*). (**A**) Instantaneous %CT over time. The heatmap on top represents change in temperature over time. (**B**) Cumulative %CT response for a duration of 5 seconds. (**C**) CT duration in seconds. (**D**) CT magnitude is an average percent change in area for the duration of stimulus. Controls include *w^{1118}*, *Empty$^{GAL4'}$* (w;;attP2) or *Empty$^{GAL4''}$*>TNT (w;attP40;attP2). Significant differences were compared to each GAL4's respective controls dependent on insertion sites. There were no significant differences detected. Therefore, the following premotor neurons (A01d3, A27k,

A02e, A02f, A02g, and A31k) are not required for cold-evoked CT responses. For each genotype average n=68.

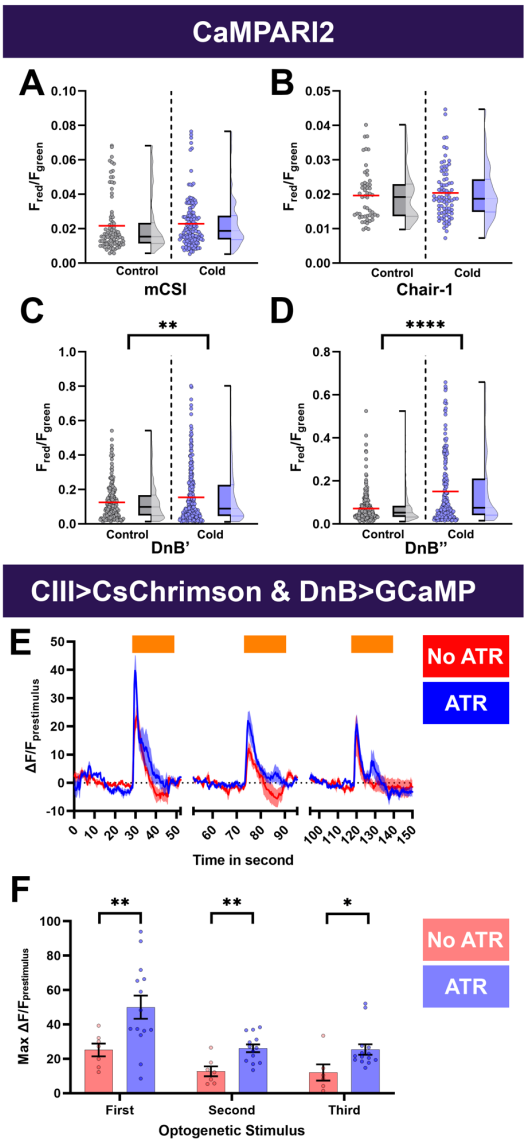

Figure 6: Cold- and CIII- evoked calcium responses of premotor neurons.
(**A-D**) Ca^{2+} responses of premotor neurons upon cold exposure vs. controls (room temperature). Neural responses (CaMPARI2) of premotor neuron cell bodies were analyzed using the following cell type driver lines (**A**) mCSI (*R94B10*^{GAL4}) average n=116, (**B**) Chair-1 (*SS00911*^{splitGAL4}) average n=66, (**C**) DnB' (*IT4015*^{GAL4}) average n=250, and (**D**) DnB'' (*IT412*^{GAL4}) average n=245, CaMPARI2 fluorescence ratio is reported as F_{red}/F_{green}. We report the data as individual datapoints, where the red line represents mean, and hybrid plots (boxplot & violin) for visualizing the distribution and quartiles of data. Significant stars represent $p<0.05$,

982 where comparisons were made to their respective no stimulus controls. (**E-F**) To functionally
983 assess CIII md neuron to DnB connectivity, we optogenetically activated CIII md neurons
984 (*83B04^{lexA}>CsChrimson*) and visualized changes in evoked Ca^{2+} using *DnB-GAL4>GCaMP6m*.
985 Control: No ATR supplemented diet, which is required for optogenetic stimulation in
986 *Drosophila*. Orange bars indicate optogenetic stimulation. (**E**) DnB changes in GCaMP reported
987 as $\Delta F/F_{prestimulus}$, where prestimulus refers to 15 seconds prior to optogenetic stimulation. (**F**)
988 Maximum DnB neuronal responses ($\Delta F/F_{prestimulus}$) upon optogenetic stimulation. Average n=10.
989 Significant differences indicated via asterisks, where *p<0.05, **p<0.01, and ****p<0.0001.
990

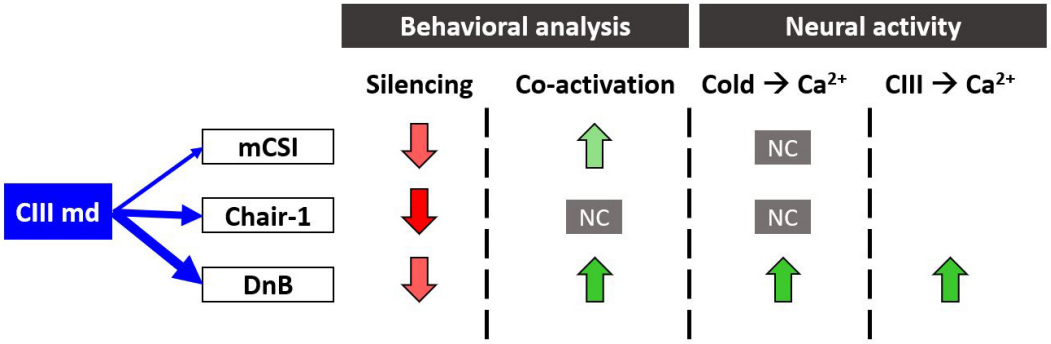

991
992
993
994 **Figure 6-figure supplement 1: Summary of behavioral and functional roles of premotor**
995 **neurons in cold nociception.**
996 Blue arrows indicate strength of synaptic connectivity between the CIII md neurons and second
997 order neurons. In the behavioral analysis column, the arrow direction indicates reduction or
998 enhancement of CT response and shading indicates magnitude of change from control. In neural
999 activity column: NC denotes no significant change in Ca^{2+} response, the arrow direction
1000 indicates reduction or enhancement in evoked Ca^{2+} response and shading indicates magnitude of
1001 change from control. Empty spaces indicate experimental analyses were not performed.
1002
1003
1004
1005 **Ascending interneurons are required for cold nociceptive responses**
1006
1007 Sensory, second order multisensory integration neurons (Basins) and a premotor neuron
1008 (DnB) have further direct synaptic connectivity to a set of projection neurons including A09e,
1009 A08n, A02o, dILP7 and *R61A01^{GAL4}* labeled neurons (labels: A10j, A09o, TePn04, TePn05) that
1010 have previously been implicated in anemotaxis, mechanosensory or chemosensory evoked
1011 behavioral responses (Hu et al., 2017; Jovanic et al., 2019; Kaneko et al., 2017; Masson et al.,
1012 2020; Takagi et al., 2017; Vogelstein et al., 2014). Briefly, A09e receives synaptic inputs from

1013 CIII md, CIV md, A08n, DnB, and TePn05 (**Figure 7A, Figure 7-figure supplement 1A**). A09e
1014 and CIII md neurons are both required for *Drosophila* larval anemotaxis (Jovanic et al., 2019;
1015 Masson et al., 2020). A08n primarily receives inputs from CIV md neurons and very few inputs
1016 from CIII md neurons (**Figure 7A, Figure 7-figure supplement 1A**). However, *Drosophila*
1017 third instar larval synaptic connectivity visualization using GFP reconstituted across synaptic
1018 partners (GRASP) revealed that A08n are not synaptic partners of CIII md neurons (Kaneko et
1019 al., 2017). A08n neurons function downstream of CIV md neurons for noxious chemical and
1020 mechanical nociception (Hu et al., 2017; Kaneko et al., 2017) and neural activation of Ch and
1021 CIII md neurons does not lead to activation of A08n neurons (Tenedini et al., 2019). *R61A01*^{GAL4}
1022 labeled neurons receive inputs from Ch, CIII md, CIV md, Basins, DnB, and A09e (**Figure 7A,**
1023 **Figure 7-figure supplement 1A**). Neurons labeled by *R61A01*^{GAL4} have been implicated in
1024 mechanosensation (Masson et al., 2020). CIII md neurons synapse onto two additional neurons
1025 that function in processing mechanosensitive information A02o and dILP7. A02o neurons are
1026 command-like neurons required for directional avoidant responses to noxious touch (Takagi et
1027 al., 2017), whereas dILP7 neurons are required for noxious mechanical and/or UV/blue light
1028 avoidance using short neuropeptide F or Ilp7, respectively (Hu et al., 2017; Imambocus et al.,
1029 2022). CIII md to dILP7 synaptic connectivity is observed in the first instar larval EM
1030 connectome, however, assessing synapse connectivity using activity-dependent GRASP in third
1031 instar larvae, there was no detectable connectivity (Hu et al., 2017). We assessed whether the
1032 following projection neurons A09e, A08n, neurons in the expression pattern of the GAL4 line
1033 *R61A01* (A10j, A09o, TePn04, TePn05), A02o and dILP7 neurons are required for cold-evoked
1034 behaviors and function in conjunction with CIII md neurons for generating CT behavioral
1035 response.
1036 Neural silencing of projection neurons using cell specific expression of tetanus toxin led
1037 to impairments in cold-evoked behaviors. Neurotransmission inhibition in projection neurons
1038 (A09e and *R61A01*) that receive strong connectivity from CIII md neurons led to significant
1039 reductions in all the CT behavioral metrics that we analyzed (**Figure 7B-E**). As expected, A08n
1040 neurons, which primarily receive inputs form CIV md neurons, are not required for cold-evoked
1041 CT response (**Figure 7B-E**). Whereas neural silencing of A09e or *R61A01* neurons led to greater
1042 than 50% reduction in cold-evoked responses from controls (**Figure 7J**). Furthermore, neural
1043 silencing of dILP7 led to a mild but significant reduction in cold-evoked CT responses, whereas
1044 A02o neurons were dispensable for cold nociception (**Figure 7A, Figure 7-figure supplement**
1045 **2**).
1046 Next, we assessed whether these projection neurons were able to elicit a CT response
1047 upon neural stimulation. Optogenetic stimulation of projection neurons alone did not lead to any
1048 CT response (**Figure 2-figure supplement 2**). Simultaneous co-activation of CIII md and
1049 *R61A01*^{GAL4} or A08n neurons led to mild but statistically insignificant increases in CT responses
1050 (**Figure 7F-I, J**). Co-activation of A09e and CIII md neurons led to facilitation of CT behavior,
1051 where compared to controls there were significant increases across all behavioral metrics that we
1052 analyzed (**Figure 7F, G-I**). There were mild, statistically insignificant, reductions in larval

immobility when these projection neurons were co-activated with CIII md neurons, however, they were significant for A08n (**Figure 7-figure supplement 1B-D**). A09e, which has receives substantial inputs from CIII md neuron, was sufficient to facilitate CIII md neuron-evoked behavioral responses (**Figure 7J**).

Our neural silencing analyses suggest that A09e and *R61A01*^{GAL4} (A10j, A09o, TePn04, TePn05) neurons are required for cold-evoked responses. We hypothesized that these neurons are cold sensitive and function downstream of CIII md neurons. We predicted that these neurons would have increases in Ca^{2+} upon cold stimulation or optogenetic activation of CIII md neurons. A09e neurons present indeed significant increases in Ca^{2+} levels upon cold stimulation, as measured by cell type-specific expression of CaMPARI2 (**Figure 8A**). Optogenetic activation of CIII md neurons led to significant increases in evoked Ca^{2+} levels of A09e neurons (**Figure 8B, C**). Multiple stimulations of CIII md neurons did lead to slightly lower levels of evoked Ca^{2+} but overall Ca^{2+} response was largely similar between stimulations (**Figure 8B, C**). For *R61A01*^{GAL4} Ca^{2+} imaging experiments, we restricted our analyses to TePn04 and TePn05 neurons, which were reliably identifiable in an intact *Drosophila* larval preparation. There were significant increases in CaMPARI2 response of TePn04/05 neurons upon cold stimulation (**Figure 8D)**. Optogenetic stimulation of CIII md neurons led to strong increases in Ca^{2+} levels of TePn04/05 neurons, however, Ca^{2+} levels rapidly returned to baseline levels (**Figure 8E, F**). Repeated stimulations of CIII md neurons led to a blunted Ca^{2+} response in TePn04/05 neurons following the initial stimulation (**Figure 8E, F**). Combined, these data indicate A09e and *R61A01*^{GAL4} neurons function downstream of CIII md neurons for cold nociception (**Figure 8-figure supplement 1**), indicating that ascending neurons relay cold somatosensation to the brain.

1077

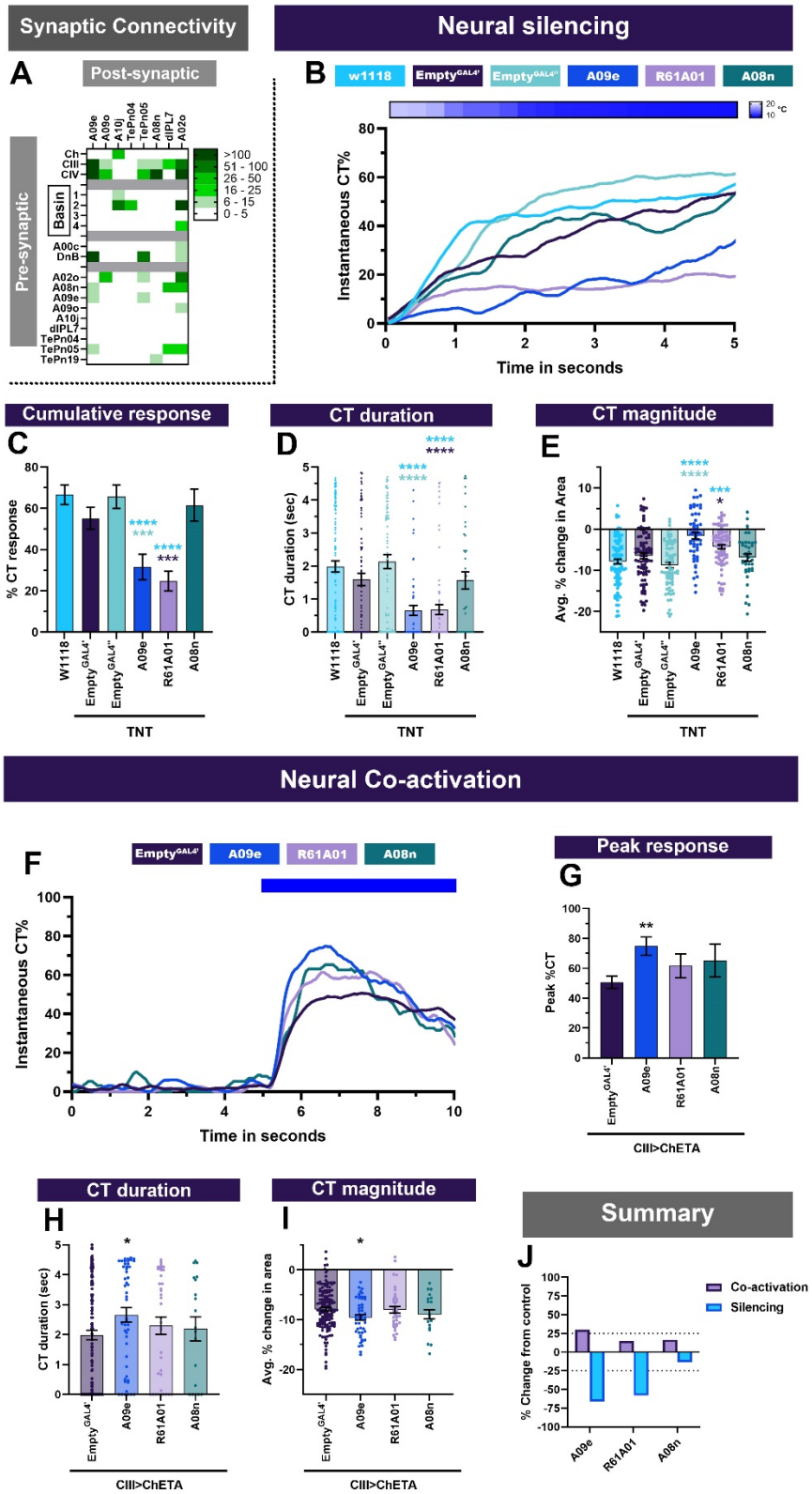
Synaptic Connectivity
Neural silencing
A
Post-synaptic
Pre-synaptic
Basin
>100
51 - 100
26 - 50
16 - 25
6 - 15
0 - 5
B
w1118
Empty^GAL4'
Empty^GAL4''
A09e
R61A01
A08n
Instantaneous CT%
Time in seconds
Cumulative response
C
% CT response
CT duration
D
CT duration (sec)
CT magnitude
E
Avg. % change in Area
TNT
Neural Co-activation
F
Instantaneous CT%
Time in seconds
Peak response
G
Peak %CT
CIII>ChETA
CT duration
H
CT duration (sec)
CT magnitude
I
Avg. % change in area
Summary
J
Co-activation
Silencing
% Change from control

1078
1079
1080 **Figure 7: Projection neurons downstream of CIII md neurons are required for cold-evoked**
1081 **responses.**
1082 (**A**) A09e, A09o, A10j, TePn04, TePn05, A08n, dILP7 and A02o primarily receive
1083 inputs from CIII md, CIV md, Basin-1, Basin-2 and DnB neurons. Heatmap plot of pre-synaptic
1084 connections to projection neurons. Synaptic connectivity data was extracted from Neurophyla
1085 LMB Cambridge. (https://neurophyla.mrc-lmb.cam.ac.uk/). (**B-E**) Cold-evoked responses of
1086 third instar *Drosophila*. Projection neurons were silenced by inhibiting neurotransmitter release
1087 via cell type specific expression of tetanus toxin (TNT), where A09e ($SS00878^{splitGAL4}$),
1088 $R61A01^{GAL4}$ (labels A09o, A10j, TePn04, and TePn05) and A08n ($R82E12^{GAL4}$). (**B**)
1089 Instantaneous %CT over time. The heatmap on top represents change in temperature over time.
1090 (**C**) Cumulative %CT response for a duration of 5 seconds. (**D**) CT duration in seconds. (**E**) CT
1091 magnitude as average percent change in area for the duration of stimulus. Controls include w^{1118},
1092 $Empty^{GAL4'}$ (*w;;attP2)* or $Empty^{GAL4''}$>*TNT* (*w;attP40;attP2)*. Significant differences were
1093 compared to each *GAL4's* respective controls dependent on insertion sites. Significant stars:
1094 turquoise stars represent comparison to w^{1118}, purple stars represent comparison to
1095 $Empty^{GAL4'}$>*TNT* and sea green stars represent comparison to $Empty^{GAL4''}$>*TNT*. For each
1096 genotype average n=72. (**F-I**) Neural co-activation of projection neurons and CIII md neurons.
1097 Here each condition represents expression of ChETA in CIII md neurons plus projection
1098 neurons. (**F**) Instantaneous %CT over time. Blue bar represents optogenetic neural activation.
1099 (**G**) Peak %CT response during optogenetic stimulation. (**H**) CT duration in seconds during
1100 optogenetic stimulation. (**I**) CT magnitude as average percent change in area for the duration of
1101 stimulus. $Empty^{GAL4'}$ n=143 and experimental condition average n =35. Significant purple stars
1102 represent comparison to *CIII md* + $Empty^{GAL4'}$>*ChETA*. (**J**) Overall percent change from control
1103 for either neural silencing or neural co-activation. The metrics for neural silencing include
1104 cumulative %CT, CT magnitude, and CT duration. The following metrics were used to calculate
1105 percent for neural co-activation: cumulative %CT, peak %CT, CT duration and magnitude.
1106 Significant differences indicated via asterisks, where *p<0.05, **p<0.01, and ***p<0.001.
1107

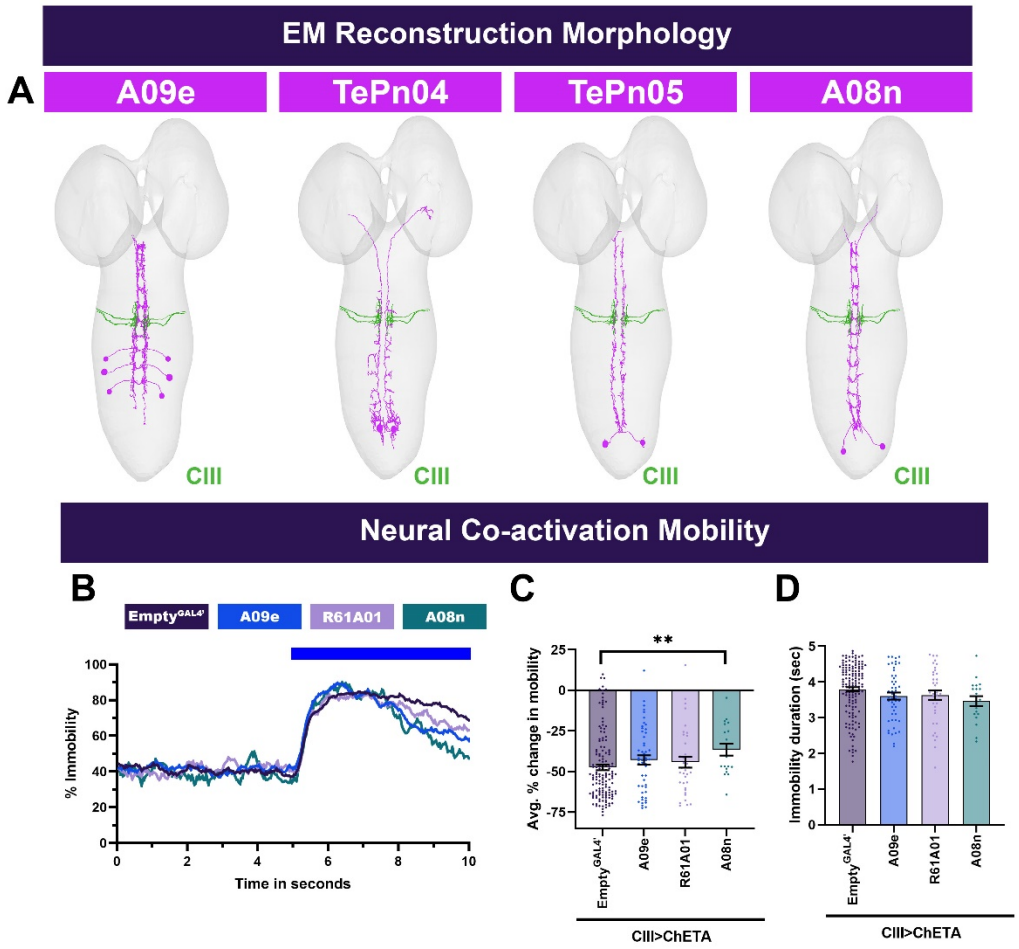

Figure 7-figure supplement 1: Neural reconstructions and larval mobility for projection neurons.

(**A**) Individual projection neuron subtypes (magenta) and CIII md neuron axons (blue). Neural reconstruction data was extracted from Neurophyla LMB Cambridge. (https://neurophyla.mrc-lmb.cam.ac.uk/). (**B-D**) *Drosophila* larval mobility observed with projection neurons plus CIII md neuron optogenetic coactivation. (**B**) Instantaneous percent immobility. Blue bar represents optogenetic neural activation. (**C**) Average percent change in mobility for each genotype, where greater percent immobility results in larger changes in average mobility. (**D**) Immobility duration in seconds during stimulation. Significant stars represent $p<0.05$, where stars represent comparison to *CIII md + Empty$^{GAL4'}$>ChETA*. *Empty$^{GAL4'}$* n=143 and experimental condition average n =35. Significant differences indicated via asterisks, where **$p<0.01$.

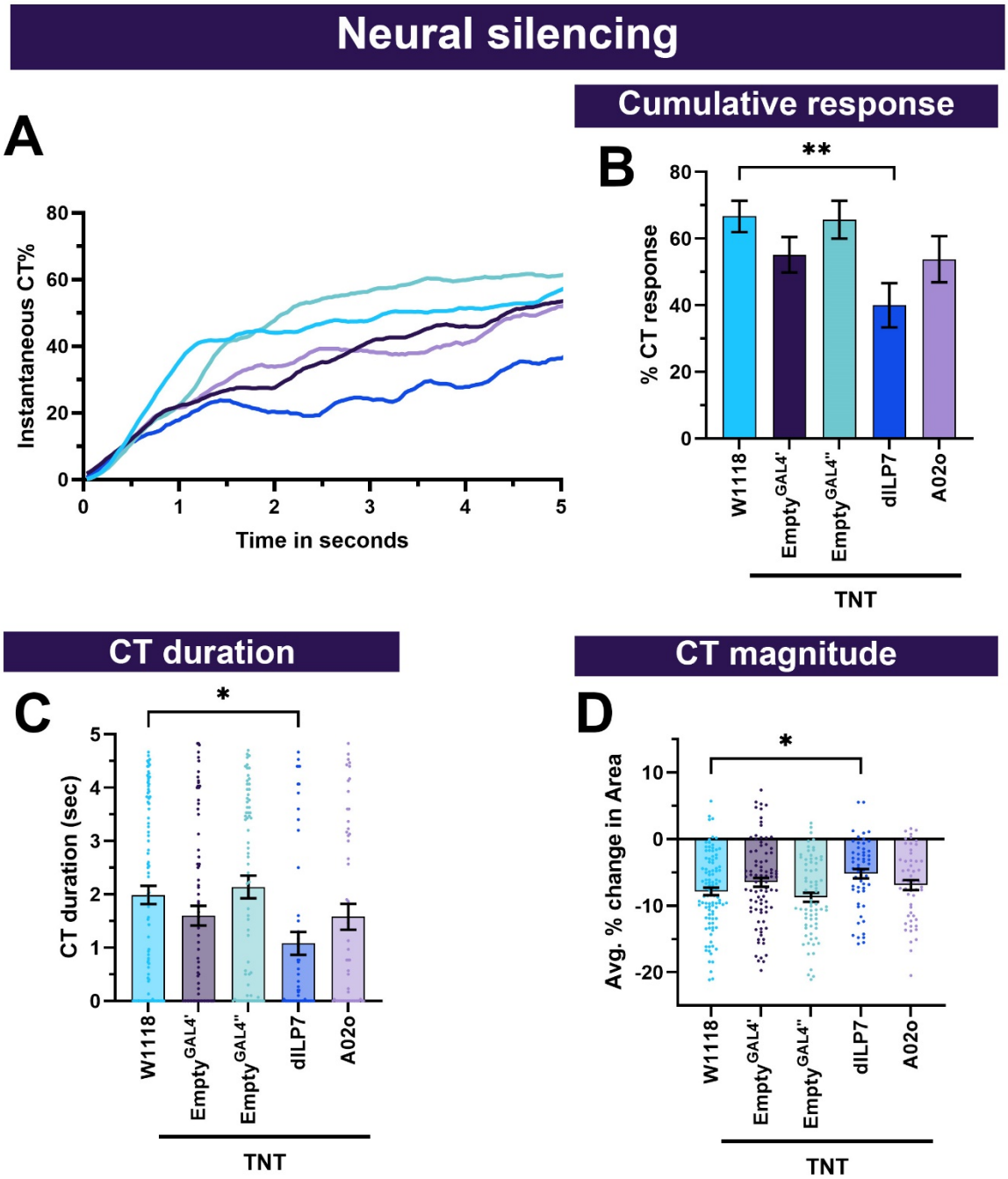

Figure 7-figure supplement 2: dLIP7 and A02o neuronal roles in cold nociception. (**A-D**) Cold-evoked responses of third instar *Drosophila*. Projection neurons were silenced by inhibiting neurotransmitter release via cell type specific expression of tetanus toxin (TNT) using driver lines for dILP7 (ILP7^{GAL4}) and A02o (MB120b^{splitGAL4}). (**B**) Instantaneous %CT over time. The heatmap on top represents change in temperature over time. (**C**) Cumulative %CT response for a duration of 5 seconds. (**D**) CT duration in seconds. (**E**) CT magnitude as average percent

change in area for the duration of stimulus. Controls include w^{1118}, $Empty^{GAL4'}$ (*w;;attP2)* or $Empty^{GAL4''}$*>TNT* (*w;attP40;attP2)*. Significant differences were compared to each *GAL4's* respective controls dependent on insertion sites. For each genotype average n=73. Significant differences indicated via asterisks, where *p<0.05 and **p<0.01.

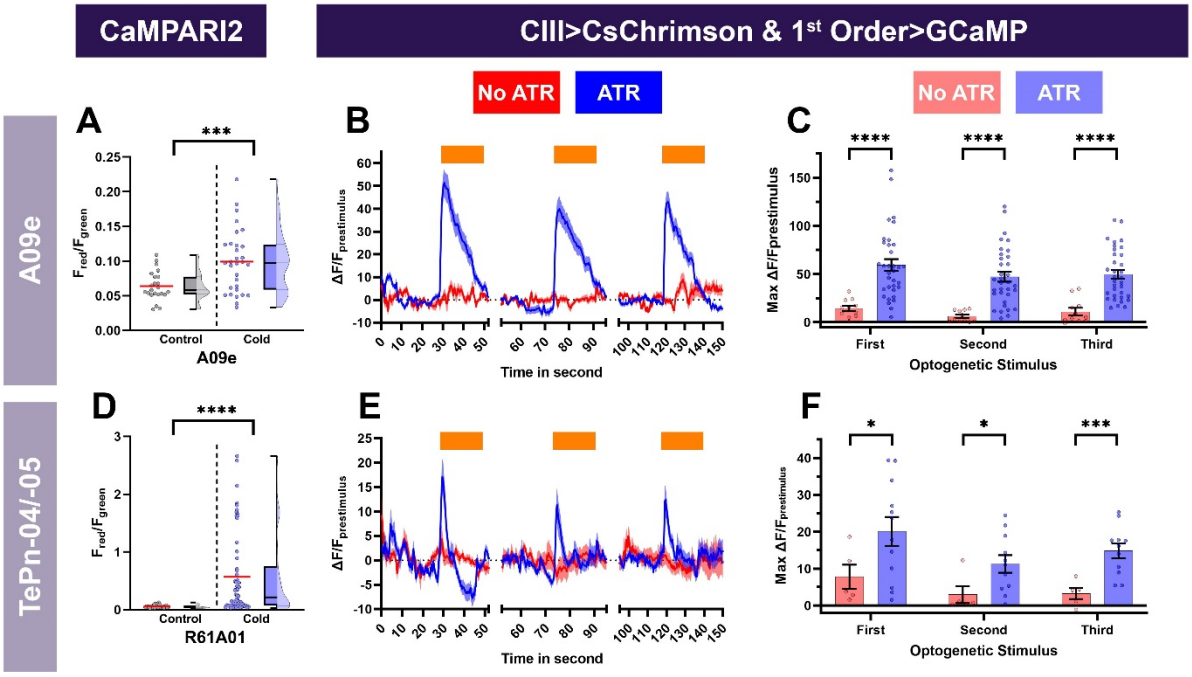

Figure 8: Cold- and CIII- evoked calcium responses of projection neurons. Neural responses of A09e ($SS00878^{GAL4}$) (**A-C**) and terminally located TePns (-04, -05) were analyzed using $R61A01^{GAL4}$(**D-F**). (**A, D**) Ca^{2+} responses of projection neurons upon cold exposure vs. controls (room temperature). Cold-evoked neural responses (CaMPARI2) of projection neuron cell bodies were analyzed for (**A**) A09e (n=27) and (**D**) TePns04, & TePn05 (n=42). CaMPARI2 fluorescence ratio is reported as F_{red}/F_{green}. We report the data as individual datapoints, where the red line represents mean, and hybrid plots (boxplot & violin) for visualizing the distribution and quartiles of data. Significant stars represent p<0.05, where comparisons were made to their respective no stimulus controls. (**B-C, E-F**) To assess, if A09e or TePns functions downstream of CIII md neurons, we optogenetically activated CIII md neurons ($83B04^{lexA}$*>CsChrimson*) and visualized changes in evoked Ca^{2+} using projection neuron specific *GAL4>GCaMP6m*. Control: No ATR supplemented diet, which is required for optogenetic stimulation in *Drosophila*. Orange bars indicate optogenetic stimulation. (**B, E**) Changes in GCaMP reported as $\Delta F/F_{prestimulus}$, where prestimulus refers to 15 seconds prior to optogenetic stimulation. (**C, F**) Maximum neuronal responses ($\Delta F/F_{prestimulus}$) upon optogenetic

stimulation. A09e average n=22. TePns average n=8. Significant differences indicated via asterisks, where *p<0.05, ***p<0.001, and ****p<0.0001.

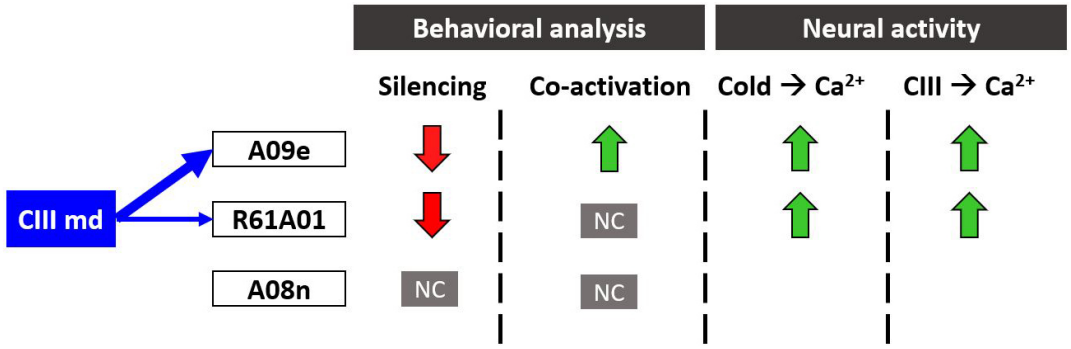

Figure 8-figure supplement 1: Summary of behavioral and functional roles of projection neurons in cold nociception.
Blue arrows indicate strength of synaptic connectivity between the CIII md neurons and second order neurons. In the behavioral analysis column, the arrow direction indicates reduction or enhancement of CT response and shading indicates magnitude of change from control. In neural activity column: NC denotes no significant change in Ca^{2+} response, the arrow direction indicates reduction or enhancement in evoked Ca^{2+} response and shading indicates magnitude of change from control. Empty spaces indicate experimental analyses were not performed.

Comparative analyses of cold sensitive neurons

Thus far, data were presented in logical groups based on their previously known cell-types and functions, however, these neurons function in an interconnected network and behavioral and functional imaging data must be assessed collectively to study circuit function. As discussed in previous sections, of all the cell types we tested only optogenetic activation of CIII md neurons alone is sufficient to elicit CT responses (**Figure 2-figure supplement 2**). Neural co-activation of CIII md neurons plus additional cell types resulted in marked increases in CT responses compared to only CIII md neuron activation (**Figure 9A**). Neural silencing of cell types downstream of CIII md neurons led to significant reductions in cold-evoked CT (**Figure 9B**). To understand how these behavioral phenotypes are interrelated, we performed t-distributed stochastic neighbor embedding (t-SNE) analysis on both neural silencing and co-activation behavioral datasets. We identified five different clusters that exhibit varying impacts on behavioral phenotypes upon either neural co-activation or silencing (**Figure 9C, D**). The first group clusters together with the control genotype and includes CIV, A05q, Goro, and A08n neurons. This group on average had less than 25% change in behavioral phenotypes in either neural co-activation or silencing experiments (**Figure 9C, D**). Basin-1 and DnB neurons clustered together, where on average they had 49% enhancement of CT response upon neural co-activation and 45% reduction in cold-evoked CT response upon neural silencing (**Figure 9C, D**).

1180 *R61A01* and CIII md neurons formed a cluster, where neural silencing resulted in nearly 60%
1181 reduction cold-evoked behavior and 20% enhancement of CIII md neuron-evoked behaviors
1182 upon neural co-activation (**Figure 9C, D**). A group of neurons including Chair-1, Basin-4 and
1183 Ch were required for cold-evoked behavioral responses, however, these neurons did not facilitate
1184 CIII evoked CT responses (**Figure 9C, D**). In the last group, neural silencing of all Basins,
1185 Basin-2, mCSI, A00c or A09e led to an overall 69% reduction in cold-evoked behaviors and
1186 34% enhancement in CIII evoked CT response (**Figure 9C, D**). Additionally, we assessed how
1187 CIII md neuron synaptic connectivity to post-synaptic neurons could inform whether CIII md
1188 post-synaptic neurons are required for cold nociception (**Figure 9E**). Generally, neural silencing
1189 of highly connected CIII md post-synaptic neurons exhibited greater requirement in cold
1190 nociception, however, there are a few notable exceptions (A02f & A02o), where greater
1191 connectivity did not lead to significant impairment in cold sensitivity (**Figure 9E**).
1192 Analyses of *Drosophila* larval behavioral phenotypes revealed distinct roles for
1193 downstream neurons in cold nociceptive circuitry. Mapping synaptic connectivity of a particular
1194 circuit is only the first step in understanding how individual behaviors arise. Here, we draw
1195 attention to select CIII md neuron first-order neurons (Basins (-2 & -4), DnB, TePns and A09e)
1196 that showed robust requirements for cold nociceptive behaviors and had functional connectivity
1197 to CIII md neurons (**Figure 9F**). TePns synapse onto Basin-4 and form reciprocal connections to
1198 Basin-2, DnB, and A09e (**Figure 9F)**. DnB further synapses onto Basin-4 and A09e. Within this
1199 circuit motif one might predict that A09e neurons function as the master integrators, where they
1200 might be computing synaptic information from various sources (**Figure 9F)**. Consistent with EM
1201 connectivity, A09e neurons have the highest CIII md neuron-evoked Ca^{2+} responses of the tested
1202 cell types (**Figure 9G, H)**. Compared to Basin-4 neurons, Basin-2 neurons receive greater
1203 synaptic input from CIII md neurons (**Figure 9F**). However, CIII md neuron activation leads to
1204 nearly twice as much Ca^{2+} response in Basin-4 neurons than Basin-2 (**Figure 9G, H)**. DnB
1205 neurons receive the second highest synaptic input from CIII md neuron and have the second
1206 highest CIII md neuron-evoked Ca^{2+} response (**Figure 9G, H)**. TePns receive significantly lower
1207 synaptic input compared to Basin-2 neurons, however, they both exhibit similar levels of CIII md
1208 neuron-evoked Ca^{2+} response (**Figure 9G, H)**. Comparative analyses reveal that synaptic
1209 connectivity is informative about functional neural activity, however, additional molecular and
1210 functional studies are required to fully understand roles of these neurons in cold nociception.
1211 Collectively, our findings on neural substrates of cold nociception indicate that second order
1212 multisensory integration by Basin neurons, select pre-motor neurons and projection neurons are
1213 preferentially activated in a stimulus specific manner to elicit appropriate behavioral responses.
1214
1215
1216
1217
1218

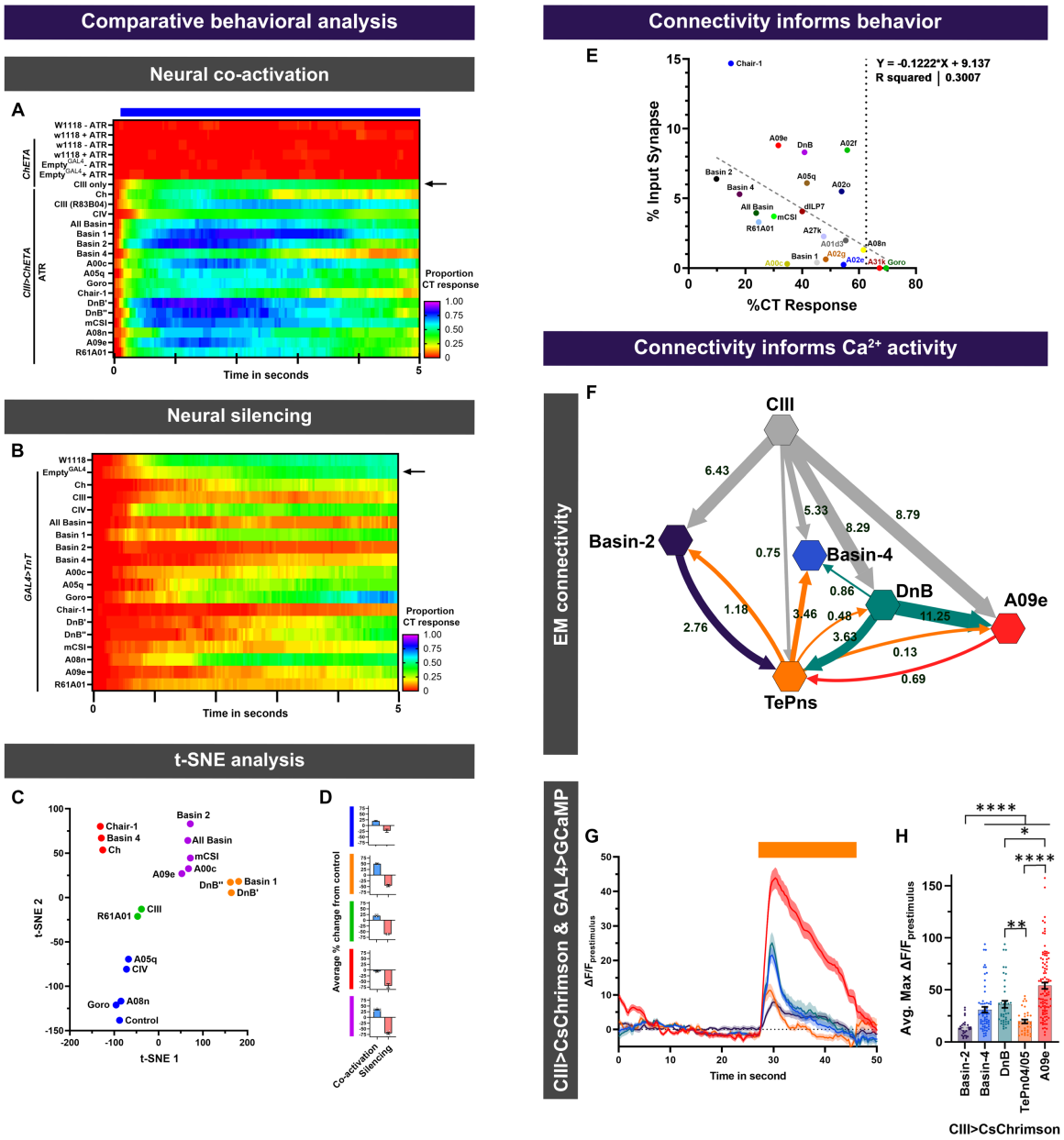

Figure 9: Dimensional reduction analysis of *Drosophila* larval behavioral responses and synaptic connectivity informs functional connectivity assessed via Ca^{2+} imaging. (**A-B**) Instantaneous CT proportions for all genotypes in this study. (**A**) Neural co-activation experiments, where CIII plus additional neuronal types were simultaneously optogenetically activated. Controls for optogenetic experiments were tested with or without ATR supplement and include the following conditions: background strain (*w1118*), background strain crossed to *UAS-ChETA*, and *Empty*^{GAL4} crossed to *UAS-ChETA*. Blue bar represents optogenetic stimulation. (**B**) Neurotransmitter release inhibition of individual neuronal types using cell-type specific expression of TnT. (**C-D**) t-distributed stochastic neighbor embedding (t-SNE) analysis of all neuronal subtypes role in both cold nociception (neural silencing data) and CIII md

1229 neuron-evoked CT facilitation (co-activation data). (**C**) 2D plot of t-SNE analysis, where post-
1230 hoc clustering analysis based on "Euclidian complete" method revealed 5 unique groups. The
1231 following percent change from control (*Empty*^{GAL4}) data were included in the analysis: For neural
1232 co-activation (peak % CT response, cumulative % CT response, average % change in area, and
1233 CT duration) and for neural silencing (cumulative % CT response, average % change in area, and
1234 CT duration). (**D**) Average percent change from control for each cluster in '**C**' across all neural
1235 co-activation or neural silencing metrics. (**E**) Synaptic connectivity informs cold-evoked
1236 behavioral responses. Here, for each neuron-type, the percent synaptic input from CIII md
1237 neurons is plotted against cold-evoked CT % upon neuron silencing. There is a negative
1238 correlation between greater synaptic connectivity and lower % CT response. (**F-H**) Analyses of
1239 connectivity upon select circuit components and comparative CIII md neuron-evoked calcium
1240 responses in post-synaptic neurons. (**F**) Proportion of synaptic inputs amongst neurons are
1241 plotted. A09e neurons integrate responses from multiple pathways originating from CIII md
1242 neurons. Network map created using Cytoscape (Shannon et al., 2003). (**G-H**) CIII md neuron-
1243 evoked calcium responses in post-synaptic neurons. (**G**) $\Delta F/F_{baseline}$ over time. (**H**) Average max
1244 $\Delta F/F_{baseline}$. Averages ± SEM of all trials are plotted. Significant differences indicated via
1245 asterisks, where *p<0.05, **p<0.001, and ****p<0.0001.
1246
1247
1248 **Neuromuscular basis of cold-evoked CT in *Drosophila* larval**
1249
1250 Sensory perception is the first node for interfacing with the external environment, which
1251 is processed through various pathways in the brain eventually leading to motor commands that
1252 generate stimulus specific behavioral responses. Thus far, we have implicated CIII md neurons
1253 as the primary cold sensitive neurons, which transduce thermal cues to select multisensory
1254 integration neurons, premotor neurons and ascending neurons. However, it remains unexplored
1255 how the sensory and central processing of cold leads to CT responses. To this end, assessing CIII
1256 md neuron's premotor neuron network revealed that collectively CIII md premotor neurons have
1257 connectivity to 5 of the 6 major muscle groups in a *Drosophila* larva hemi-segment (**Figure**
1258 **10A)**. Next, we assessed how individual *Drosophila* larva muscular segments respond to noxious
1259 cold. Analysis of muscle localized Ca^{2+} responses revealed that all larval segments have cold-
1260 evoked increases in Ca^{2+} (**Figure 10B-D)**. Interestingly, the strongest cold-evoked response is
1261 present in abdominal segments (A2-A5), whereas anterior (T1-A1) and posterior (A6-A8)
1262 segments have marginally smaller cold-evoked Ca^{2+} responses (**Figure 10B,C)**. Similar to cold-
1263 evoked CT behavior, where the head and tail contract towards the center of the animal, muscle
1264 segments in anterior and posterior reach peak activity sooner than the central segments by
1265 average of 4 seconds (**Figure 10B'**). Evaluating individual larval cold-evoked Ca^{2+} levels
1266 revealed segmental responses that can be attributed to previously identified cold-evoked
1267 behavioral responses (*i.e.* CT and head and/or tail raises) (**Figure 10D)** (Turner et al., 2016;
1268 Turner et al., 2018).

Furthermore, we assessed whether impaired circuit function would lead to reduced cold-evoked muscle responses. Firstly, while maintaining sensory perception, silencing motor neuron activity using GtACR1 resulted in significant reductions in cold-evoked Ca^{2+} levels compared to controls (**Figure 10-figure supplement 1A-E**). Secondly, application of ethyl ether also resulted in significant reductions in cold-evoked Ca^{2+} activity in postsynaptic densities (PSDs) in larval muscles (**Figure 10-figure supplement 1F-H**).

To achieve greater granularity of how muscles respond to noxious cold, we quantitatively assessed how individual muscles respond to changes in temperature. Based on electrical stimulations of abdominal motor nerves, larval body wall muscles have equivalent force generation capabilities for dorsal, lateral or ventral muscles (Ormerod et al., 2022). Dorsal longitudinal and oblique (DL and DO) muscles respond acutely and maintain high cold-evoked Ca^{2+} levels throughout the stimulus period (**Figure 10E-I)**. Meanwhile, lateral transverse (LT) muscles exhibit a gradually increasing cold-evoked Ca^{2+} levels reaching a peak response at the end of the cold stimulus (**Figure 10E-I)**. Lastly, ventral lateral and oblique (VL and VO) muscles respond most robustly to the onset of cold stimulation which gradually declines over the course of the stimulation, in contrast to DL and DO muscles, which maintain their levels of Ca^{2+} activation throughout the stimulus (**Figure 10E-I)**. Both dorsal (DO & DL) and ventral (VO & VL) muscles reach peak response ~10 seconds before lateral muscles (**Figure 10I)**. Thus, *Drosophila* larvae exhibit stimulus specific muscle activation patterns that are consistent with cold-evoked behavioral responses arising from sensory processing of temperature changes.

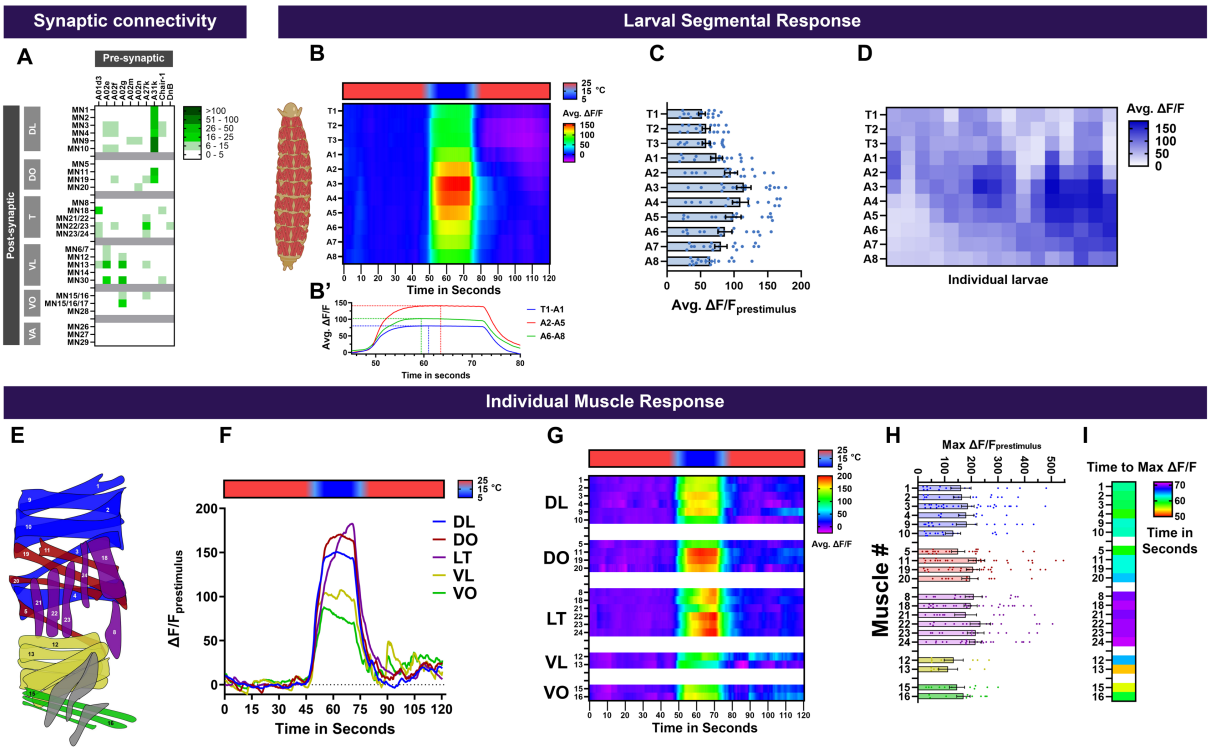

1291

1292 **Figure 10: Muscular basis of *Drosophila* larval cold-evoked CT at segmental and individual**
1293 **muscle level.**
1294 (**A**) Motor neurons (MN) receiving synaptic input from premotor neurons that are downstream of
1295 CIII md neurons. Heatmap plot of pre-synaptic connections to motor neurons. Synaptic
1296 connectivity data was extracted from Neurophyla LMB Cambridge. (https://neurophyla.mrc-
1297 lmb.cam.ac.uk/). (**B-D**) Analysis of cold-evoked Ca^{2+} responses of muscles in individual
1298 segments measured by expressing *jRCaMP1a* using *Mef2*^{GAL4}. Larval graphic created using
1299 BioRender.com. (**B**) Average $\Delta F/F_{prestimulus}$ of individual larval segments across time. (B')
1300 Average cold-evoked Ca^{2+} response in the anterior (T1-A1), central (A2-A5), posterior (A6-A8)
1301 segments. Dotted lines mark max $\Delta F/F_{prestimulus}$ and time to max $\Delta F/F_{prestimulus.}$ (**C**) Average
1302 $\Delta F/F_{prestimulus}$ of individual larval segments during cold exposure. (**D**) Individual larval average
1303 $\Delta F/F_{prestimulus}$ for each larval segments during cold exposure. Individual larval responses exhibit a
1304 variety of cold-evoked increases in Ca^{2+}, similar to the range of observed micro-behaviors that
1305 lead to CT. Average n= 16. (**E-H**) Analysis of cold-evoked Ca^{2+} of individual muscle cells in
1306 *Drosophila* larvae as measured by expressing *jRCaMP1a* using *Mef2*^{GAL4} and laser confocal
1307 microscopy. (**E**) Schematic of individual muscle cells in a larval hemi-segment from an external
1308 view. Muscles that are numerically labeled were analyzed; many ventrally located muscles could
1309 not reliably be analyzed. (**F**) Average $\Delta F/F_{prestimulus}$ of individual spatial muscle groups as
1310 defined in (Zarin et al., 2019). All muscle groups show cold-evoked Ca^{2+} increase, however, the
1311 dynamics of each muscle group are varied. Dorsal longitudinal (DL) and Dorsal oblique (DO)
1312 both have strong cold-evoked Ca^{2+} response that is largely stable throughout the stimulus period.
1313 Both DL and DO muscles have a peak average $\Delta F/ F_{prestimulus}$ about halfway through the
1314 stimulus. Lateral Transverse (LT) muscles show an ever increasing cold-evoked Ca^{2+} response
1315 that peaks near the end of the stimulus. Lastly, Ventral Longitudinal (VL) and Ventral Oblique
1316 (VO) have cold-evoked Ca^{2+} increase that is highest at the onset of stimulus and decays
1317 gradually throughout the stimulus period. (**G**) Cold-evoked average $\Delta F/F_{prestimulus}$ of individual
1318 muscles across time. (**H**) Cold-evoked average max $\Delta F/F_{prestimulus}$ of individual muscles across
1319 time. Average n= 16. (**I**) Heatmap representation of average time max $\Delta F/F_{prestimulus}$ for
1320 individual muscles.

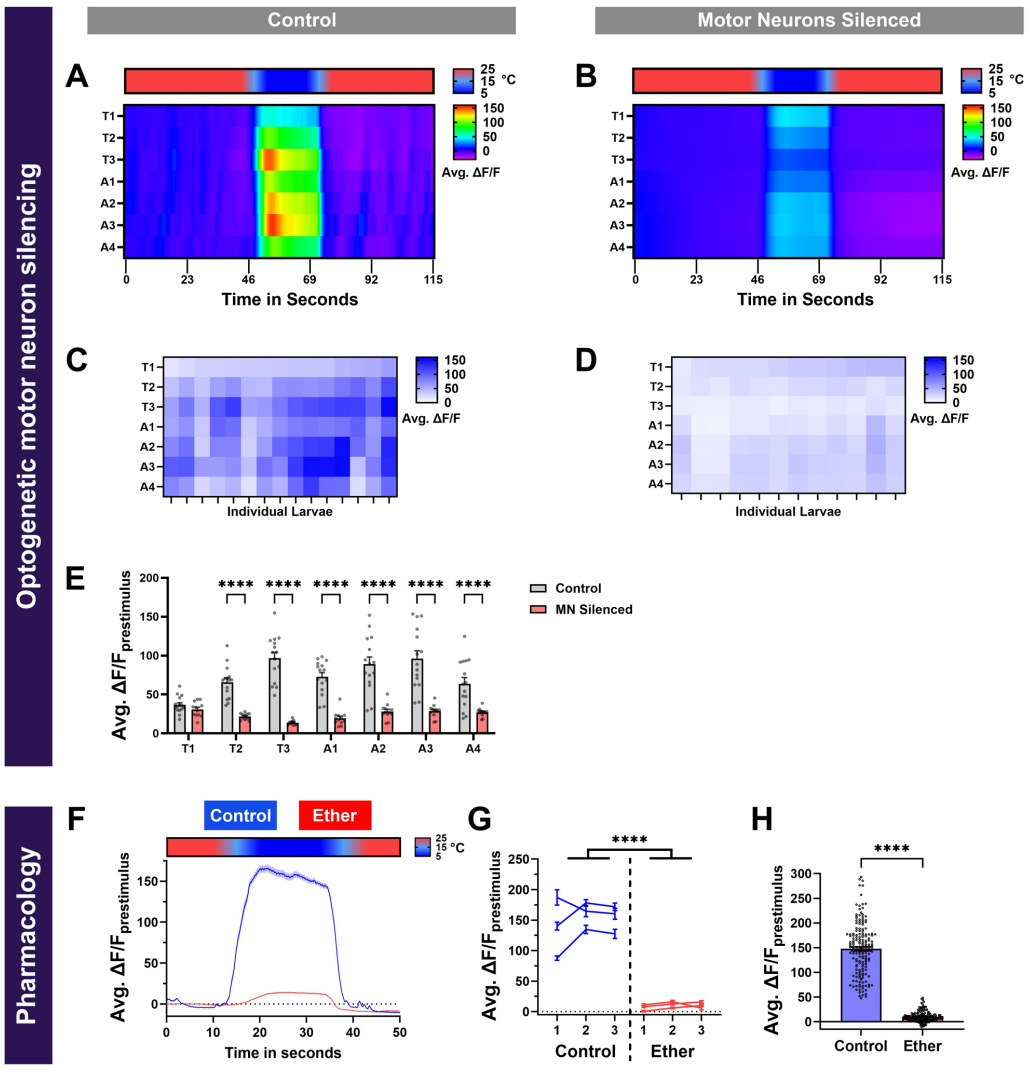

Figure 10 -figure supplement 1: Motor neuron silencing or pharmacological anesthesia results in significant reductions in cold-evoked muscle activity

(**A-E**) Cold-evoked muscle Ca^{2+} responses with functional motor neurons and optogenetically silenced motor neurons. (**A-B**) Heatmap of average $\Delta F/F_{prestimulus}$ GCaMP6f responses in segments T1-A4. Segments A5-A8 were not analyzed due to high autofluorescence of the digestive tract. (**C-D**) Heatmap of average $\Delta F/F_{prestimulus}$ GCaMP6f responses individual larvae and segments during the stimulus period. When motor neurons are silenced, nearly all analyzed segments have the similar cold-evoked responses compared to controls, where we certain segments reaching very high average $\Delta F/F_{prestimulus.}$ (**E**) Average muscle average $\Delta F/F_{prestimulus}$ GCaMP6f response comparison for each segment between control and silenced motor neurons. Average n= 13 larvae. Genotype: 44H10-GCaMP6f, D42>GtACR1 ± ATR.

(**F-H**) Muscle postsynaptic density (PSD) Ca^{2+} responses were assessed using SynapGCaMP6f (MHC-CD8-GCaMP6f-Sh) in *Drosophila* larval segment T3/A1. In controls, there is a robust cold-evoked increase in Ca^{2+} levels, however, upon ethyl ether application, there is a significant

reduction in evoked Ca^{2+} levels. (**F**) Average $\Delta F/F_{prestimulus}$ over time for all stimulations. (**G**) Average $\Delta F/F_{prestimulus}$ during stimulus of all quantified PSDs for each animal across three stimulations. (**H**) Average $\Delta F/F_{prestimulus}$ of individual PSDs across three stimulations. Average n=3 larvae with average PSDs n=171.

Discussion

Environmental stimuli are detected by peripheral sensory neurons, which transduce relevant cues to downstream central circuitry responsible for processing multisensory input and generating stimulus-relevant behavioral responses. The study of the diverse molecular and cellular mechanisms involved in sensory discrimination have yielded key insights into how animals interact with their environment (Arnadóttir et al., 2011; Bandell & Patapoutian, 2009; Chrispin et al., 2013; Corfas & Vosshall, 2015; Coste et al., 2010; Derby et al., 2016; Dietrich et al., 2022; Fowler & Montell, 2013; Freeman & Dahanukar, 2015; Himmel et al., 2017; Leung & Montell, 2017; Montell, 2021; Wu et al., 2018; Xiao & Xu, 2021). However, how animals distinguish between innocuous and noxious stimuli at molecular, cellular and circuit level remains an important question in modern neuroscience (Bushnell et al., 1985; Dannhauser et al., 2020; Himmel et al., 2023; Imambocus et al., 2022; Moehring et al., 2018; Patel et al., 2022; Turner et al., 2016; Ward et al., 1996).

Here, we assessed the downstream circuitry of a multimodal sensory (CIII md) neuron that detects both innocuous mechanical and noxious cold temperatures. In CIII md neurons, detection of innocuous cues occurs via low threshold activation and noxious cues are detected via high threshold activation leading to stimulus-relevant behaviors (Turner et al., 2016). Transduction of nociceptive cold stimulus is predominantly mediated by multimodal Ch and CIII md neurons. However, nociceptive peripheral sensory neurons, CIII md and CIV md neurons, function through shared downstream neural circuitry. We describe the behavioral and functional requirements of multisensory integration (Basins) neurons, premotor (DnB and mCSI) neurons and projection (A09e and TePns) neurons in noxious cold-evoked behavioral responses. We identified circuit components that play a role in amplifying noxious cues and differentiating between opposing noxious (heat versus cold) stimuli-evoked behaviors at various levels of sensory processing. Finally, we characterize how stimulus-evoked muscle contractions lead to cold nociceptive behavioral response. Our findings provide key insights into how environmental cues are processed by multiplexed networks for multisensory integration and decision making.

<u>Basin-1 neurons function across sensory modalities as gain modulators for noxious stimuli-evoked escape responses.</u>

Accurately responding to potentially harmful stimuli by appropriately executing energetically expensive escape behaviors is critical for animal survival. Incorrectly performing escape responses in absence of dangerous stimuli can have long-term detrimental consequences.

Therefore, the need for neural mechanisms responsible for integrating various noxious and innocuous sensory stimuli for accurately executing stimulus-appropriate escape responses. Here, we focus on the role of Basin neurons, known to mediate various escape responses (Jovanic et al., 2016; Masson et al., 2020; Ohyama et al., 2015).

EM connectome analyses revealed that somatosensory (Ch, CIII md and CIV md) neurons all synapse onto multisensory integrating Basin neurons, and that amongst the Basins subtypes, Basin-1 neurons are presynaptic to Basin-2,-3 and -4 neurons (Masson et al., 2020; Ohyama et al., 2015). On the basis of the known connectome, we analyzed the function of Basin neurons in cold-evoked escape behaviors. Our findings indicate that optogenetic activation of Basin-1 is not sufficient to evoke noxious cold-evoked behavioral response (**Figure 2 – Supplement 2**) and it was known that thermogenetic activation of Basin-1 is also not sufficient for evoked rolling escape (Ohyama et al., 2015). Therefore, Basin-1 neuron activity alone is not sufficient to elicit a noxious stimuli-evoked behavioral response. However, due to intricate connectivity amongst the Basins, the total integrated output of multiple Basin neurons may lead to threshold activation of noxious stimulus-evoked escape responses. And indeed, thermogenetic co-activation assays found that Basin-1 neural activity could facilitate a Basin-4 -mediated rolling response (Ohyama et al., 2015), and also the activation of Basin-1 neurons leads to the activation of Basin-2 neurons through lateral disinhibition (Jovanic et al., 2016). Here, we found that co-activation of Basin-1 plus CIII md neurons led to strong-evoked CT responses (**Figure 2**). Taken together, these studies concluded that Basin-1 facilitates the activation of other Basin neurons, and our results also provide additional support for the role of Basin-1 neurons in fine-tuning behavioral outcomes and enhancing cumulative output of multisensory integration Basin neurons leading stimulus specific escape responses.

Multisensory integration neurons drive behavioral selection downstream of sensory neurons.

In order to evaluate the functional and behavioral roles of neurons within a circuit, a comprehensive analysis of both upstream and downstream synaptic connectivity is necessary. Basin-2 and -4 neurons integrate different amounts of synaptic input from somatosensory neurons, other Basin neurons, feedforward/back inhibitory neurons, and projection neurons. Basin-4 neurons receive greater excitatory synaptic input compared to Basin-2 neurons, which have greater connectivity with local inhibitory neurons (Jovanic et al., 2016; Masson et al., 2020; Ohyama et al., 2015). Larger inhibitory connectivity of Basin-2 neurons likely arises from much broader downstream connectivity including several projection/descending neurons (A00c, A02o, A05q, A10j, TePn04), premotor neurons (A02m, A02n, Chair-1), descending feedback inhibitory neuron (SeIN128), local feedback neurons (Handle-a/-b), whereas Basin-4 downstream connectivity is restricted to limited set of neurons (A00c, A02o, Basin-3, Chair-1) (Zhu et al., 2024). These synaptic level differences in multisensory integration neurons underlie noxious stimuli-specific evoked responses and suggest that CIII md neuron mediated responses primarily

1416 function through Basin-2 neurons and CIV md neuron mediated environmental cues are
1417 processed via Basin-4 neurons.
1418
1419 Chemical nociception in *Drosophila* larvae primarily functions via CIV md neurons.
1420 Among the md neurons, CIII md neurons are the least sensitive to noxious chemical stimulus
1421 (Lopez-Bellido et al., 2019). Analyses of Basin neuron requirement in chemical nociception
1422 revealed that all Basins are necessary for chemical-evoked rolling, where comparative analyses
1423 of Basin subtypes revealed that chemical nociception is primarily mediated through Basin-4 with
1424 weaker behavioral phenotypes of Basin-1 or -2 (Lopez-Bellido et al., 2019). Our work shows
1425 that inhibition of neurotransmission in Basin-2 or Basin-4 neurons leads to significant reductions
1426 in cold nociceptive responses, where across the analyzed behavioral metrics Basin-2 had stronger
1427 deficits in cold-evoked responses (**Figure 2**). Furthermore, neural co-activation analyses
1428 revealed that Basin-2 plus CIII md led to enhanced CT response, whereas Basin-4 plus CIII md
1429 co-activation did not facilitate but rather suppressed the CT response (**Figure 2**). Basin-2 neural
1430 activity likely has cascading effects on functions of downstream neurons (i.e. TePns, A02m/n,
1431 Chair-1, & A00c), which we also found to be required for cold nociception. Behavioral
1432 assessment of multisensory integration neurons supports the notion that CIII md neuron sensory
1433 input is processed primarily by Basin-2 and CIV md neuron sensory cues are processed via
1434 Basin-4 neurons.
1435
1436 Despite the accumulating evidence that cold-evoked responses are primarily mediated by
1437 Basin-2, our Ca^{2+} analyses revealed that compared to Basin-2, Basin-4 neurons have much
1438 greater cold- or CIII md neuron- evoked Ca^{2+} responses. There are a few possible explanations
1439 for greater Basin-4 activity levels. Firstly, greater Basin-4 Ca^{+2} activity could be due to greater
1440 synaptic input from projection neurons (TePn04/05) and premotor neurons (DnB), which are
1441 both required for cold nociception and exhibit cold- or CIII md neuron-evoked Ca^{2+} responses
1442 (**Figure 7, Figure 8 – Supplement 1**) (Masson et al., 2020). Secondly, reduced Basin-2 Ca^{2+}
1443 responses could be due to greater connectivity with feedback/feedforward inhibitory local
1444 neurons (Jovanic et al., 2016; Masson et al., 2020) or descending feedback neuron (SeIN128)
1445 (Zhu et al., 2024). Descending inhibitory, SeIN128, neuron functions in transitioning from
1446 rolling to fast crawling response in *Drosophila* larvae (Zhu et al., 2024). SeIN128 receives
1447 synaptic input from Basin-2 but not Basin-4, while providing feedback inhibition to Basins (-1, -
1448 2, -3), premotor neurons (A02m/n, Chair-1 & DnB) and projection neurons (A00c, A02o, &
1449 A05q) (Ohyama et al., 2015; Zhu et al., 2024). Thus, lower cold-/CIII md neuron-evoked Basin-
1450 2 neural activity could be due to greater feedback inhibitory input compared to Basin-4.
1451 Comparative Ca^{2+} imaging or electrophysiological analyses can further delineate the precise
1452 interplay between Basin-2 and -4 neurons in integrating sensory information across
1453 somatosensory modalities leading to distinct behavioral responses. However, to date, synaptic
1454 connectivity and behavioral analyses collectively indicate an initial sensory discrimination node
1455 amongst the Basin neurons, where downstream processing of CIII mediated sensory input is

conveyed through Basin-2 and its downstream connectivity, meanwhile CIV somatosensory information is transduced through Basin-4 neuronal pathway.

Differential roles of pre-motor neurons lead to behavioral selection.

Animal locomotive behavioral responses are implemented through neurosecretory systems and muscle contractions evoked by motor neuron activity. Motor neurons integrate a conglomerate of neural impulses from premotor neurons, leading to appropriate muscle activation patterns to implement specific behavioral responses (Bellardita & Kiehn, 2015; Berkowitz et al., 2010; Carreira-Rosario et al., 2018; Green & Soffe, 1996; Huang & Zarin, 2022; Liao & Fetcho, 2008; Talpalar et al., 2013; Zarin et al., 2019). Recent work in premotor and motor neuron connectomics has provided evidence for both labeled line and combinatorial connectivity between promotor and motor neurons that give rise to co-active motor neurons states leading to selective muscle group activation (Cooney et al., 2023; Huang & Zarin, 2022; Zarin et al., 2019). Various *Drosophila* larval premotor neuron subtypes and/or motor pools have been implicated in locomotion, nociception, and innocuous mechanosensation (Burgos et al., 2018; Cooney et al., 2023; Huang & Zarin, 2022; Kohsaka et al., 2017; Kohsaka et al., 2014; Kohsaka et al., 2019; Yoshino et al., 2017; Zarin et al., 2019). Neural reconstruction efforts in *Drosophila* larvae have revealed that somatosensory (CIII md and CIV md) neurons are not directly connected to motor neurons, but rather feed into polysynaptic pathways leading to motor neurons via premotor neurons (such as the DnB, mCSI, & Chair-1 neurons studied here) (Cooney et al., 2023; Jovanic et al., 2019; Ohyama et al., 2015; Winding et al., 2023; Yoshino et al., 2017). Premotor neurons (DnB, mCSI, and Chair-1) that receive synaptic input from CIII md neurons are required for cold-evoked responses. However, only premotor neurons previously implicated in nociceptive escape responses, DnB and mCSI, can facilitate CIII-evoked CT responses (Burgos et al., 2018; Lopez-Bellido et al., 2019; Yoshino et al., 2017). Meanwhile, Chair-1 neurons, which are required for innocuous mechanosensation (Jovanic et al., 2019), do not facilitate CIII md neuron mediated CT responses. We showed, with Ca^{2+} imaging, that Chair-1 neurons are not activated upon cold exposure. It remains unclear whether Chair-1 neuronal function is sufficient to drive specific sensory evoked behaviors or requires a combinatorial pre-motor neuronal activity for generating evoked behavioral responses. Given the data, we speculate that Chair-1 neurons likely gate innocuous-to-noxious stimulus-evoked behaviors; however, additional functional studies are required to tease out how Chair-1 neurons function in behavioral selection.

Heterogeneity in thermosensory processing reflects variety of thermal stimuli.

Animals detect changes in temperature through a variety of sensors that occupy and function in different spatiotemporal timescales. Thermosensory systems function to detect changes at the epidermal, brain and visceral levels, and these broad thermosensory inputs must

be integrated to generate appropriate behavioral responses (Nakamura, 2018). The underlying neural circuitry for thermosensation differs based on body plan and type of thermosensation. In mice, cool and warm sensory signals, which are detected by TRP channels, are transmitted to the spinal dorsal horn, where distinct cool/warm pathways relay epidermal changes in temperature to thalamocortical regions for perception and discrimination (Nakamura, 2018). In *Drosophila* larvae and adults, thermotaxis occurs through temperature detection via dorsal organ ganglion (DOG) and antennal thermoreceptors, respectively (Frank et al., 2015; Gallio et al., 2011; Hernandez-Nunez et al., 2021; Klein et al., 2015; Liu et al., 2003). Investigations of circuit bases of thermotaxis have revealed different strategies for larval and adult systems. Adult antennal thermoreceptors have distinct hot or cold sensors, which project to the proximal antennal lobe (PAL), where hot and cold information is segregated into discrete regions (Gallio et al., 2011; Macpherson et al., 2015). Thermal coding properties of thermosensory projections neurons (tPNs), whose dendrites are located in PAL, include both slow/fast adapting tPNs and broadly/narrowly tuned tPNs (Frank et al., 2017). *Drosophila* larval thermosensory DOG contains both warm- and cool- sensing cells that are connected to individual cool or warm projection neurons (Hernandez-Nunez et al., 2021). DOG thermosensory information is further integrated by integration projection neurons (iPNs), which receive inputs from both warm and cool projection neurons (Hernandez-Nunez et al., 2021). The *Drosophila* larval noxious thermosensory system has distinct hot (CIV md) or cold (CIII md) sensing neurons (Babcock et al., 2009; Tracey et al., 2003; Turner et al., 2016). Larval somatosensory thermal inputs mediated by CIII md neurons are heavily integrated by second order neurons (Basins, DnB, A09e, etc.), where population coding leads to cold-evoked behavioral response. Noxious cold stimulus is encoded downstream of CIII md neurons by ascending neurons (A09e and TePns) that allow for systems-level integration of multiple thermal inputs including those from cool/warm sensitive larval DOG neural circuits and cold/heat information from CIII/CIV md neurons, respectively. Thermal information from the larval DOG and somatosensory neurons converges onto the mushroom body, where cool or warm projection neurons downstream of DOG and feed-forward projection neurons downstream of ascending neurons (A09e) synapse onto the same mushroom body output neuron (Eichler et al., 2017; Hernandez-Nunez et al., 2021; Winding et al., 2023). Thus far, ascending pathways into the brain have been characterized for larval cold nociception, however, descending output neurons responsible for cold-evoked behaviors remains unidentified. Diversity in processing thermosensory stimuli reflects heterogeneity at molecular, cellular, and circuit levels that collectively function to maintain proper thermal homeostasis and ultimately behavioral action selection. The *Drosophila* larval thermosensory system is well-suited to dissect mechanisms underlying central nervous system integration of varying spatial and functional thermosensory information by utilizing various molecules, sensory systems, and interconnected circuits for appropriate behavioral responses.

<u>Muscle activity patterns underpin behavioral responses</u>

1536 Animals interact with the external environment by detecting external cues via sensory
1537 systems that are transduced to CNS, where motor commands are generated to elicit stimulus
1538 relevant muscle activity patterns leading to behavioral responses. *Drosophila* larval body wall
1539 muscle have unique behavior relevant muscle activity patterns for locomotion and nociceptive
1540 responses (rolling and CT) (Cooney et al., 2023; Heckscher et al., 2012; Liu et al., 2023; Zarin et
1541 al., 2019, This work). In forward locomotion, posterior segments contract before anterior
1542 segments generating a forward contraction wave, where the longitudinal (dorsal & ventral)
1543 muscles contract first during the wave phase and lateral muscles contract during the interwave
1544 interval (Heckscher et al., 2012; Liu et al., 2023; Zarin et al., 2019). Exposure to nociceptive
1545 heat, mechanical or chemical cues larvae execute a corkscrew rolling response (Babcock et al.,
1546 2009; Hu et al., 2017; Hu et al., 2020; Hwang et al., 2012; Im et al., 2018; Im et al., 2015;
1547 Kaneko et al., 2017; Lopez-Bellido et al., 2019; Ohyama et al., 2013; Ohyama et al., 2015;
1548 Robertson et al., 2013; Tracey et al., 2003). In rolling response, multiple abdominal segments
1549 respond synchronously for executing a roll (Cooney et al., 2023). Furthermore, within a hemi-
1550 segment, the muscle activation pattern moves circumferentially during the roll durations, where
1551 DL, DO, and VL muscles are active during the bend phase and LT, VO, & VA muscles
1552 transition the larval hemi-segment into a stretch phase completing a roll (Cooney et al., 2023). In
1553 cold-evoked CT responses, anterior and posterior segments reach peak activation before central
1554 segments. Within a hemi-segment individual muscles groups have unique activation profiles,
1555 where upon cold exposure both dorsal and ventral muscles reach peak response before lateral
1556 muscles. Thus, we can conclude the following. For both Cold-evoked CT and locomotion,
1557 longitudinal (dorsal and ventral) muscles contract before lateral muscles, whereas rolling
1558 response has a mixed activation pattern. The larval segments responds uniquely and dependent
1559 on the behavior being generated. In forward locomotion had a propagating wave of activation
1560 from posterior to anterior, rolling has a synchronous activation of segments and in CT response,
1561 anterior/posterior segments contract before central. The underlying circuitry responsible for
1562 generating these three unique behaviors differs based on sensory, central and motor processing
1563 modules.
1564
1565 **Methods**
1566
1567 **Fly Strains**
1568 All *Drosophila melanogaster* strains used in this study are listed in (**Table 1**). All
1569 *Drosophila* reagents were maintained on standard cornmeal-molasses-agar diet in 12:12 hour
1570 light-dark cycle at ~22°C. All experimental crosses were raised in 12:12 hour light-dark cycle at
1571 29°C, unless otherwise stated. We used two separate CIII md neuron driver lines in this
1572 study:*19-12*^{GAL4}, *R83B04*^{GAL4} and *R83B04*^{lexA}.
1573
1574 **Molecular cloning and transgenic generation of *CIII*^{lexA}**

1575 *GMR83B04*^{GAL4} was characterized as CIII md neuron driver using both optogenetics and
1576 visualization using membrane markers (Galindo et al., 2023; Himmel et al., 2023; Patel et al.,
1577 2022). The R83B04 enhancer containing entry vector was a gift from FlyLight team at Janelia
1578 Research Campus, Ashburn, VA. We performed Gateway cloning to insert R83B04 enhancer
1579 upstream of lexA. LR reaction was performed using R83B04 containing entry vector and lexA
1580 containing (pBPLexA::p65Uw) destination vector (Addgene: 26231). Transgenic fly generation
1581 was conducted by GenetiVision. *R83B04*^{lexA} was inserted in VK20 docking site using PhiC31
1582 integrase mediated transformation.
1583
1584 **EM connectomics**
1585 All data for synaptic connectivity, circuit diagrams and wire frame projections of neural
1586 cell types were extracted from Neurophyla LMB Cambridge (https://neurophyla.mrc-
1587 lmb.cam.ac.uk/). Relevant primary literature sources are cited within the main text. Sensory
1588 neurons from abdominal segments 1-4 were analyzed and for the remaining cell types, all
1589 reconstructed neurons were included (date accessed: March 04, 2022).
1590
1591 **Cold Plate Assay**
1592 We assessed requirements of neurons downstream from peripheral sensory neurons in
1593 cold-evoked responses using the cold plate assay (Patel & Cox, 2017; Patel et al., 2022; Turner
1594 et al., 2016). *GAL4* drivers for select neuronal subtypes were used to express the light chain of
1595 tetanus toxin (*UAS-TNT*). We used two sets of controls: *w1118*, genetic background control, and
1596 *Empty*^{GAL4}, which contains a GAL4 construct but no regulatory promoter (*GAL4* only control).
1597 Genetic crosses were raised on standard cornmeal-molasses-agar diet and at 29°C. To assess
1598 cold-evoked behavioral responses of age matched *Drosophila* third instar larvae, we exposed the
1599 ventral surface to noxious cold (10°C) temperatures. Briefly, using a brush we remove third
1600 instar larvae from food and place them on wet Kimwipe. Food debris is removed passively by
1601 allowing the larvae to freely locomote on wet Kimwipe. We place 6-8 larvae on a thin black
1602 metal plate that is subsequently placed on a pre-chilled (10°C) Peltier plate TE technologies
1603 Peltier plate (CP-031, TC-48-20, RS-100-12). Larval responses are recorded from above using
1604 Nikon DSLR (D5300). Changes in larval surface area were extracted using FIJI and Noldus
1605 Ethovision XT (https://github.com/CoxLabGSU/CaMPARI-intensity-and-cold-plate-assay-
1606 analysis/branches) (Patel et al., 2022). Next, we isolated individual larva from each video,
1607 removed background and used Ethovision to measure larval surface area. Using custom built r
1608 scripts, we compiled data from each larva and each genotype. Utilizing r, we calculated percent
1609 change in larval surface area (Area change= ($Area_N$ – $Average_Area_{baseline}$)/
1610 $Average_Area_{baseline}$*100). From the percent change in area dataset, we report three behavioral
1611 metrics: Average change in area, which is average percent change in area for the stimulus
1612 duration. We defined cold-evoked CT response as change in area of -10% or less for at least 0.5
1613 consecutive seconds. CT duration, time spent at or below -10% change in area. Lastly, percent

1614 CT response, which is cumulative percent of animals that CT for at least 0.5 consecutive
1615 seconds.
1616 Statistical analysis: We performed the following statistical tests for all cold plate assay
1617 data analysis. %CT response: Fisher's exact with Benjamini-Hochberg for multiple comparison.
1618 We used r for performing comparisons of percent behavior response between genotypes, we used
1619 Benjamini-Hochberg multiple comparison correction. CT duration: Kruskal-Wallis with
1620 Benjamini, Krieger and Yekutieli for multiple comparisons. CT duration data are not normal. CT
1621 magnitude: One-way ANOVA with Holm-Šídák's for multiple comparisons.
1622
1623 **Neural activation via optogenetics**
1624 We performed two types of neural activations to assess sufficiency for CT response:
1625 single downstream neural activation and co-activation, where we simultaneously activated CIII
1626 md neurons and individual downstream neurons. For optogenetic experiments in *Drosophila*, a
1627 light sensitive co-factor all *trans*-retinal (ATR) is required. For all conditions, all adult animals in
1628 the genetic cross were placed in ATR (1500µM) supplemented food and subsequently F1
1629 progeny were also raised in food containing ATR and raised in dark. For control condition, we
1630 used an $Empty^{GAL4}$ containing GAL4 construct but no regulatory promoter. Optogenetic
1631 experiments were conducted using a similar setup as previously described (Patel et al., 2022).
1632 Briefly, we used principles of dark field microscopy to enhance signal to noise ratio and capture
1633 high resolution larval videos. We created a custom dark field stage, where a Canon DSLR T3i
1634 camera captures video from above. Neural activation is performed by two blue led lights that are
1635 controlled remotely using the Noldus control box (Thorlabs: DC4100, DC4100-hub, and two
1636 M470L3-C4 led light. Noldus: mini-IO box). Larval behaviors are directly captured using
1637 Noldus Ethovision XT software, which also controls blue led activation. All optogenetic
1638 experiments were conducted in a dimly lit room. Third instar *Drosophila* larva were removed
1639 from food plug and placed onto wet Kimwipe, where larval locomotion allowed for passive
1640 removal of food debris. We lightly sprayed water onto a thin glass plate, then placed a single
1641 larva for optogenetic stimulation. The glass plate was manually moved on XY-axis to keep larva
1642 in the field of view. The following stimulus paradigm was used: 5 seconds of baseline (light off)
1643 and 5 seconds of neural activation (blue led lights on).
1644 We performed video processing and behavioral analysis using FIJI and data compilation
1645 and analysis using r (https://github.com/CoxLabGSU/Drosophila_larval_optogenetic_analysis-
1646 area_and_mobility). In order to analyze *Drosophila* larval behavioral responses, we first
1647 automatically stabilized (XY axis) and then measured changes in larval surface area and mobility
1648 (described below).
1649 Raw videos from Noldus Ethovision XT were uncompressed using video-to-video
1650 convertor (https://www.videotovideo.org/). The following steps were scripted in FIJI macro
1651 language for automatic video processing and data acquisition. For increasing processing speed,
1652 the uncompressed videos were automatically cropped to dimensions to contain all of the larva's
1653 movement. Next, using a pre-determined threshold, we created a mask followed by background

removal using erode, remove outlier and dilate functions. We then used the 'Analyze Particles' function to obtain XY coordinates of the larva in each frame. Larval movements were stabilized using XY coordinates and the 'Translate' function was used to create a highly stabilized video. Next, we measured larval surface area using automatic thresholding 'Huang method' and 'Analyze Particles' to obtain area. We define *Drosophila* larval mobility as changes in occupied pixels between two frames. We used our stabilized larval video to measure larval mobility, where larval peristaltic movements (XY displacement) are not captured. However, changes in occupied pixels resulting from turning and head sweeps are captured. Specifically, larval mobility was measured by subtracting thresholded larva in each frame from the previous frame (Raw mobility = Thresholded $larva_{Frame\ N}$ - Thresholded $larva_{Frame\ N-1}$).

Data compilation and analysis was performed in r using custom scripts. Optogenetically-evoked changes in behavior were analyzed independently for mobility and changes in area. For each larva, we calculated percent change in area (Area change= ($Area_N$ – $Average_Area_{baseline}$)/ $Average_Area_{baseline}$*100). We measured CT duration as the amount of time the larva has -10% or lower change in area. We also measure CT magnitude by analyzing average change area for stimulus duration. We report percent instantaneous CT over time as percent of animals that are at or below -10% change in area. Additionally, we report peak %CT from percent instantaneous CT dataset for each genotype. For analysis of mobility, we calculated percent change in mobility (Mobility change= ($Mobility_N$ – $Average_ Mobility_{baseline}$)/ $Average_ Mobility_{baseline}$*100). We report average percent change in mobility during stimulus for each genotype. We also plot percent immobility, which is calculated by the percent of animals with -25% or more reduction in mobility. Immobility duration is calculated based on amount of time individual animals spend at or below -25% mobility.

Statistical analysis: We performed the following statistical tests for all behavioral optogenetic data analysis. %CT peak response: Fisher's exact with Benjamini-Hochberg for multiple comparison. We used r for performing comparisons of percent behavior response between genotypes, we used Benjamini-Hochberg multiple comparison correction. CT/immobility duration: Kruskal-Wallis with Benjamini, Krieger and Yekutieli for multiple comparisons. CT duration data are not normal. CT/immobility magnitude: One-way ANOVA with Holm-Šídák's for multiple comparisons.

CT behavior across life stages - Cold Plate Assay

For assessing cold-evoked larval behavior across life stages, we developed a specialized behavior apparatus that improved to signal to noise ratios, allowed for similar stimulus magnitude between trial and across larval life stages, and an improved assay throughput. The apparatus consists of VWR circulating water chiller (model: MX7LR20), two aquarium mini-pumps (model: AD20P-1230D), custom 3D-printed water chamber with glass 1 inch glass walls, a remote control to activate the aquarium pumps (Syantek model: BHZ0320U-RF), three-way

water valve (Malida model: 607569660968), iPad screen protector (Ailun model: B0BJQ24MK7), Canon R6 with RF50mm F1.8 and RF85mm F2 macro lens and led lights for illumination from all sides (Daybetter model: FLSL-DB-501215RGBUS). The larvae were removed and cleaned as described above, then placed on a thin transparent glass plate (screen protector). The glass plate bearing larvae is placed on a 3D-printed water chamber, then pre-chilled water is piped into the chamber using mini-aquarium pumps. After the water touches the bottom of the glass plate a three-way water valve is turned off and the chilled water remains in the 3D-printed water chamber providing cold stimulation to the larvae through the glass surface. At the end of the trial, the water valve is opened to drain the water into the VWR water chiller. For first and second instar larval assays, a 85mm RF macro lens was used at different distances to increase magnification. A 50mm RF lens was used to image third instar larval cold-evoked responses.

To quantitatively analyze the larval responses, we used a slightly modified versions of FIJI and r macros as described above. In the FIJI macro, individual larvae were extracted into their individual video file and the background was removed. A technical challenge arose in the new assay, where each larva gets the cold stimulus at slightly different time point as the water filling up in the water chamber. There is a minor but consistent change in brightness/contrast for each larva, when the water below the glass plate touches the bottom of the glass plate. Using Noldus Ethovision, changes in brightness/contrast are quantified and then using r, the time of stimulus delivery is obtained. After determining the first frame automatically in r, the analysis for various cold-evoked CT response metric are obtained using the same r code as described above.

Statistical analysis: We performed the following statistical tests for all behavioral data analysis. CT magnitude and duration: One-way ANOVA with Holm-Šídák's for multiple comparisons.

CT behavior across life stages – Optogenetic Assay

To evaluate CIII-evoked CT responses across life stages, we utilized optogenetic neural activation of CIII md neurons using *ChR2-H134R* ± ATR. In order to maintain consistent blue-light based neural activation, we used Canon R6 camera mounted on AxioScope V16 Zeiss microscope for visualizing *Drosophila* larvae at life stage specific magnification while applying oblique blue light exposure (Thorlabs: DC4100, DC4100-hub, and one M470L3-C4 led light). We recorded larva responses without blue light (pre-stimulus) for 5 seconds and 5 seconds of blue light exposure. To quantitatively analyze larval responses, we used a similar method as described above for neural activation.

1733 Statistical analysis: We performed the following statistical tests for all behavioral
1734 optogenetic data analysis. CT magnitude and duration: One-way ANOVA with Holm-Šídák's for
1735 multiple comparisons.
1736
1737 **Cold-evoked Ca^{2+} responses of muscles in *Drosophila* larvae**
1738
1739 For visualizing cold-evoked Ca^{2+} responses of larval muscles in each segment, we
1740 expressed *jRCaMP1a* in *Drosophila* larval muscles using *mef2*^{GAL4} and motor neuron silencing
1741 using GtACR1 with muscle Ca^{2+} imaging. Cold stimulus was delivered using CherryTemp
1742 temperature controller (Cherry Biotech: Cherry Temp dual channel temperature control), which
1743 allows for rapid changes in temperature. To analyze *Drosophila* larval cold-evoked segmental
1744 response, we used AxioScope V16 Zeiss microscope with a Canon R6 camera mounted. *In vivo*
1745 jRCaMP1a responses were observed in third instar larva, where the larva was mounted with
1746 dorsal midline centered on the top. Using FIJI, changes in jRCaMP1a fluorescence intensities in
1747 each segment were quantified with manually drawn regions of interest (ROI). We report changes
1748 in jRCaMP1a fluorescence as $\Delta F/F = (F - F_{prestimulus}) / F_{prestimulus} * 100$ and average ΔF/F for each
1749 larval segment.
1750
1751 *Drosophila* larva's individual muscles cold-evoked Ca^{2+} responses were visualized using
1752 *mef2*^{GAL4}*> jRCaMP1a* and Zeiss LSM 780 confocal microscope with EC Plan-Neofluar 10x
1753 objective. Time-lapse acquisition was acquired at 500.11µm x 500.11µm x 307.2ms using
1754 561nm laser wavelength. Three different imaging planes (dorsal, lateral, & ventral) were used to
1755 capture the majority of the muscles of a hemi-segment. Using FIJI, changes in jRCaMP1a
1756 fluorescence intensities in each muscle were quantified with manually drawn ROIs. We report
1757 changes in jRCaMP1a fluorescence as $\Delta F/F = (F - F_{prestimulus}) / F_{prestimulus} * 100$ and maximum ΔF/F
1758 for each muscle. No statistical analyses were performed.
1759
1760 The following temperature exposure paradigm was used for both segmental and
1761 individual muscle cold-evoked Ca^{2+} response assays: Pre-stimulus (25°C for 45 seconds),
1762 temperature ramp down, steady state cold (5°C for 15 seconds), temperature ramp up, and post-
1763 stimulus (25°C for 40 seconds). Temperature ramp duration 10 seconds.
1764
1765 We used the above-mentioned Cherry Temp. dual channel temperature control system,
1766 Canon R6 and Zeiss V16 to visualize cold-evoked Ca^{2+} responses for assessing delay in mouth
1767 hook retraction (10°C stimulus) and ethyl ether pharmacological application and muscle post-
1768 synaptic density Ca^{2+} imaging (5°C stimulus). We used the following temperature exposure
1769 paradigm: pre-stimulus (20 seconds), 10 second ramp down, steady state cold (10 seconds),
1770 temperature ramp up, baseline (10 seconds), temperature ramp down, steady state cold (10
1771 seconds), temperature ramp up, baseline (10 seconds), temperature ramp down, steady state cold
1772 (10 seconds), temperature ramp up, and baseline (20 seconds). The temperature ramp duration

1773 was10 seconds. For muscle Ca^{2+} fluorescence analyses, we used $\Delta F/F = (F - F_{prestimulus})/$
1774 $F_{prestimulus} * 100$. For assessing, CIII md Ca^{2+} increase and delay in mouth hook retraction, we used
1775 $\Delta F/F = (F - F_{prestimulus})/ F_{prestimulus} * 100$ for CIII md Ca^{2+} levels and visually determined the time at
1776 which the mouth retracted.
1777
1778 Statistical analysis: Delay in mouth hook retraction - Mann-Whitney test. For motor
1779 neuron silencing assay - Two-way ANOVA with Holm-Šídák's for multiple comparisons. For
1780 pharmacology assay - Mann-Whitney test for non-parametric data and Welch's t-test for
1781 parametric data.
1782
1783
1784
1785 **CaMPARI Imaging**
1786 Post-synaptic neuron CaMPARI2 imaging: For assessing cold-evoked Ca^{2+} responses of sensory
1787 neurons and CIII md neuron downstream neurons, we utilized CaMPARI2, which upon
1788 photoconverting light and high intracellular Ca^{2+} stably photoconverts fluorescence from green
1789 to red. We performed the cold plate assay as described above. For stimulus condition, the Peltier
1790 plate was set to noxious cold (6°C) temperature and for control condition, the Peltier plate was
1791 turned off (room temperature). We placed individual third instar larvae onto the Peltier plate and
1792 simultaneously exposed the animal to photoconverting light for 20 seconds. CaMPARI2
1793 fluorescence was imaged in live, intact larvae via confocal microscopy. Zeiss LSM 780 Axio
1794 examiner microscope, Plan-Apochromat 20x objective, and excitation wavelengths of 561nm
1795 and 488nm were used to image larval ventral nerve cord or peripheral sensory neurons. We
1796 mounted live intact larva onto microscope slide and immobilized the larva by placing a
1797 coverslip, as previously described (Im et al., 2018; Patel & Cox, 2017; Patel et al., 2022; Turner
1798 et al., 2016). Three dimensional CaMPARI2 fluorescence in ventral nerve cord localized
1799 downstream neurons was imaged at 607.28µm x 607.28µm (XY resolution) and 2µm z-slices.
1800 Regions of interests were identified and area normalized fluorescence intensity for red & green
1801 signals were obtained via Imaris 9.5 software. CaMPARI responses are reported as ratio of
1802 F_{red}/F_{green}. Statistical comparisons: Parametric data – Welch's t-test and non-parametric data –
1803 Mann-Whitney test.
1804
1805 PNS CAMPARI2 imaging: Sensory neuron CaMPARI2 responses were analyzed using custom
1806 FIJI macros that automatically detected cell bodies and sholl intensity analyses were performed
1807 using semi-automated custom FIJI macros (https://github.com/CoxLabGSU/CaMPARI-intensity-
1808 and-cold-plate-assay-analysis/branches) (Patel et al., 2022).
1809 Cell body analysis – We created a set of three sequential macros that draw ROIs around
1810 the cell body, user verification of the ROIs and lastly quantification of fluorescence intensities.
1811 The first custom FIJI script generates maximum intensity projections of z-stacks, image masks
1812 were created by thresholding (Moments method) GFP signal, and next, background and dendritic

branches removed using erode and dilate functions. At the end of background clearing only cell bodies remain, where Analyze particle function is used to draw ROIs around soma. The second FIJI script is used for manual verification of each ROI and manually redrawing any incorrect ROIs. Lastly, upon ROI verification, area normalized F_{red} and F_{green} intensities are quantified. As previously described (Fosque et al., 2015; Im et al., 2018; Patel & Cox, 2017; Patel et al., 2022; Turner et al., 2016), we report evoked photoconverted CaMPARI signal as F_{red}/F_{green} ratio. Statistical comparisons: Non-parametric data – Mann-Whitney test.

Sholl intensity analysis – Sholl intensity analysis was performed using a set of two custom FIJI scripts as previously described (Patel et al., 2022). Briefly, we first perform background clearing by manually thresholding the GFP signal and select all branches and soma of neuron of interest using the "Wand Tool" in FIJI and then a mask of neuron of interest is created. The second FIJI script draws five-pixel wide radial ROIs at a single pixel interval, here only the dendrites and soma from the neuron of interest are selected at each radial interval. After Sholl ROIs are drawn, area and area normalized F_{red} and F_{green} fluorescence intensities are extracted for each radial step away from the soma. Similar to CaMPARI cell body analysis, we CaMPARI2 signal as F_{red}/F_{green} ratios away from the soma.

Ventral nerve cord CaMPARI imaging: We utilized Pan-neural (*R57C10*^{GAL4}*>CaMPARI*) driver to visualize ventral nerve cord Ca^{2+} responses to various stimuli including innocuous touch, noxious heat (45°C) and noxious cold (6°C). Stimulus and photoconverting light were delivered for 20 seconds. Whole ventral nerve cord was imaged at 607.28µm x 607.28µm (XY resolution) and 2µm z-slices. The rest of the stimulus delivery and imaging was similar to previously described CaMPARI experiments. No statistical analyses were performed.

CIII activation and second order neuron GCaMP imaging

CIII md neuron-evoked responses in downstream neurons were evaluated by using optogenetics and GCaMP. We expressed *lexAop-CsCrimson* in CIII md neurons using *R83B04*^{lexA} and used downstream neuron specific *GAL4* to drive expression of *GCaMP6m*. For experimental condition, all adult animals in the genetic cross were reared in ATR (1500µM) supplemented food and subsequently F1 progeny were also raised in food containing ATR. For control condition, adult flies and F1 progeny were raised in standard cornmeal-molasses-agar diet. Both control and experimental crosses were reared in 24hr dark. We mounted live intact third instar larva in between microscope slide and a coverslip. Larval ventral nerve cord and cells of interest were located using epifluorescence on Zeiss LSM 780 confocal microscope. Larval GCaMP6 responses were allowed to return to baseline for at least 2 minutes. Time-lapse acquisition was imaged at 250.06µm x 250.06µm x 307.2ms using 488nm laser wavelength. CIII md neural activation was performed using two oblique 617nm leds (Thorlabs M617F2 and M79L01) that were manually operated using Thorlabs led controller (Thorlabs DC4100 and DC4100-hub). We performed three sequential neural activations using the following paradigm was used: Baseline light off (30 seconds)-> neural activation (617nm for 15 seconds)-> light off (30 seconds)-> neural activation (617nm for 15 seconds)-> light off (30 seconds)-> neural

1853 activation (617nm for 15 seconds)-> light off (30 seconds). Time-lapse videos were stabilized
1854 using Stack reg – Rigid transformation in FIJI (Linkert et al., 2010; Schindelin et al., 2012;
1855 Thevenaz et al., 1998). Regions of interest were manually drawn and area normalized GCaMP
1856 fluorescence over time was exported. We report changes in GCaMP6m fluorescence as ΔF/F
1857 $=(F-F_{prestimulus})/ F_{prestimulus}*100$ and max ΔF/F for each of the three neural activation epochs.
1858 Statistical comparisons: Parametric data – Welch's t-test and non-parametric data – Mann-
1859 Whitney test.

1860 **Statistics and data visualization**

1861 Statistical analyses were performed using r (Fisher's exact test) and GraphPad Prism. All
1862 graphical visualization of the data were created using Prism GraphPad. Details on specific
1863 statistical tests are listed in respective methods section.
1864
1865

1866 ***Table 1: Drosophila melanogaster strains used in this study***

Designation	**Nomenclature**	**Source or reference**	**Identifier**	**Insertion site**
w1118		BDSC	3605	
CaMPARI2	*UAS-CaMPARI2*	BDSC	78317	attP5
ChETA	*UAS-ChETA::YFP*	BDSC	36495	attP2
ChR2	*UAS-ChR2*	BDSC	9681	Chr 3
ChR2-H134R	*UAS-H134R-ChR2*	BDSC	28995	Chr 2
CsChrimson	*LexAop2-CsChrimson.tdTomato*	BDSC	82183	VK00005
CsChrimson	*UAS-IVS-CsChrimson.mCherry*	BDSC	82180	VK00005
GCaMP6m	*UAS-GCaMP6m*	BDSC	42748	attP40
Pan-neural CaMPARI	*R57C10^{GAL4}, UAS-CaMPARI*	BDSC	58763	VK00040/ VK00020
RCaMP	*UAS-jRCaMP1a*	BDSC	63792	VK00005
SynapGCaMP6f	*Mhc-SynapGCaMP6f*	BDSC	67739	Chr 3
Muscle GCaMP + GtACR1	*w;;44H10::GCaMP6f, UAS-GtACR1*	Gift from Zarin Lab		
TnT	*UAS-TeTxLC.tnt-E2*	BDSC	28837	Chr 2
Ch	*IAV - GAL4*	BDSC	52273	Chr 3
CIII	*19-12 - GAL4*			Chr 3
CIII	*R83B04 - GAL4*	BDSC	41309	attP2
CIII	*R83B04 - lexA*	This Study		
CIII>ChETA	*19-12^{GAL4}, UAS-ChETA::YFP*	BDSC	36495	Chr 3,attP2
CIV	*ppk - GAL4*	BDSC	32079	Chr 3

Mef2	*Mef2-GAL4*	BDSC	27390	Chr 3
Empty$^{GAL4'}$	*w;;attP2*	BDSC	68384	attP2
Empty$^{GAL4''}$	*w;attP40;attP2*	Gift from Rubin Lab		attP40;attP2
A00c	*R71A10 - GAL4*	BDSC	39562	attP2
A01d3	*SS02065 - splitGAL4*	Gift from Nose Lab		attP40;attP2
A02e	*R70C01 - GAL4*	BDSC	39520	attP2
A02f	*SS01792 - GAL4*	Gift from Zlatic & Ohyama Labs		attP40;attP2
A02g	*R36G02 - GAL4*	BDSC	49939	attP2
A02o	*MB120B - splitGAL4*	Gift from Nose Lab		attP40;attP2
A05q	*R47D07 - GAL4*	BDSC	50304	attP2
A08n	*R82E12 - GAL4*	BDSC	40153	attP2
A09e	*SS00878 - splitGAL4*	Gift from Zlatic Lab		attP40;attP2
A27k	*SS026694 - splitGAL4*	Gift from Nose Lab		attP40;attP2
A31k	*SS04399 - splitGAL4*	Gift from Zarin Lab		attP40;attP2
All Basin	*R72F11 - GAL4*	BDSC	39786	attP2
Basin-1	*R20B01 - GAL4*	BDSC	48877	attP2
Basin-2	*SS00739 - splitGAL4*	Gift from Zlatic Lab		attP40;attP2
Basin-4	*SS00740 - splitGAL4*	Gift from Zlatic Lab		attP40;attP2
Chair-1	*SS00911 - splitGAL4*	Gift from Zlatic Lab		attP40;attP2
dILP7	*ILP7 – GAL4*	Gift from Jan Lab		
DnB'	*IT4051 - GAL4*	Gift from Grueber Lab		Chr 3
DnB''	*IT412 - GAL4*	BDSC	63300	Chr 3
Goro	*R69F06 - GAL4*	BDSC	39497	attP2
mCSI	*R94B10 - GAL4*	BDSC	41325	attP2
R61A01/TePns	*R61A01 - GAL4*	BDSC	39269	attP2
D42	*D42 – GAL4*	BDSC	8816	Chr 3

1867

1868 **Data availability statement**

1869 The original contributions presented in the study are included in the article/Supplementary
1870 material, further inquiries can be directed to the corresponding author.

1871

1872 **Conflict of Interest**

1873 The authors declare that the research was conducted in the absence of any commercial or
1874 financial relationships that could be construed as a potential conflict of interest.
1875

1876 **Author Contributions**

1877 Conceptualization: AAP and DNC. Methodology: AAP, and DNC. Cold-plate assays: AAP;
1878 Optogenetics, AAP; Calcium imaging: AAP. Statistics and other formal analyses: AAP. EM
1879 Connectome analysis: AAP and AC. Writing – Original Draft: AAP and DNC; Writing – Review
1880 & Editing: AAP, AC and DNC. Visualization: AAP. Supervision: DNC. Funding acquisition:
1881 DNC.
1882

1883 **Funding**

1884 This work was supported by NIH R01 NS115209 (to DNC). AAP was supported by a Brains &
1885 Behavior Fellowship, a 2CI Neurogenomics Fellowship, and a Kenneth W. and Georganne F.
1886 Honeycutt Fellowship from Georgia State University. AC thanks the Wellcome Trust (award
1887 205038/Z/16/Z and 205038/A/16/Z) and the HHMI Janelia Resarch Campus for funding.
1888

1889 **Acknowledgments**

1890 We thank members of Cox Lab and Michael J. Galko (MD Anderson Cancer Center) for critical
1891 comments on the manuscript. We thank Shatabdi Bhattacharjee for sharing insightful feedback
1892 on the manuscript. We thank the Janelia Visiting Scientist program hosted by HHMI Janelia
1893 Research Campus for providing critical training in EM connectomics. We thank members of the
1894 *Drosophila* research community for sharing reagents: Gerald M. Rubin, Marta Zlatic, Tomoko
1895 Ohyama, Aref Zarin, Akinao Nose, Yuh Nung Jan, Lily Jan and Wesley Grueber. We
1896 acknowledge the Georgia State University Imaging Core Facility for training and instrument
1897 support associated with this work.
1898

1899 **References**

1900 Andrade, I. V., Riebli, N., Nguyen, B. M., Omoto, J. J., Cardona, A., & Hartenstein, V. (2019,
1901 Feb 4). Developmentally Arrested Precursors of Pontine Neurons Establish an Embryonic

Blueprint of the Drosophila Central Complex. *Curr Biol, 29*(3), 412-425 e413. https://doi.org/10.1016/j.cub.2018.12.012

Arnadóttir, J., O'Hagan, R., Chen, Y., Goodman, M. B., & Chalfie, M. (2011, 2011/8//). The DEG/ENaC protein MEC-10 regulates the transduction channel complex in Caenorhabditis elegans touch receptor neurons. *The Journal of neuroscience : the official journal of the Society for Neuroscience, 31*(35), 12695-12704. https://doi.org/10.1523/JNEUROSCI.4580-10.2011

Babcock, D. T., Landry, C., & Galko, M. J. (2009, 2009/5//). Cytokine signaling mediates UV-induced nociceptive sensitization in Drosophila larvae. *Current biology : CB, 19*(10), 799-806. https://doi.org/10.1016/j.cub.2009.03.062

Babcock, Daniel T., Shi, S., Jo, J., Shaw, M., Gutstein, Howard B., & Galko, Michael J. (2011, 2011/9//). Hedgehog Signaling Regulates Nociceptive Sensitization. *Current Biology, 21*(18), 1525-1533. https://doi.org/10.1016/j.cub.2011.08.020

Balakrishnan, M., Yu, S. F., Chin, S. M., Soffar, D. B., Windner, S. E., Goode, B. L., & Baylies, M. K. (2020, 2020/07/21/). Cofilin Loss in Drosophila Muscles Contributes to Muscle Weakness through Defective Sarcomerogenesis during Muscle Growth. *Cell Reports, 32*(3), 107893. https://doi.org/https://doi.org/10.1016/j.celrep.2020.107893

Bandell, M., & Patapoutian, A. (2009, 2009/12//). Itching for insight. *Cell, 139*(7), 1224-1226. https://doi.org/10.1016/j.cell.2009.12.012

Bellardita, C., & Kiehn, O. (2015, Jun 1). Phenotypic characterization of speed-associated gait changes in mice reveals modular organization of locomotor networks. *Curr Biol, 25*(11), 1426-1436. https://doi.org/10.1016/j.cub.2015.04.005

Berck, M. E., Khandelwal, A., Claus, L., Hernandez-Nunez, L., Si, G., Tabone, C. J., Li, F., Truman, J. W., Fetter, R. D., Louis, M., Samuel, A. D. T., & Cardona, A. (2016). The wiring diagram of a glomerular olfactory system. https://doi.org/10.7554/eLife.14859.001

Berkowitz, A., Roberts, A., & Soffe, S. R. (2010). Roles for multifunctional and specialized spinal interneurons during motor pattern generation in tadpoles, zebrafish larvae, and turtles. *Front Behav Neurosci, 4*, 36. https://doi.org/10.3389/fnbeh.2010.00036

Berndt, A., Schoenenberger, P., Mattis, J., Tye, K. M., Deisseroth, K., Hegemann, P., & Oertner, T. G. (2011, May 3). High-efficiency channelrhodopsins for fast neuronal stimulation at low light levels. *Proceedings of the National Academy of Sciences of the United States of America, 108*(18), 7595-7600. https://doi.org/10.1073/pnas.1017210108

Boyden, E. S., Zhang, F., Bamberg, E., Nagel, G., & Deisseroth, K. (2005, Sep). Millisecond-timescale, genetically targeted optical control of neural activity. *Nat Neurosci, 8*(9), 1263-1268. https://doi.org/10.1038/nn1525

Burgos, A., Honjo, K., Ohyama, T., Qian, C. S., Shin, G. J.-e., Gohl, D. M., Silies, M., Tracey, W. D., Zlatic, M., Cardona, A., & Grueber, W. B. (2018, 2018/3//). Nociceptive interneurons control modular motor pathways to promote escape behavior in Drosophila. *eLife, 7*. https://doi.org/10.7554/eLife.26016

Bushnell, M. C., Duncan, G. H., Dubner, R., Jones, R. L., & Maixner, W. (1985, May). Attentional influences on noxious and innocuous cutaneous heat detection in humans and monkeys. *J Neurosci, 5*(5), 1103-1110. https://doi.org/10.1523/JNEUROSCI.05-05-01103.1985

Caldwell, J. C., Miller, M. M., Wing, S., Soll, D. R., & Eberl, D. F. (2003, 2003/12/23). Dynamic analysis of larval locomotion in Drosophila chordotonal organ mutants. *Proceedings of the National Academy of Sciences, 100*(26), 16053-16058. https://doi.org/10.1073/pnas.2535546100

Carreira-Rosario, A., Zarin, A. A., Clark, M. Q., Manning, L., Fetter, R. D., Cardona, A., & Doe, C. Q. (2018, 2018/8//). MDN brain descending neurons coordinately activate backward and inhibit forward locomotion. *eLife, 7*. https://doi.org/10.7554/eLife.38554

Chrispin, J., Martin, S. S., Hasan, R. K., Joshi, P. H., Minder, C. M., McEvoy, J. W., Kohli, P., Johnson, A. E., Wang, L., Blaha, M. J., & Blumenthal, R. S. (2013, Sep). Landmark lipid-lowering trials in the primary prevention of cardiovascular disease. *Clin Cardiol, 36*(9), 516-523. https://doi.org/10.1002/clc.22147

Clark, M. Q., Zarin, A. A., Carreira-Rosario, A., & Doe, C. Q. (2018, 2018/12//). Neural circuits driving larval locomotion in Drosophila. *Neural Development, 13*(1), 6-6. https://doi.org/10.1186/s13064-018-0103-z

Cooney, P. C., Li, W., Huang, Y., Hormigo, R., Tabachnik, T., Hillman, E. M. C., Grueber, W. B., & Zarin, A. A. (2023). Neuromuscular Basis of Drosophila larval escape behavior. *bioRxiv*, 2023.2002.2001.526733. https://doi.org/10.1101/2023.02.01.526733

Corfas, R. A., & Vosshall, L. B. (2015, 2015/12//). The cation channel TRPA1 tunes mosquito thermotaxis to host temperatures. *eLife, 4*. https://doi.org/10.7554/eLife.11750

Coste, B., Mathur, J., Schmidt, M., Earley, T. J., Ranade, S., Petrus, M. J., Dubin, A. E., & Patapoutian, A. (2010, 2010/10//). Piezo1 and Piezo2 are essential components of distinct mechanically activated cation channels. *Science (New York, N.Y.), 330*(6000), 55-60. https://doi.org/10.1126/science.1193270

Dannhauser, S., Lux, T. J., Hu, C., Selcho, M., Chen, J. T., Ehmann, N., Sachidanandan, D., Stopp, S., Pauls, D., Pawlak, M., Langenhan, T., Soba, P., Rittner, H. L., & Kittel, R. J. (2020, Sep 30). Antinociceptive modulation by the adhesion GPCR CIRL promotes mechanosensory signal discrimination. *eLife, 9*. https://doi.org/10.7554/eLife.56738

Demontis, F., & Perrimon, N. (2009, Mar). Integration of Insulin receptor/Foxo signaling and dMyc activity during muscle growth regulates body size in Drosophila. *Development, 136*(6), 983-993. https://doi.org/10.1242/dev.027466

Derby, C. D., Kozma, M. T., Senatore, A., & Schmidt, M. (2016, Jun). Molecular Mechanisms of Reception and Perireception in Crustacean Chemoreception: A Comparative Review. *Chem Senses, 41*(5), 381-398. https://doi.org/10.1093/chemse/bjw057

Dietrich, S., Company, C., Song, K., Lowenstein, E. D., Riedel, L., Birchmeier, C., Gargiulo, G., & Zampieri, N. (2022, Nov 11). Molecular identity of proprioceptor subtypes innervating different muscle groups in mice. *Nat Commun, 13*(1), 6867. https://doi.org/10.1038/s41467-022-34589-8

Eichler, K., Li, F., Litwin-Kumar, A., Park, Y., Andrade, I., Schneider-Mizell, C. M., Saumweber, T., Huser, A., Eschbach, C., Gerber, B., Fetter, R. D., Truman, J. W., Priebe, C. E., Abbott, L. F., Thum, A. S., Zlatic, M., & Cardona, A. (2017, 2017/8//). The complete connectome of a learning and memory centre in an insect brain. *Nature, 548*(7666), 175-182. https://doi.org/10.1038/nature23455

Eschbach, C., Fushiki, A., Winding, M., Schneider-Mizell, C. M., Shao, M., Arruda, R., Eichler, K., Valdes-Aleman, J., Ohyama, T., Thum, A. S., Gerber, B., Fetter, R. D., Truman, J. W., Litwin-Kumar, A., Cardona, A., & Zlatic, M. (2020, Apr). Recurrent architecture for adaptive regulation of learning in the insect brain. *Nat Neurosci, 23*(4), 544-555. https://doi.org/10.1038/s41593-020-0607-9

Eschbach, C., & Zlatic, M. (2020, Dec). Useful road maps: studying Drosophila larva's central nervous system with the help of connectomics. *Curr Opin Neurobiol, 65*, 129-137. https://doi.org/10.1016/j.conb.2020.09.008

Fosque, B. F., Sun, Y., Dana, H., Yang, C. T., Ohyama, T., Tadross, M. R., Patel, R., Zlatic, M., Kim, D. S., Ahrens, M. B., Jayaraman, V., Looger, L. L., & Schreiter, E. R. (2015, 2015/2//). Labeling of active neural circuits in vivo with designed calcium integrators. *Science, 347*(6223), 755-760. https://doi.org/10.1126/science.1260922

Fowler, M. A., & Montell, C. (2013, 2013/3//). Drosophila TRP channels and animal behavior. *Life sciences, 92*(8-9), 394-403. https://doi.org/10.1016/j.lfs.2012.07.029

Frank, D. D., Enjin, A., Jouandet, G. C., Zaharieva, E. E., Para, A., Stensmyr, M. C., & Gallio, M. (2017, 2017/8//). Early Integration of Temperature and Humidity Stimuli in the Drosophila Brain. *Current Biology, 27*(15), 2381-2388.e2384. https://doi.org/10.1016/j.cub.2017.06.077

Frank, D. D., Jouandet, G. C., Kearney, P. J., Macpherson, L. J., & Gallio, M. (2015, 2015/3//). Temperature representation in the Drosophila brain. *Nature, 519*(7543), 358-361. https://doi.org/10.1038/nature14284

Freeman, E. G., & Dahanukar, A. (2015). Molecular neurobiology of Drosophila taste. *Current Opinion in Neurobiology, 34*, 140-148. https://doi.org/10.1016/j.conb.2015.06.001

Fushiki, A., Zwart, M. F., Kohsaka, H., Fetter, R. D., Cardona, A., & Nose, A. (2016, 2016/2//). A circuit mechanism for the propagation of waves of muscle contraction in Drosophila. *eLife, 5*. https://doi.org/10.7554/eLife.13253

Galindo, S. E., Wood, A. J., Cooney, P. C., Hammond, L. A., & Grueber, W. B. (2023, Mar 1). Axon-axon interactions determine modality-specific wiring and subcellular synaptic specificity in a somatosensory circuit. *Development, 150*(5). https://doi.org/10.1242/dev.199832

Gallio, M., Ofstad, T. A., Macpherson, L. J., Wang, J. W., & Zuker, C. S. (2011, Feb 18). The coding of temperature in the Drosophila brain. *Cell, 144*(4), 614-624. https://doi.org/10.1016/j.cell.2011.01.028

Garner, A. (2020). *Identification of neural premotor substrates affecting escape behaviours in Drosophila larvae* [Master's thesis, McGill University]. https://escholarship.mcgill.ca/concern/theses/th83m403v

Gerhard, S., Andrade, I., Fetter, R. D., Cardona, A., & Schneider-Mizell, C. M. (2017, 2017/10//). Conserved neural circuit structure across Drosophila larval development revealed by comparative connectomics. *eLife, 6*. https://doi.org/10.7554/eLife.29089

Green, C. S., & Soffe, S. R. (1996, 1996/02/01). Transitions between two different motor patterns in Xenopus embryos. *Journal of Comparative Physiology A, 178*(2), 279-291. https://doi.org/10.1007/BF00188169

Gunaydin, L. A., Yizhar, O., Berndt, A., Sohal, V. S., Deisseroth, K., & Hegemann, P. (2010, 2010/3//). Ultrafast optogenetic control. *Nature Neuroscience, 13*(3), 387-392. https://doi.org/10.1038/nn.2495

He, L., Gulyanon, S., Skanata, M. M., Karagyozov, D., Heckscher, E., Krieg, M., Tschekpenakis, G., Gershow, M., & Tracey, D. (2018, 2018/11//). Proprioceptive neurons of larval Drosophila melanogaster show direction selective activity requiring the mechanosensory channel TMC. *bioRxiv*, 463216-463216. https://doi.org/10.1101/463216

Heckscher, E. S., Lockery, S. R., & Doe, C. Q. (2012). Characterization of *Drosophila* Larval Crawling at the Level of Organism, Segment, and Somatic Body Wall Musculature. *The Journal of Neuroscience, 32*(36), 12460. https://doi.org/10.1523/JNEUROSCI.0222-12.2012

Heckscher, Ellie S., Zarin, Aref A., Faumont, S., Clark, Matthew Q., Manning, L., Fushiki, A., Schneider-Mizell, Casey M., Fetter, Richard D., Truman, James W., Zwart, Maarten F., Landgraf, M., Cardona, A., Lockery, Shawn R., & Doe, Chris Q. (2015, 2015/10//). Even-Skipped+ Interneurons Are Core Components of a Sensorimotor Circuit that

Maintains Left-Right Symmetric Muscle Contraction Amplitude. *Neuron, 88*(2), 314-329. https://doi.org/10.1016/J.NEURON.2015.09.009

Herculano-Houzel, S. (2009). The human brain in numbers: a linearly scaled-up primate brain. *Front Hum Neurosci, 3*, 31. https://doi.org/10.3389/neuro.09.031.2009

Hernandez-Nunez, L., Chen, A., Budelli, G., Berck, M. E., Richter, V., Rist, A., Thum, A. S., Cardona, A., Klein, M., Garrity, P., & Samuel, A. D. T. (2021). Synchronous and opponent thermosensors use flexible cross-inhibition to orchestrate thermal homeostasis. *Science Advances, 7*(35), eabg6707. https://doi.org/doi:10.1126/sciadv.abg6707

Himmel, N. J., Letcher, J. M., Sakurai, A., Gray, T. R., Benson, M. N., & Cox, D. N. (2019, Nov 11). Drosophila menthol sensitivity and the Precambrian origins of transient receptor potential-dependent chemosensation. *Philos Trans R Soc Lond B Biol Sci, 374*(1785), 20190369. https://doi.org/10.1098/rstb.2019.0369

Himmel, N. J., Letcher, J. M., Sakurai, A., Gray, T. R., Benson, M. N., Donaldson, K. J., & Cox, D. N. (2021, Jun 25). Identification of a neural basis for cold acclimation in Drosophila larvae. *iScience, 24*(6), 102657. https://doi.org/10.1016/j.isci.2021.102657

Himmel, N. J., Patel, A. A., & Cox, D. N. (2017). *Invertebrate Nociception* (Vol. 1). Oxford University Press. https://doi.org/10.1093/acrefore/9780190264086.013.166

Himmel, N. J., Sakurai, A., Donaldson, K. J., & Cox, D. N. (2022, Sep 16). Protocols for measuring cold-evoked neural activity and cold tolerance in Drosophila larvae following fictive cold acclimation. *STAR Protoc, 3*(3), 101510. https://doi.org/10.1016/j.xpro.2022.101510

Himmel, N. J., Sakurai, A., Patel, A. A., Bhattacharjee, S., Letcher, J. M., Benson, M. N., Gray, T. R., Cymbalyuk, G. S., & Cox, D. N. (2023, Jan 23). Chloride-dependent mechanisms of multimodal sensory discrimination and nociceptive sensitization in Drosophila. *eLife, 12*. https://doi.org/10.7554/eLife.76863

Hiramoto, A., Jonaitis, J., Niki, S., Kohsaka, H., Fetter, R. D., Cardona, A., Pulver, S. R., & Nose, A. (2021, May 19). Regulation of coordinated muscular relaxation in Drosophila larvae by a pattern-regulating intersegmental circuit. *Nat Commun, 12*(1), 2943. https://doi.org/10.1038/s41467-021-23273-y

Hu, C., Petersen, M., Hoyer, N., Spitzweck, B., Tenedini, F., Wang, D., Gruschka, A., Burchardt, L. S., Szpotowicz, E., Schweizer, M., Guntur, A. R., Yang, C.-H., & Soba, P. (2017, 2017/8//). Sensory integration and neuromodulatory feedback facilitate Drosophila mechanonociceptive behavior. *Nature Neuroscience, 20*(8), 1085-1095. https://doi.org/10.1038/nn.4580

Hu, Y., Wang, C., Yang, L., Pan, G., Liu, H., Yu, G., & Ye, B. (2020, Dec 21). A Neural Basis for Categorizing Sensory Stimuli to Enhance Decision Accuracy. *Curr Biol, 30*(24), 4896-4909 e4896. https://doi.org/10.1016/j.cub.2020.09.045

Huang, Y., & Zarin, A. A. (2022). A premotor microcircuit to generate behavior-specific muscle activation patterns in Drosophila larvae. *bioRxiv*, 2022.2008.2018.504452. https://doi.org/10.1101/2022.08.18.504452

Huckesfeld, S., Schlegel, P., Miroschnikow, A., Schoofs, A., Zinke, I., Haubrich, A. N., Schneider-Mizell, C. M., Truman, J. W., Fetter, R. D., Cardona, A., & Pankratz, M. J. (2021, Jun 4). Unveiling the sensory and interneuronal pathways of the neuroendocrine connectome in Drosophila. *eLife, 10*. https://doi.org/10.7554/eLife.65745

Hwang, R. Y., Stearns, N. A., & Tracey, W. D. (2012, 2012/1//). The Ankyrin Repeat Domain of the TRPA Protein Painless Is Important for Thermal Nociception but Not Mechanical Nociception. *PLoS One, 7*(1), e30090-e30090. https://doi.org/10.1371/journal.pone.0030090

Im, S. H., Patel, A. A., Cox, D. N., & Galko, M. J. (2018, 2018/5//). Drosophila Insulin receptor regulates the persistence of injury-induced nociceptive sensitization. *Disease Models & Mechanisms, 11*(5), dmm034231-dmm034231. https://doi.org/10.1242/dmm.034231

Im, S. H., Takle, K., Jo, J., Babcock, D. T., Ma, Z., Xiang, Y., & Galko, M. J. (2015). Tachykinin acts upstream of autocrine Hedgehog signaling during nociceptive sensitization in Drosophila. *eLife, 4*. https://doi.org/10.7554/eLife.10735

Imambocus, B. N., Zhou, F., Formozov, A., Wittich, A., Tenedini, F. M., Hu, C., Sauter, K., Macarenhas Varela, E., Heredia, F., Casimiro, A. P., Macedo, A., Schlegel, P., Yang, C. H., Miguel-Aliaga, I., Wiegert, J. S., Pankratz, M. J., Gontijo, A. M., Cardona, A., & Soba, P. (2022, Jan 10). A neuropeptidergic circuit gates selective escape behavior of Drosophila larvae. *Curr Biol, 32*(1), 149-163 e148. https://doi.org/10.1016/j.cub.2021.10.069

Imura, E., Shimada-Niwa, Y., Nishimura, T., Huckesfeld, S., Schlegel, P., Ohhara, Y., Kondo, S., Tanimoto, H., Cardona, A., Pankratz, M. J., & Niwa, R. (2020, Jun 8). The Corazonin-PTTH Neuronal Axis Controls Systemic Body Growth by Regulating Basal Ecdysteroid Biosynthesis in Drosophila melanogaster. *Curr Biol, 30*(11), 2156-2165 e2155. https://doi.org/10.1016/j.cub.2020.03.050

Jenett, A., Rubin, Gerald M., Ngo, T.-T. B., Shepherd, D., Murphy, C., Dionne, H., Pfeiffer, Barret D., Cavallaro, A., Hall, D., Jeter, J., Iyer, N., Fetter, D., Hausenfluck, Joanna H., Peng, H., Trautman, Eric T., Svirskas, Robert R., Myers, Eugene W., Iwinski, Zbigniew R., Aso, Y., DePasquale, Gina M., Enos, A., Hulamm, P., Lam, Shing Chun B., Li, H.-H., Laverty, Todd R., Long, F., Qu, L., Murphy, Sean D., Rokicki, K., Safford, T., Shaw, K., Simpson, Julie H., Sowell, A., Tae, S., Yu, Y., & Zugates, Christopher T.

(2012, 2012/10//). A GAL4-Driver Line Resource for Drosophila Neurobiology. *Cell Reports, 2*(4), 991-1001. https://doi.org/10.1016/j.celrep.2012.09.011

Jovanic, T., Schneider-Mizell, C. M., Shao, M., Masson, J.-B., Denisov, G., Fetter, R. D., Mensh, B. D., Truman, J. W., Cardona, A., & Zlatic, M. (2016, 2016/10//). Competitive Disinhibition Mediates Behavioral Choice and Sequences in Drosophila. *Cell, 167*(3), 858-870.e819. https://doi.org/10.1016/j.cell.2016.09.009

Jovanic, T., Winding, M., Cardona, A., Truman, J. W., Gershow, M., & Zlatic, M. (2019, Feb 18). Neural Substrates of Drosophila Larval Anemotaxis. *Curr Biol, 29*(4), 554-566 e554. https://doi.org/10.1016/j.cub.2019.01.009

Kaneko, T., Macara, A. M., Li, R., Hu, Y., Iwasaki, K., Dunnings, Z., Firestone, E., Horvatic, S., Guntur, A., Shafer, O. T., Yang, C.-H., Zhou, J., & Ye, B. (2017, 2017/8//). Serotonergic Modulation Enables Pathway-Specific Plasticity in a Developing Sensory Circuit in Drosophila. *Neuron, 95*(3), 623-638.e624. https://doi.org/10.1016/j.neuron.2017.06.034

Klapoetke, N. C., Murata, Y., Kim, S. S., Pulver, S. R., Birdsey-Benson, A., Cho, Y. K., Morimoto, T. K., Chuong, A. S., Carpenter, E. J., Tian, Z., Wang, J., Xie, Y., Yan, Z., Zhang, Y., Chow, B. Y., Surek, B., Melkonian, M., Jayaraman, V., Constantine-Paton, M., Wong, G. K.-S., & Boyden, E. S. (2014, 2014/3//). Independent optical excitation of distinct neural populations. *Nature Methods, 11*(3), 338-346. https://doi.org/10.1038/nmeth.2836

Klein, M., Afonso, B., Vonner, A. J., Hernandez-Nunez, L., Berck, M., Tabone, C. J., Kane, E. A., Pieribone, V. A., Nitabach, M. N., Cardona, A., Zlatic, M., Sprecher, S. G., Gershow, M., Garrity, P. A., & Samuel, A. D. (2015, Jan 13). Sensory determinants of behavioral dynamics in Drosophila thermotaxis. *Proc Natl Acad Sci U S A, 112*(2), E220-229. https://doi.org/10.1073/pnas.1416212112

Kohsaka, H., Guertin, P. A., & Nose, A. (2017, 2017/5//). Neural Circuits Underlying Fly Larval Locomotion. *Current Pharmaceutical Design, 23*(12), 1722-1733. https://doi.org/10.2174/1381612822666161208120835

Kohsaka, H., Takasu, E., Morimoto, T., & Nose, A. (2014, 2014/11//). A Group of Segmental Premotor Interneurons Regulates the Speed of Axial Locomotion in Drosophila Larvae. *Current Biology, 24*(22), 2632-2642. https://doi.org/10.1016/j.cub.2014.09.026

Kohsaka, H., Zwart, M. F., Fushiki, A., Fetter, R. D., Truman, J. W., Cardona, A., & Nose, A. (2019, 2019/06/14). Regulation of forward and backward locomotion through intersegmental feedback circuits in Drosophila larvae. *Nature Communications, 10*(1), 2654. https://doi.org/10.1038/s41467-019-10695-y

Larderet, I., Fritsch, P. M. J., Gendre, N., Larisa Neagu-Maier, G., Fetter, R. D., Schneider-Mizell, C. M., Truman, J. W., Zlatic, M., Cardona, A., & Sprecher, S. G. (2017).

Organization of the Drosophila larval visual circuit. https://doi.org/10.7554/eLife.28387.001

Leung, N. Y., & Montell, C. (2017, Oct 6). Unconventional Roles of Opsins. *Annu Rev Cell Dev Biol, 33*, 241-264. https://doi.org/10.1146/annurev-cellbio-100616-060432

Liao, J. C., & Fetcho, J. R. (2008, Nov 26). Shared versus specialized glycinergic spinal interneurons in axial motor circuits of larval zebrafish. *J Neurosci, 28*(48), 12982-12992. https://doi.org/10.1523/JNEUROSCI.3330-08.2008

Liu, L., Yermolaieva, O., Johnson, W. A., Abboud, F. M., & Welsh, M. J. (2003, Mar). Identification and function of thermosensory neurons in Drosophila larvae. *Nat Neurosci, 6*(3), 267-273. https://doi.org/10.1038/nn1009

Liu, Y., Hasegawa, E., Nose, A., Zwart, M. F., & Kohsaka, H. (2023, 2023/08/08). Synchronous multi-segmental activity between metachronal waves controls locomotion speed in Drosophila larvae. *eLife, 12*, e83328. https://doi.org/10.7554/eLife.83328

Lopez-Bellido, R., Himmel, N. J., Gutstein, H. B., Cox, D. N., & Galko, M. J. (2019, Nov 11). An assay for chemical nociception in Drosophila larvae. *Philos Trans R Soc Lond B Biol Sci, 374*(1785), 20190282. https://doi.org/10.1098/rstb.2019.0282

Macpherson, L. J., Zaharieva, E. E., Kearney, P. J., Alpert, M. H., Lin, T.-Y., Turan, Z., Lee, C.-H., & Gallio, M. (2015, 2015/12//). Dynamic labelling of neural connections in multiple colours by trans-synaptic fluorescence complementation. *Nature Communications, 6*(1), 10024-10024. https://doi.org/10.1038/ncomms10024

Maksymchuk, N., Sakurai, A., Cox, D. N., & Cymbalyuk, G. (2022). Transient and Steady-State Properties of Drosophila Sensory Neurons Coding Noxious Cold Temperature [Original Research]. *Frontiers in Cellular Neuroscience, 16*. https://www.frontiersin.org/articles/10.3389/fncel.2022.831803

Maksymchuk, N., Sakurai, A., Cox, D. N., & Cymbalyuk, G. S. (2023, Sep 27). Cold-Temperature Coding with Bursting and Spiking Based on TRP Channel Dynamics in Drosophila Larva Sensory Neurons. *Int J Mol Sci, 24*(19). https://doi.org/10.3390/ijms241914638

Mark, B., Lai, S. L., Zarin, A. A., Manning, L., Pollington, H. Q., Litwin-Kumar, A., Cardona, A., Truman, J. W., & Doe, C. Q. (2021, May 11). A developmental framework linking neurogenesis and circuit formation in the Drosophila CNS. *eLife, 10*. https://doi.org/10.7554/eLife.67510

Masson, J. B., Laurent, F., Cardona, A., Barre, C., Skatchkovsky, N., Zlatic, M., & Jovanic, T. (2020, Feb). Identifying neural substrates of competitive interactions and sequence transitions during mechanosensory responses in Drosophila. *PLoS Genet, 16*(2), e1008589. https://doi.org/10.1371/journal.pgen.1008589

Miroschnikow, A., Schlegel, P., Schoofs, A., Hueckesfeld, S., Li, F., Schneider-Mizell, C. M., Fetter, R. D., Truman, J., Cardona, A., & Pankratz, M. J. (2018, 2018/7//). The Feeding Connectome: Convergence of Monosynaptic and Polysynaptic Sensory Paths onto Common Motor Outputs. *bioRxiv*, 368878-368878. https://doi.org/10.1101/368878

Moehring, F., Cowie, A. M., Menzel, A. D., Weyer, A. D., Grzybowski, M., Arzua, T., Geurts, A. M., Palygin, O., & Stucky, C. L. (2018, Jan 16). Keratinocytes mediate innocuous and noxious touch via ATP-P2X4 signaling. *eLife, 7*. https://doi.org/10.7554/eLife.31684

Montell, C. (2021, Mar 3). Drosophila sensory receptors-a set of molecular Swiss Army Knives. *Genetics, 217*(1), 1-34. https://doi.org/10.1093/genetics/iyaa011

Nakamura, K. (2018). Afferent pathways for autonomic and shivering thermoeffectors. *Handb Clin Neurol, 156*, 263-279. https://doi.org/10.1016/B978-0-444-63912-7.00016-3

Ohyama, T., Jovanic, T., Denisov, G., Dang, T. C., Hoffmann, D., Kerr, R. A., & Zlatic, M. (2013, 2013/8//). High-Throughput Analysis of Stimulus-Evoked Behaviors in Drosophila Larva Reveals Multiple Modality-Specific Escape Strategies. *PLoS One, 8*(8), e71706-e71706. https://doi.org/10.1371/journal.pone.0071706

Ohyama, T., Schneider-Mizell, C. M., Fetter, R. D., Aleman, J. V., Franconville, R., Rivera-Alba, M., Mensh, B. D., Branson, K. M., Simpson, J. H., Truman, J. W., Cardona, A., & Zlatic, M. (2015, 2015/4//). A multilevel multimodal circuit enhances action selection in Drosophila. *Nature, 520*(7549), 633-639. https://doi.org/10.1038/nature14297

Ormerod, K. A.-O., Scibelli, A. E., & Littleton, J. A.-O. (2022). Regulation of excitation-contraction coupling at the Drosophila neuromuscular junction. *The Journal of Physiology, 600 (2)*(349–372). https://doi.org/https://doi.org/10.1113/JP282092

Patel, A., & Cox, D. (2017). Behavioral and Functional Assays for Investigating Mechanisms of Noxious Cold Detection and Multimodal Sensory Processing in Drosophila Larvae. *BIO-PROTOCOL, 7*(13). https://doi.org/10.21769/BioProtoc.2388

Patel, A. A., Sakurai, A., Himmel, N. J., & Cox, D. N. (2022). Modality specific roles for metabotropic GABAergic signaling and calcium induced calcium release mechanisms in regulating cold nociception. *bioRxiv*, 2022.2005.2012.491647. https://doi.org/10.1101/2022.05.12.491647

Pfeiffer, B. D., Jenett, A., Hammonds, A. S., Ngo, T. T., Misra, S., Murphy, C., Scully, A., Carlson, J. W., Wan, K. H., Laverty, T. R., Mungall, C., Svirskas, R., Kadonaga, J. T., Doe, C. Q., Eisen, M. B., Celniker, S. E., & Rubin, G. M. (2008, Jul 15). Tools for neuroanatomy and neurogenetics in Drosophila. *Proc Natl Acad Sci U S A, 105*(28), 9715-9720. https://doi.org/10.1073/pnas.0803697105

Robertson, J. L., Tsubouchi, A., & Tracey, W. D. (2013). Larval defense against attack from parasitoid wasps requires nociceptive neurons. *PLoS One, 8*(10), e78704-e78704. https://doi.org/10.1371/journal.pone.0078704

Saalfeld, S., Cardona, A., Hartenstein, V., & Tomancak, P. (2009, Aug 1). CATMAID: collaborative annotation toolkit for massive amounts of image data. *Bioinformatics, 25*(15), 1984-1986. https://doi.org/10.1093/bioinformatics/btp266

Salvaterra, P. M., & Kitamoto, T. (2001, Aug). Drosophila cholinergic neurons and processes visualized with Gal4/UAS-GFP. *Brain Res Gene Expr Patterns, 1*(1), 73-82. https://doi.org/10.1016/s1567-133x(01)00011-4

Saumweber, T., Rohwedder, A., Schleyer, M., Eichler, K., Chen, Y.-c., Aso, Y., Cardona, A., Eschbach, C., Kobler, O., Voigt, A., Durairaja, A., Mancini, N., Zlatic, M., Truman, J. W., Thum, A. S., & Gerber, B. (2018, 2018/12//). Functional architecture of reward learning in mushroom body extrinsic neurons of larval Drosophila. *Nature Communications, 9*(1), 1104-1104. https://doi.org/10.1038/s41467-018-03130-1

Scheffer, L. K., Xu, C. S., Januszewski, M., Lu, Z., Takemura, S. Y., Hayworth, K. J., Huang, G. B., Shinomiya, K., Maitlin-Shepard, J., Berg, S., Clements, J., Hubbard, P. M., Katz, W. T., Umayam, L., Zhao, T., Ackerman, D., Blakely, T., Bogovic, J., Dolafi, T., Kainmueller, D., Kawase, T., Khairy, K. A., Leavitt, L., Li, P. H., Lindsey, L., Neubarth, N., Olbris, D. J., Otsuna, H., Trautman, E. T., Ito, M., Bates, A. S., Goldammer, J., Wolff, T., Svirskas, R., Schlegel, P., Neace, E., Knecht, C. J., Alvarado, C. X., Bailey, D. A., Ballinger, S., Borycz, J. A., Canino, B. S., Cheatham, N., Cook, M., Dreher, M., Duclos, O., Eubanks, B., Fairbanks, K., Finley, S., Forknall, N., Francis, A., Hopkins, G. P., Joyce, E. M., Kim, S., Kirk, N. A., Kovalyak, J., Lauchie, S. A., Lohff, A., Maldonado, C., Manley, E. A., McLin, S., Mooney, C., Ndama, M., Ogundeyi, O., Okeoma, N., Ordish, C., Padilla, N., Patrick, C. M., Paterson, T., Phillips, E. E., Phillips, E. M., Rampally, N., Ribeiro, C., Robertson, M. K., Rymer, J. T., Ryan, S. M., Sammons, M., Scott, A. K., Scott, A. L., Shinomiya, A., Smith, C., Smith, K., Smith, N. L., Sobeski, M. A., Suleiman, A., Swift, J., Takemura, S., Talebi, I., Tarnogorska, D., Tenshaw, E., Tokhi, T., Walsh, J. J., Yang, T., Horne, J. A., Li, F., Parekh, R., Rivlin, P. K., Jayaraman, V., Costa, M., Jefferis, G. S., Ito, K., Saalfeld, S., George, R., Meinertzhagen, I. A., Rubin, G. M., Hess, H. F., Jain, V., & Plaza, S. M. (2020, Sep 7). A connectome and analysis of the adult Drosophila central brain. *eLife, 9*. https://doi.org/10.7554/eLife.57443

Schlegel, P., Texada, M. J., Miroschnikow, A., Schoofs, A., Hückesfeld, S., Peters, M., Schneider-Mizell, C. M., Lacin, H., Li, F., Fetter, R. D., Truman, J. W., Cardona, A., & Pankratz, M. J. (2016, 2016/11//). Synaptic transmission parallels neuromodulation in a central food-intake circuit. *eLife, 5*. https://doi.org/10.7554/eLife.16799

Schneider-Mizell, C. M., Gerhard, S., Longair, M., Kazimiers, T., Li, F., Zwart, M. F., Champion, A., Midgley, F. M., Fetter, R. D., Saalfeld, S., & Cardona, A. (2016,

2016/3//). Quantitative neuroanatomy for connectomics in Drosophila. *eLife, 5*. https://doi.org/10.7554/eLife.12059

Scholz, N., Gehring, J., Guan, C., Ljaschenko, D., Fischer, R., Lakshmanan, V., Kittel, R. J., & Langenhan, T. (2015, 2015/05/12/). The Adhesion GPCR Latrophilin/CIRL Shapes Mechanosensation. *Cell Reports, 11*(6), 866-874. https://doi.org/https://doi.org/10.1016/j.celrep.2015.04.008

Shannon, P., Markiel, A., Ozier, O., Baliga, N. S., Wang, J. T., Ramage, D., Amin, N., Schwikowski, B., & Ideker, T. (2003, Nov). Cytoscape: a software environment for integrated models of biomolecular interaction networks. *Genome Res, 13*(11), 2498-2504. https://doi.org/10.1101/gr.1239303

Sweeney, S. T., Broadie, K., Keane, J., Niemann, H., & O'Kane, C. J. (1995, Feb). Targeted expression of tetanus toxin light chain in Drosophila specifically eliminates synaptic transmission and causes behavioral defects. *Neuron, 14*(2), 341-351. https://doi.org/10.1016/0896-6273(95)90290-2

Takagi, S., Cocanougher, B. T., Niki, S., Miyamoto, D., Kohsaka, H., Kazama, H., Fetter, R. D., Truman, J. W., Zlatic, M., Cardona, A., & Nose, A. (2017, 2017/12//). Divergent Connectivity of Homologous Command-like Neurons Mediates Segment-Specific Touch Responses in Drosophila. *Neuron, 96*(6), 1373-1387.e1376. https://doi.org/10.1016/j.neuron.2017.10.030

Talpalar, A. E., Bouvier, J., Borgius, L., Fortin, G., Pierani, A., & Kiehn, O. (2013, Aug 1). Dual-mode operation of neuronal networks involved in left-right alternation. *Nature, 500*(7460), 85-88. https://doi.org/10.1038/nature12286

Tastekin, I., Khandelwal, A., Tadres, D., Fessner, N. D., Truman, J. W., Zlatic, M., Cardona, A., & Louis, M. (2018, Nov 22). Sensorimotor pathway controlling stopping behavior during chemotaxis in the Drosophila melanogaster larva. *eLife, 7*. https://doi.org/10.7554/eLife.38740

Tenedini, F. M., Sáez González, M., Hu, C., Pedersen, L. H., Petruzzi, M. M., Spitzweck, B., Wang, D., Richter, M., Petersen, M., Szpotowicz, E., Schweizer, M., Sigrist, S. J., Calderon de Anda, F., & Soba, P. (2019, 2019/08/05). Maintenance of cell type-specific connectivity and circuit function requires Tao kinase. *Nature Communications, 10*(1), 3506. https://doi.org/10.1038/s41467-019-11408-1

Tracey, W. D., Wilson, R. I., Laurent, G., & Benzer, S. (2003, 2003/4//). painless, a Drosophila gene essential for nociception. *Cell, 113*(2), 261-273. http://www.ncbi.nlm.nih.gov/pubmed/12705873

Tsubouchi, A., Caldwell, J. C., & Tracey, W. D. (2012, 2012/11//). Dendritic filopodia, Ripped Pocket, NOMPC, and NMDARs contribute to the sense of touch in Drosophila larvae. *Current biology : CB, 22*(22), 2124-2134. https://doi.org/10.1016/j.cub.2012.09.019

Turner, H. N., Armengol, K., Patel, A. A., Himmel, N. J., Sullivan, L., Iyer, S. C., Bhattacharya, S., Iyer, E. P. R., Landry, C., Galko, M. J., & Cox, D. N. (2016, Dec 5). The TRP Channels Pkd2, NompC, and Trpm Act in Cold-Sensing Neurons to Mediate Unique Aversive Behaviors to Noxious Cold in Drosophila. *Curr Biol, 26*(23), 3116-3128. https://doi.org/10.1016/j.cub.2016.09.038

Turner, H. N., Patel, A. A., Cox, D. N., & Galko, M. J. (2018). Injury-induced cold sensitization in Drosophila larvae involves behavioral shifts that require the TRP channel Brv1. *PLoS One, 13*(12), e0209577. https://doi.org/10.1371/journal.pone.0209577

Vaadia, R., Li, W., Voleti, V., Singhania, A., Hillman, E. M. C., & Grueber, W. B. (2018, 2018/11//). Characterization of proprioceptive system dynamics in behaving Drosophila larvae using high-speed volumetric microscopy. *bioRxiv*, 467274-467274. https://doi.org/10.1101/467274

Valdes-Aleman, J., Fetter, R. D., Sales, E. C., Heckman, E. L., Venkatasubramanian, L., Doe, C. Q., Landgraf, M., Cardona, A., & Zlatic, M. (2021). Comparative Connectomics Reveals How Partner Identity, Location, and Activity Specify Synaptic Connectivity in Drosophila. *Neuron, 109*(1), 105-122.e107. https://doi.org/10.1016/j.neuron.2020.10.004

Vogelstein, J. T., Park, Y., Ohyama, T., Kerr, R. A., Truman, J. W., Priebe, C. E., & Zlatic, M. (2014, 2014/4//). Discovery of Brainwide Neural-Behavioral Maps via Multiscale Unsupervised Structure Learning. *Science, 344*(6182), 386-392. https://doi.org/10.1126/science.1250298

Ward, L., Wright, E., & McMahon, S. B. (1996, Jan). A comparison of the effects of noxious and innocuous counterstimuli on experimentally induced itch and pain. *Pain, 64*(1), 129-138. https://doi.org/10.1016/0304-3959(95)00080-1

Winding, M., Pedigo, B. D., Barnes, C. L., Patsolic, H. G., Park, Y., Kazimiers, T., Fushiki, A., Andrade, I. V., Khandelwal, A., Valdes-Aleman, J., Li, F., Randel, N., Barsotti, E., Correia, A., Fetter, R. D., Hartenstein, V., Priebe, C. E., Vogelstein, J. T., Cardona, A., & Zlatic, M. (2023, Mar 10). The connectome of an insect brain. *Science, 379*(6636), eadd9330. https://doi.org/10.1126/science.add9330

Wu, P., Arris, D., Grayson, M., Hung, C. N., & Ruparel, S. (2018). Characterization of sensory neuronal subtypes innervating mouse tongue. *PLoS One, 13*(11), e0207069. https://doi.org/10.1371/journal.pone.0207069

Xiao, R., & Xu, X. Z. S. (2021, Feb 10). Temperature Sensation: From Molecular Thermosensors to Neural Circuits and Coding Principles. *Annu Rev Physiol, 83*, 205-230. https://doi.org/10.1146/annurev-physiol-031220-095215

Yan, Z., Zhang, W., He, Y., Gorczyca, D., Xiang, Y., Cheng, L. E., Meltzer, S., Jan, L. Y., & Jan, Y. N. (2012, 2012/12//). Drosophila NOMPC is a mechanotransduction channel subunit for gentle-touch sensation. *Nature, 493*(7431), 221-225. https://doi.org/10.1038/nature11685

Yoshino, J., Morikawa, R. K., Hasegawa, E., & Emoto, K. (2017, 2017/8//). Neural Circuitry that Evokes Escape Behavior upon Activation of Nociceptive Sensory Neurons in Drosophila Larvae. *Current Biology, 27*(16), 2499-2504.e2493. https://doi.org/10.1016/j.cub.2017.06.068

Zarin, A. A., Mark, B., Cardona, A., Litwin-Kumar, A., & Doe, C. Q. (2019, Dec 23). A multilayer circuit architecture for the generation of distinct locomotor behaviors in Drosophila. *eLife, 8*. https://doi.org/10.7554/eLife.51781

Zheng, Z., Lauritzen, J. S., Perlman, E., Robinson, C. G., Nichols, M., Milkie, D., Torrens, O., Price, J., Fisher, C. B., Sharifi, N., Calle-Schuler, S. A., Kmecova, L., Ali, I. J., Karsh, B., Trautman, E. T., Bogovic, J. A., Hanslovsky, P., Jefferis, G., Kazhdan, M., Khairy, K., Saalfeld, S., Fetter, R. D., & Bock, D. D. (2018, Jul 26). A Complete Electron Microscopy Volume of the Brain of Adult Drosophila melanogaster. *Cell, 174*(3), 730-743 e722. https://doi.org/10.1016/j.cell.2018.06.019

Zhu, J., Boivin, J. C., Garner, A., Ning, J., Zhao, Y. Q., & Ohyama, T. (2024, Aug 28). Feedback inhibition by a descending GABAergic neuron regulates timing of escape behavior in Drosophila larvae. *eLife, 13*. https://doi.org/10.7554/eLife.93978

Zwart, M. F., Pulver, S. R., Truman, J. W., Fushiki, A., Fetter, R. D., Cardona, A., & Landgraf, M. (2016, 2016/8//). Selective Inhibition Mediates the Sequential Recruitment of Motor Pools. *Neuron, 91*(4), 944-944. https://doi.org/10.1016/j.neuron.2016.07.041